

SCANNING PROBE STUDIES ON THE SURFACE OF Bi_2Se_3

By

Megan E. Romanowich

A DISSERTATION

Submitted to
Michigan State University
in partial fulfillment of the requirements
for the degree of

DOCTOR OF PHILOSOPHY

Physics

2012

ABSTRACT

SCANNING PROBE STUDIES ON THE SURFACE OF Bi_2Se_3

By

Megan E. Romanowich

Topological insulators are an exciting material that are insulating in the bulk, but have a metallic surface state where spin and momentum are locked perpendicular to each other by strong spin orbit coupling. The simplest topological insulator, Bi_2Se_3 , has a band gap of 0.3 eV and a single Dirac cone, a state where energy and momentum are linearly related, in the gap. This special state is protected against scattering and small perturbations by time reversal symmetry. Before any of the exotic effects predicted to be present in this material can be fully realized, it is important to know what other electronic effects coexist with the topological state on the surface of the material. To that end, I employed scanning tunneling microscopy on the surface of Bi_2Se_3 far from defect states. I probed the interplay of bulk electrons with the Dirac cone that adds additional states. I also show that the Dirac cone can coexist with a two-dimensional electron gas, although the amplitude is potentially reduced.

In memory of my father, Dr. Robert H. Knapp MD, who was responsible for fostering my love of science and for my mother who helped me achieve my educational goals along the way.

ACKNOWLEDGMENTS

I could not go any further in writing my dissertation without first acknowledging the people who helped me along the way. I first want to recognize my advisor, Stuart Tessmer, who has been an invaluable resource in the lab. He helped me by answering questions sincerely, no matter how simplistic they turned out to be, helped me thing through experimental processes, and offered suggestions to troubleshoot the equipment. I always appreciated his encouragement and his overly generous compliments about my scientific abilities. From Stuart I not only learned how to be a thoughtful scientist, but also how to relax and be a good mentor to others in the lab.

Stuart is not the only person to help support my research. Mal-soon Lee spent many hours perfecting the calculations related in this work. She took the time to explain some of the challenges with the program and the subtleties of the theoretical approach. S.D. Mahanti likewise spent many hours in meetings helping with the analysis and offering his words of wisdom.

There are many individuals who help the day-to-day activities of the department run smoothly. The PA Machine Shop spent many hours talking through designs and making the processing chamber that gave me the pristine samples for my experiments. I would particularly like to thank Tom Palazzolo for his incredible machining knowledge. Baokang Bi spent hours helping me learn and then troubleshoot the scanning electron microscope in the clean room. Reza Lolee was an invaluable resource on cryogenic systems and always helped find the tool I needed from somewhere in the basement. It never ceases to amaze me just how much Reza knows about everything that goes on in the basement labs. My time teaching labs would not have run nearly so smoothly without the knowledge and help

of Mark Olsen and Richard Hallstein. Happily, Debbie Barratt and Kim Crosslan have been invaluable resources and I am sure they have done more paperwork for me than I will know. I would also recognize my committee: Professors Pengpeng Zhang, Remco Zegers, Kirsten Tollefson and Carlo Piermarocchi. It was nice to have their support through this process.

I have very much appreciated those I shared a lab with throughout my time here. Josh Veazey spent hours explaining what he was doing when he scanned and gave me helpful hints on how to use the microscope. Kathy Walsh has been an amazing friend to me. I enjoyed our conversations about science and *Doctor Who* over lunches and in the lab. Her undying optimism, puns and dramatic flair helped me through many days where I thought nothing was going to work. I also appreciate the hard work and creativity of three great undergraduates: Mark Regalla, Andrew Belcher, and Eric Goodwin who perfected the process for and made tips for my experiments. They all helped take a half-baked idea to make ultra-sharp tips and make it a reality. Day to day lab work would not be nearly so interesting without the day-to-day conversations with other lab-mates and others who also inhabit the basement over the years: Matt DeNinno, Sean Wagner, Eric Gingrich and John Raguse. I have many happy memories of time in the lab spent chatting about different scientifically irrelevant (and sometimes relevant) topics with these individuals.

In addition to my work in the lab, I have greatly enjoyed participating in committees and organizations over my time at Michigan State University. Women and Minorities in the Physical Sciences gave me the opportunity to grow as a leader, learn about challenges facing women in science, and take steps to address common problems locally. In particular, I have loved my time in the Mentoring program, both as the Mentoring Program Coordinator and as a mentor. I was thrilled with the department's financial and graduate student mentors'

time commitments that enabled this program to be successful. Through mentoring, I was able to meet some promising young undergraduates. Because I got to mentor them through their entire undergraduate experience, the two that I particularly enjoyed were Monica Derris and Caitlin Brecklin. These two mentees and some of the others impressed me with how intentional they were with their future careers in physics and science. The other committee that enabled me to not only become a better leader but also to change things within the college was the Council of Diversity and Community in the College of Natural Science. Here, I met some extremely motivated graduate students in the College outside my discipline and dedicated staff members who truly want to address some key issues within the College to make it a better place for everyone.

Were it not for my study group, I would not remember the very first years of graduate school so fondly. Dan Olds has been a constant support from classes through research from the very first day of orientation. He has provided some perspective on problems through both verbal and alcoholic perspective. Carol Guess and Ania Kwiatkowski were both friends and mentors. Their individual senses of poise and self-confidence are qualities I have tried to emulate. These three made studying for subject exam classes enjoyable. Some of my favorite study breaks were during girls nights with Amanda Prinke and Johanna Swanson. Game nights with Dan Olds, Marilyn McDowall, Jenni Portman and her husband Guiseppe, Connor Glosser and Shannon and Jim Demlow have been excellent at lightening the mood after a lot of time in the lab or writing my thesis.

My life would not be complete without all the joy I get from my family. My parents gave me so many advantages and emotional support throughout all my studies that helped me to get where I am now. I count myself fortunate that my family has grown over my

time in graduate school and that all of my family including my sister, Sarah, is nothing but supportive of my sometimes demanding educational endeavors. I especially appreciate the support of my husband, Tim, even when my path through school and ultimate employment goals were unclear. He has been a particular support these last few months by taking on much of the responsibility for our darling daughter, Amelia, so that I could focus on finishing up. I love them all and I could not enjoy my work so much without the joy they bring me at home.

PREFACE

Having just left Dr. Mackey's material science research lab in summer of 2008, I was very excited to learn a new technique in the Tessmer group: scanning tunneling microscopy. Over the next year, I rebuilt a scanning tunneling microscope, learning what makes scanning tunneling microscopy work. At the same time, a hot new area of research was just coming to prominence on the condensed matter scene. The earliest experiments on three-dimensional topological insulators were published in 2008 and 2009, just after I began my research in the Tessmer group. Due to a fascinating surface state, topological insulators are a natural pairing with scanning tunneling microscopy and other surface probe techniques. Shortly after joining the group, I proposed the experiments on the topological insulator Bi_2Se_3 which made up the experiments described in this work.

Over the next few chapters I will explain some scanning probe techniques and unusual features in the local density of states in Bi_2Se_3 . To ground the reader in the literature, I have taken a historical approach in the introduction. As topological insulators are a rather specific topic, I am motivating key aspects of their physics by first explaining the earliest experiments in two dimensions. This early work shaped some of the terminology in topological insulating literature today. Conversely, scanning probe microscopy has so many applications that to do it justice, I very briefly elaborate on its scope before focusing on my Bi_2Se_3 studies.

TABLE OF CONTENTS

List of Figures	xi
Chapter 1 Introduction	1
1.1 Topological Insulators	1
1.2 Scanning Probe Methods	6
Chapter 2 Apparatus and Technique	8
2.1 Sample Processing Chamber	8
2.2 Scanning Tunneling Microscopy and Spectroscopy	11
2.2.1 Physics	14
2.2.2 Calibration	17
2.2.2.1 Graphite	18
2.2.2.2 Pt Pits	18
2.3 Experimental Constraints and Setup	20
2.3.1 Besocke Type STM	20
2.3.2 Noise Isolation	22
2.3.3 Cryogenic System	22
2.3.4 Tips	23
2.3.4.1 <i>In situ</i> Tip Cleaning Techniques	25
Chapter 3 An Introduction to Topological Insulators	27
3.1 Background	27
3.1.1 Graphene Model	30
3.1.2 HgTe/CdTe Wells	35
3.1.3 Three Dimensional Topological Insulators	37
3.1.4 Early Studies on $\text{Bi}_{1-x}\text{Sb}_x$	38
3.1.4.1 ARPES	39
3.1.4.2 Quasiparticle Interference Patterns	39
3.2 Bi_2Se_3 Background	41
3.2.1 Structure	41
3.2.2 Dopants and Defects	44
3.2.3 Surface Potential Fluctuations	47
3.2.4 Band Bending	49

Chapter 4	Measurements of States on the Surface of Bi_2Se_3	54
4.1	Sample Overview and Procedure	54
4.2	Spectroscopy Measurements on Bi_2Se_3	56
4.3	Analysis of the Bi_2Se_3 Spectrum	61
4.4	Analysis of Two Dimensional Electron Gas on the Surface	65
4.5	Bi_2Se_3	69
Chapter 5	Other Measurements of Bi_2Se_3	72
5.1	$\text{Bi}_{2.02}\text{Se}_{2.98}$	72
5.2	$\text{Bi}_{2.04}\text{Se}_{2.96}$	74
5.3	$\text{Bi}_{2.08}\text{Se}_{2.92}$	78
Chapter 6	Other Scanning Probe Methods	81
6.1	Capacitance and Kelvin Probe Circuit	81
6.1.1	High Electron Mobility Transistor	83
6.2	Capacitance Measurement	85
6.2.1	Physics	85
6.2.2	Demonstration	87
6.3	Kelvin Probe Measurement	87
6.3.1	Physics	88
6.3.2	Demonstration	90
6.4	Tips	91
6.4.0.1	Etched	92
6.4.0.2	Cut	93
6.4.0.3	Ultrasharp	94
Chapter 7	Conclusions	97
7.1	Summary	97
7.2	Future Directions	99
Bibliography		100

LIST OF FIGURES

- Figure 1.1 For interpretation of the references to color in this and all other figures, the reader is referred to the electronic version of this dissertation. Arrows in these diagrams represent spin. (a) Band diagram of an insulator showing the filled valence states are separated from empty conduction band states by a band gap. The bands are spin degenerate. (b) In a topological insulator, a surface state connecting the conduction and valence band consists of a band where holes traveling left (negative in k -space) are connected to electrons traveling right, and vice versa exists within the gap. In (b) the horizontal scale represents momentum, but there is no physical meaning to the horizontal scale in (a). 4
- Figure 1.2 (a) Three quintuple layers of Bi_2Se_3 . Inside each layer the atoms form covalent bonds and each layer is held to its neighbor by Van der Waals forces. This image is from of Dr. Mal-soon Lee. (b) My Bi_2Se_3 local density of states measurement. The dotted lines show the Dirac cone. Specific features of the Dirac cone will be discussed in Chapter 4. 5
- Figure 2.1 My processing chamber. (a) The back of the chamber showing the exit to the microscope and two ports. The top port goes to a pressure relief valve that prevents the chamber from exploding the top off and exposing the contents to air. The lower port connects to a loading chamber so that the main chamber is always under nitrogen. (b) The top shows two access ports: one is for loading materials too big to come in through the loading chamber. The other supports the tubes that allow nitrogen to come in and out in a continuous flow through the chamber. The two protrusions are the glove ports. All of these tubes and lids are made of plexiglass to allow maximum light within the chamber. The support structure on the right is made of aluminum and provides the strength to support the loading fork. 10

Figure 2.2	My experimental setup. The blue dewar in the lower left of the image is my cryogenic system discussed in Section 2.3.3. The sample processing chamber is in the center of the image with yellow gloves. The fork for transferring the sample is inside the steel tube to the right on the image (and has the pink marker on its end). The sample loading chamber is not visible as it is behind the nitrogen chamber itself. . .	12
Figure 2.3	(a) Schematic of the tip and the sample. The sample is in the x-y plane and the tip is hovering above the sample in the z-direction. (b) A model of tunneling barrier showing the wavefunction decays exponentially in the gap [38].	13
Figure 2.4	(a) Graphite atoms at a 1.0 nA tunneling current and 0.1 V bias. The scale bar is 500 pm. (b) This is an image of step edge of graphite. The spectra shown in (c) and (d) were taken on the smooth part of the image. Because the scale of this image is so much larger than (a), individual atoms are not resolved. The scale bar is 200 nm. (c) Shows linear I-V curve on graphite. (d) Density of states measurement on graphite.	19
Figure 2.5	Pt pits sample where the scale bar is 1 μm . The pit is 5 $\mu\text{m} \times 5 \mu\text{m}$ and 180 nm deep. There is at least a double tip, possibly a triple tip in this case giving rise to multiple apparent edges as indicated by the arrows.	20
Figure 2.6	(a) Besoke design microscope where three piezoelectric tubes support a sample and a central tube scans the tip. (b) My microscope outside of its protective case.	21
Figure 2.7	Diagram of the cryostat. The microscope mounts on the probe entry port and is isolated from the sample tube by a gate valve until it is under vacuum. The microscope can then be lowered slowly into the bottom of the dewar. The system is cooled by a main bath of nitrogen or helium. The transfer tube entry port is the site where liquid is transferred into the system. Gas from liquid boil off is released through the helium exhaust port [43].	24

Figure 3.1	Figure from Zhang <i>et al.</i> [44] shows the unit cell in a crystal lattice of Bi_2Se_3 . Primitive vectors \vec{t}_1 , \vec{t}_2 , and \vec{t}_3 show equivalent translation vectors of the lattice. There are 3 inequivalent sites in the lattice, Bi, Se1 and Se2 that stack in inequivalent layers C(Se1)-A(Se1)-B(Bi)-C(Se2)-A(Bi)-B(Se1)-C(Se1). Viewed from above, this looks like a hex lattice with inequivalent layers marking out triangular lattices. In the bottom right, the three-dimensional unit cell is mapped out with its two-dimensional projection showing high symmetry points in k -space, Γ , M and K that are time reversal invariant momentum points for this crystal structure. Used under Creative Commons Attribution 3.0 Unported (CC-BY) license and all credit for creation of this figure goes to [44].	28
Figure 3.2	A calculation from Kane and Mele [48]. A single pair of edge states traverse the bulk insulating gap due to spin orbit coupling in a band structure calculation from a tight-binding model on a strip (in the inset) of graphene. Reprinted figure with permission from Kane, C.L. and Mele, E.J., <i>Physical Review Letters</i> , 95, 226801(2005). Copyright (2005) by the American Physical Society. Abstract can be viewed at: http://prl.aps.org/abstract/PRL/v95/i22/e226801	33
Figure 3.3	A schematic band structure showing Kramers pairs traversing the gap from Fu <i>et al.</i> [52]. (a) A schematic of a topological insulator that has an odd number of Fermi level crossings. (b) A schematic of a simple insulator that has an even number of crossings. There are still degenerate points at Λ_a and Λ_b but they are not topologically protected against deformation. Reprinted figure with permission from Fu, Liang and Kane, C.L., <i>Physical Review B</i> , 76, 045302 (2007). Copyright (2007) by the American Physical Society. Abstract can be viewed at: http://prb.aps.org/abstract/PRB/v76/i4/e045302	34
Figure 3.4	Figure adapted from Konig <i>et al.</i> [56]. Resistance measurement of CdTe/HgTe quantum wells that support the quantum spin Hall state. Sample I shows that the wells are insulating below the critical width. Sample II shows disorder due to temperature effects. Samples III and IV show that the conductance is precisely equal to $2e^2/h$ for two different well widths above the critical dimension. From M. Koenig, S. Wiedmann, C. Bruene, A. Roth, H. Buhmann, L. W. Molenkamp, X.-L. Qi, S.-C. Zhang, <i>Science</i> , 318, 766-770 (2007). Reprinted with permission from AAAS.	36

Figure 3.5	(a) Adapted from [58]. $\text{Bi}_{0.92}\text{Sb}_{0.08}$ dI/dV map with the Fourier transform of the image inset. The snowflake pattern shows the six-fold symmetric scattering in k -space. Some scattering directions are forbidden. (b) Adapted from Figure 4 in reference [58]. The scattering patterns are only duplicated when spin-dependent scattering is accounted for in calculations. Reprinted by permission from Macmillan Publishers Ltd: NATURE (P.Roushan, J.Seo, C.V. Parker, Y.S. Hor, D.Hsieh, D.Qian, A.Richardella, M.Z. Hasan, R.J. Cava, and A.Yazdani. "Topological surface states protected from backscattering by chiral spin texture," <i>Nature</i> , 460, 11061109, (2009)), copyright (2009)	40
Figure 3.6	Density functional theory calculation of the Bi_2Se_3 bulk [gray] and 6 quintuple layer calculation of the Dirac cone in blue. The single Dirac cone on the surface is circled in red. Figure courtesy of Dr. Mal-soon Lee.	42
Figure 3.7	Triangular defects on Bi_2Se_3 where the bright triangles are attributed to bismuth on a selenium site substitutions. The scan range is $65 \text{ nm} \times 65 \text{ nm}$. Topograph from Urazhdin <i>et al.</i> [10]. Reprinted figure with permission from S.Urazhdin, D.Bilc, S.Mahanti, S.Tessmer, T.Kyratsi, and M.Kanatzidis. <i>Physical Review B</i> , 69(8):085313, 2004. Copyright (2004) by the American Physical Society. Abstract can be viewed at: http://prb.aps.org/abstract/PRB/v69/i8/e085313	44
Figure 3.8	Quasiparticle scattering data from Kim <i>et al.</i> [95]. The six-fold symmetry gets smeared by the bulk valence band when the voltage is less than -500 meV and by the bulk conduction band when it is greater than -250 meV. Scattering is enhanced in the Γ -M direction and suppressed in the Γ -K. At some voltages, they 6-fold symmetry is less clear. (a) and (b) show the smearing of the topological state due to the valence band and (g)-(i) show the smearing due to the conduction band. Reprinted figure with permission from S.Kim, M.Ye, K.Kuroda, Y.Yamada, E.Krasovskii, E.Chulkov, K.Miyamoto, M.Nakatake, T.Okuda, Y.Ueda, K.Shimada, H.Namatame, M.Taniguchi, and A.Kimura. <i>Physical Review Letters</i> , 107:056803, (2011). Copyright (2011) by the American Physical Society. Abstract can be viewed at: http://prl.aps.org/abstract/PRL/v107/i5/e056803	48

Figure 3.9	ARPES measurements on Bi_2Se_3 showing effects of the top quintuple layer separating from the crystal [102] E vs. k of the Dirac cone is shown with the 2DEG evident as the bright rim surrounding the diffuse conduction band edge. The Dirac cone is the outer x shaped feature with the Dirac point at the center of the x. Reprinted by permission from Macmillan Publishers Ltd: NATURE COMMUNICATIONS (M.Bianchi, D.Guan, S.Bao, J.Mi, B.B. Iversen, P.D.C. King, and P.Hofmann. “Coexistence of the Topological State and a Two-Dimensional Electron Gas on the Surface of Bi_2Se_3 ”. Nature Communications, 1:128, 2010.), copyright (2010)	53
Figure 4.1	Characteristic triangles from bismuth substitutions on selenium sites in Bi_2Se_3 doped with 4% excess Bi. Image is at 4.2K with -0.8 V bias and 0.50 nA set current. The scale bar is 3 nm.	56
Figure 4.2	(a) The calculated I-V curve on Bi_2Se_3 doped with 4% excess Bi at 4.2K. (b) The same I-V curve expanded in the region of the Dirac cone. The slope does not go to zero at zero voltage, indicating there are states in the gap. Due to an analog to digital issue in the electronics, the current was calculated from the dI/dV curve in Figure 4.3 (a). The dI/dV curve was measured directly from using the lock-in amplifier as described in Section 2.2.1 and therefore did not experience the same analog to digital issue.	57
Figure 4.3	(a) Density of states on Bi_2Se_3 doped with 4% excess Bi at 4.2K where the linear region of the Dirac cone is between ± 0.15 V. The Fermi level is in the center of the gap. There are additional states that lift up the bottom of the Dirac cone. The curve is an average of 150 curves taken successively to reduce the signal to noise ratio. (b) The density of states only in the region of the Dirac cone showing parameters α and β , described in the text.	58
Figure 4.4	Density of States where each of the curves is an average of 50 measurements. Data set A was taken before Data set B without manually moving the tip. Data set A has been offset by one tick mark to ease visual comparison. A blue bracket has been drawn to highlight the enhancement. We speculate the tip drifted during the measurement, causing the feature at +0.2 V to change.	60

Figure 4.5	(a) Valence band calculation with increasing numbers of QL. The shoulder state in the Γ -M direction increases in energy and eventually crosses the Dirac point. (b) Graph of the change in energy with QL. Eventually the height of the shoulder will reach a bulk value as the number of QL increases. Figure courtesy of Dr. Mal-soon Lee	62
Figure 4.6	Partial density of states (PDOS) calculations performed by Dr. Mal-soon Lee on a 6 QL slab. The inset shows the parts of k-space that contribute to Region I and Region II. The contribution to PDOS from the Dirac cone is depicted in red. It resides primarily in the top layers within the bulk band gap. The contribution from the shoulder states (blue) have the largest contribution in the middle QL, however it has a finite contribution in the top QL Se and Bi atoms. In this case, the peak is just to the left of zero energy (the Fermi level) for this rather thin slab.	66
Figure 4.7	Comparison of bulk and slab calculations. This contrasts the partial charge density from bulk band structure calculations (gray in the band structure) on the left side of the image with those from the slab calculations (blue in the band structure calculations). The Se are yellow, the Bi atoms are blue-gray and the the intensity of the red halos depicts how strong the charge density is at that region. No halo means there is no significant charge density. The bulk calculations show the partial charge density is mostly distributed on the Se atoms in all layers equally. The partial charge density on the slab calculation on the right is primarily located on Se atoms as well, but has the highest density in the middle layers (the bulk-like area of the slab). However, there is some charge density on Se atoms in the outermost quintuple layers shown by the green arrows. Figure courtesy of Dr. Mal-soon Lee	67
Figure 4.8	Band structure calculations of a 6 QL slab of Bi_2Se_3 for which the top QL is separated from the others. The percentages refer to how much additional separation is given to the top QL. We see as the top layer detaches, the bottom of the conduction band drops into the gap and forms a two-dimensional electron gas on the surface. Figure courtesy of Dr. Mal-soon Lee.	70
Figure 4.9	STM data at 77K. Both the (a) I-V curve and the (b) density of states are an average of 5 curves. (c) Atoms on the surface of Bi_2Se_3 at -0.20 V and 0.1 nA. Scale bar is 1.6 nm.	71

Figure 5.1	Data taken at 77K without the chamber. (a) Atoms on the surface of $\text{Bi}_{2.02}\text{Se}_{2.98}$ at a set current of 0.11 nA and -0.5 V. Scale bar is 3 Å. (b) Dark pits seen all over the $\text{Bi}_{2.02}\text{Se}_{2.98}$ potentially caused by surface contamination. Scale bar is 17 Å.	74
Figure 5.2	Defects on the surface of $\text{Bi}_{2.02}\text{Se}_{2.98}$ at 0.5 nA set tunneling current and 77K. Scale bars are 7 Å. Each image is taken in sequence at a bias voltage of (a) -0.5 V (b) -0.55 V (c) -0.50 V and (d) -0.4 V. The bright spot in the upper right corner of every image is surface contamination. Impurities in the crystal are visible in the upper left in (a) and (c).	75
Figure 5.3	Defects on the surface of $\text{Bi}_{2.04}\text{Se}_{2.96}$ at 0.5 nA set tunneling current and liquid helium temperature. Each image is taken in sequence at a bias voltage of (a) -0.80 V, 36 pA (b) -0.49 V, 73 pA and (c) -0.29 V, 52 pA. Dark impurity spots become more diffuse with changing voltage. Bright specs of surface contamination also visible in every image. Scale bars are 3.3nm.	76
Figure 5.4	Data taken at 4.2K. Scale bars are 3.3 nm.(a) Bright triangular defects on the surface of $\text{Bi}_{2.04}\text{Se}_{2.96}$ at a set current of 60 pA and bias voltage of -0.80 V. (b) Clusters of triangular defects arranging in strings at 60 pA and -0.79 V.	77
Figure 5.5	Data taken at 77K. (a) Bright triangular defects on the surface of $\text{Bi}_{2.04}\text{Se}_{2.96}$ at a set current of 24 pA and bias voltage of -0.48 V. Scale bar is 17 nm. (b) Pits on the surface at 118 pA and -0.38 V. The scale bar is 67 nm.	78
Figure 5.6	Data at 77K, scale bar is 3.3 Å and set current 1.02 nA. (a) -0.6 V (b) -0.3 V and (c) -0.6 V. There is both surface contamination, atomic resolution and a voltage-dependent defect in the upper right corner.	79
Figure 6.1	HEMT circuit diagram: The standard capacitor (line drawn in blue) is only included for capacitance measurements. Oscillations are applied either to the bias voltage for capacitance measurements or by oscillating the tip above the sample in Kelvin probe. The lock-in amplifier detects the change in capacitance on the tip due to these oscillations.	82

Figure 6.2	The plot shows the drain current vs. the drain-source voltage of a HEMT at different gate voltages. Varying the gate voltage changes the effective resistance of the source-drain channel. The HEMT is operated in the linear region circled in red to minimize power output [43].	84
Figure 6.3	A photograph of the Fujutsi model FHX35X HEMT. The size of the device is $\sim 500 \mu\text{m}$ across [43].	84
Figure 6.4	(a) Topography image of the corner of a pit. (b) Capacitance image in the same region as (a). Both are imaged at 77K, the scale bars are 330nm long and were taken with an etched tip.	87
Figure 6.5	Nulling voltage measurement on Bi_2Se_3 . The arrow shows the voltage where all the curves intersect (0.9 V). Because there is a -0.43 V applied to the tip relative to the sample, the nulling voltage here is $0.9 - (-0.43) = 1.23 \text{ V}$	89
Figure 6.6	Bi_2Se_3 topography (a) and Kelvin probe (b). In this case, the Kelvin probe image is nearly featureless because the signal is dominated by the high plateau in the lower left. The topography image shows two step edges, where each step is 1 nm high. The Kelvin probe scan must be within half a nanometer of the sample – even one nanometer beyond does not contribute. The scale bar is 170 nm on both images. The amplitude of oscillation is 1 nm.	90
Figure 6.7	Bi_2Se_3 topography (a) and Kelvin probe (b), Here we see a scan showing a trench indicated by an arrow. The trench is three times as wide in Kelvin probe as topography. Th Kelvin probe scan had a 1 nm amplitude of oscillation on the tip at the nulling voltage and was 1 nm above the sample. The scale bars are both 33 nm. The tip may have drifted over the four hours between the topography scan and the Kelvin probe scan	92
Figure 6.8	SEM image of an etched tip made by Agilent with a tip radius of curvature of 100 nm. Both (a) and (b) are the same tip with different scales.	93
Figure 6.9	Cut tips with a radius of curvature of 10 nm and 25 nm.	94

Figure 6.10	(a) The micropositioner used to assemble the ultrasharp tips. It finely positions a Pt(.8)Ir(.2) wire with respect to a AFM cantilever. (b) A view through the microscope used to see tip placement on the epoxy. The triangular cantilever is touching the conducting epoxy.	95
Figure 6.11	Ultrasharp tip with radius of curvature of 10 nm. (a) All components of the tip are visible: the cantilever, conducting epoxy, and Pt(.8)Ir(.2) wire. This tip has nice cylindrical symmetry. (b) The apex of the tip is the highest point.	96
Figure 7.1	Schematic of the proposed experiment. An STM tip will probe vortices in an superconducting antidot patterned on a topological insulator to search for Majorana modes [51]. Figure from Dr. Stuart Tessmer.	98

Chapter 1

Introduction

This thesis is organized as follows: After I briefly introduce the major topics covered in my thesis experiment, topological insulators, I will begin to discuss my apparatus and the scanning tunneling microscopy technique in Chapter 2. Chapter 3 will cover a historically motivated background of the physics of topological insulators and the topological insulator I studied, Bi_2Se_3 . Chapter 4 covers both my thesis experiment, spectroscopy on the surface of Bi_2Se_3 , and the analysis. Then I go on to discuss other observations on scanning tunneling microscopy studies on Bi_2Se_3 samples in Chapter 5 before I completely change topics to discuss other scanning probe techniques I performed in Chapter 6. Finally, I will conclude with a summary of my experimental observations and analysis and discuss future directions in Chapter 7.

1.1 Topological Insulators

Undoped semiconductor materials are normally insulators. Figure 1.1 (a) shows the standard electronic structure, consisting of a filled valence band and an empty conduction band. The

bands are separated in energy by a band gap as shown in Figure 1.1 (a). The reason a semiconductor cannot support a current is because of the filled valence band. Every electronic state in the band has a twin state with the opposite sign in momentum-space (k -space). In other words, for every electron that could transport current to the right, there is a twin that carries current to the left. Since all of the states are filled (i.e. occupied), there is no way to build a quantum state that will carry an overall current in any one direction.

The quantum Hall effect was discovered in 1980. When a large magnetic field is applied perpendicular to the two-dimensional conducting plane, a quantized current is established on the edges, with the interior becoming an insulator [1]. This current is robust against backscattering; in other words, a charge cannot rebound from a defect in a way that would change its direction. A topological invariant, called a Chern number, distinguishes the quantum Hall insulator from a simple insulator and helps to explain the robust nature of the edge states in the integer quantum Hall effect [2]. It would be years before another boundary state that is protected by a topological invariant would be predicted and discovered.

A topological insulator is a material that is insulating in the bulk but conducting on the surface; it has edge or surface states that are conducting (gapless) that lie inside the bulk gap as depicted in Figure 1.1 (b). Moreover, the surface state, that arises due to strong spin-orbit coupling, traverses this gap is composed of a single (more generally it just needs to be an odd number) pair of eigenstates on each (conduction and valence) band edge which are symmetric under time reversal. These states are known as Kramers pairs or Kramers doublets [3, 4]. However, if there are even numbers of Kramers pairs on each band, elastic backscattering destroys any conducting edge state and it is the topological equivalent of a simple insulator [4]. As long as time reversal symmetry holds, the topological surface state

where electron spin is locked perpendicular to its momentum is robust against scattering. The interplay of momentum and spin is amazing and simple: charge moving to the right must have opposite spin as charge moving to the left.

Much of the research in the last five years has focused on 3D topological insulators. Here, the surface state has an odd number of massless Dirac cones around high symmetry points [5] that are protected by a topological invariant. A Dirac cone is a state that can be described by Dirac's equation where energy is linearly related to momentum. Figure 1.1 (b) shows the topological insulator's Dirac cone where states of opposite sides of the cone (opposite momentum) have opposite spin due to the spin-orbit interactions. Spin orbit interactions are crucial in creating a topological insulator as it gives rise to band inversion that forms the cone [6]. Due to the magneto-electric effect, surface states of topological insulators are described by Maxwell's equations with the addition of a topological term [7]. This gives rise to fascinating properties. For example, theory predicts that bringing an electric charge in close proximity above the surface produces an image magnetic monopole inside the material [8]. Moreover, the interface between a superconductor and a topological insulator can support a particle analogous to a Majorana fermion, a particle which is its own antiparticle. The state created in the topological insulator is actually a particle that is its own hole that could be useful in quantum energy storage [9]. The prospect of these effects is thrilling, but before serious experimental progress can be made in creating and discovering these exotic effects, all the fundamental aspects of the material including bulk effects need to be characterized to avoid experimental complications later.

For example, Bi_2Se_3 is a narrow band gap semiconductor that has been studied for years. Previous interest in these narrow gap semiconductors came from their thermoelectric

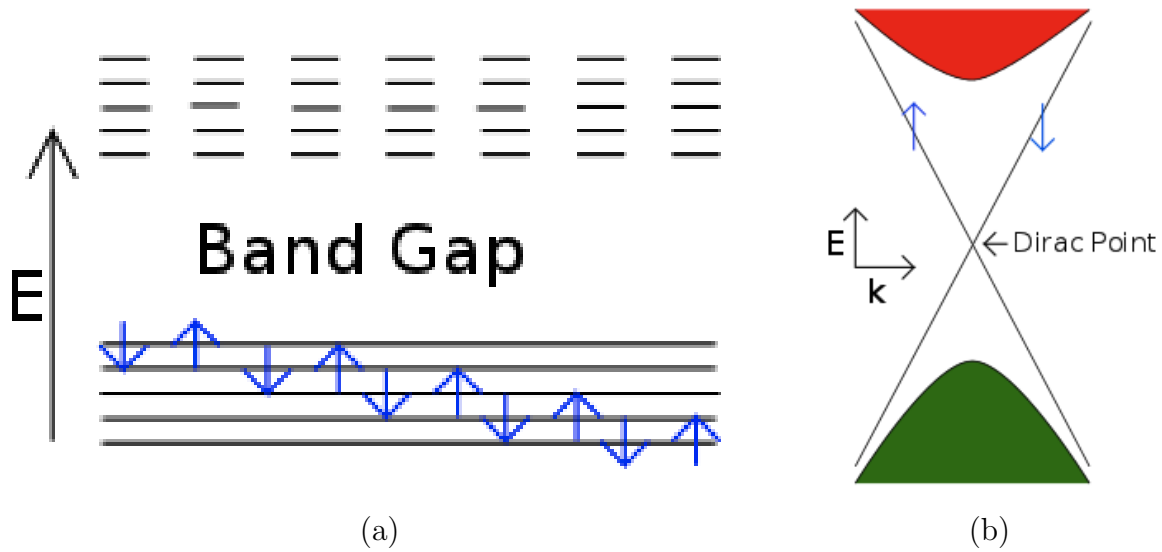


Figure 1.1: For interpretation of the references to color in this and all other figures, the reader is referred to the electronic version of this dissertation. Arrows in these diagrams represent spin. (a) Band diagram of an insulator showing the filled valence states are separated from empty conduction band states by a band gap. The bands are spin degenerate. (b) In a topological insulator, a surface state connecting the conduction and valence band consists of a band where holes traveling left (negative in k -space) are connected to electrons traveling right, and vice versa exists within the gap. In (b) the horizontal scale represents momentum, but there is no physical meaning to the horizontal scale in (a).

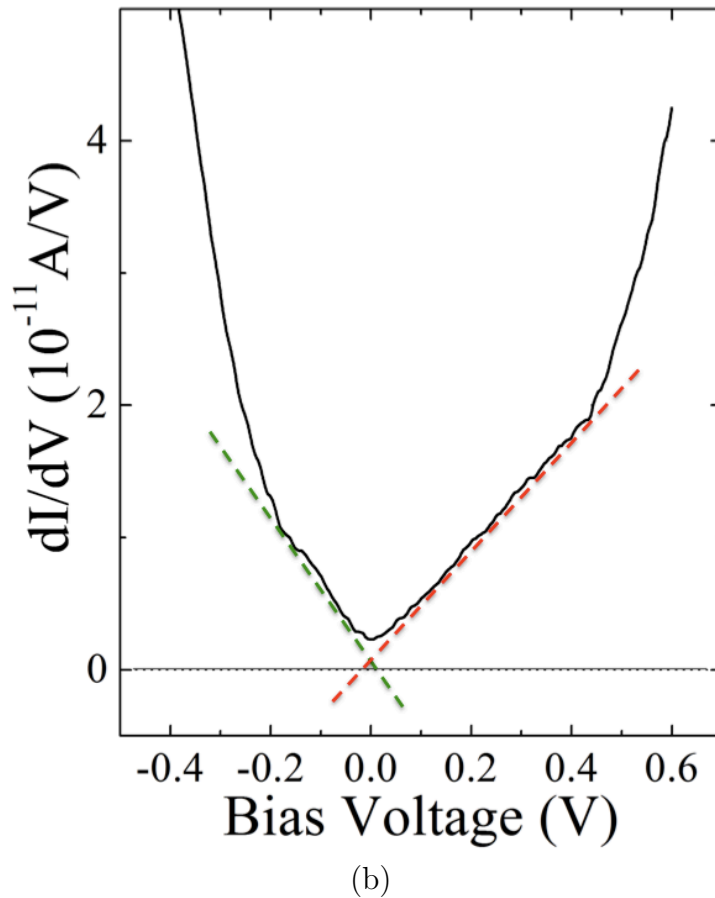
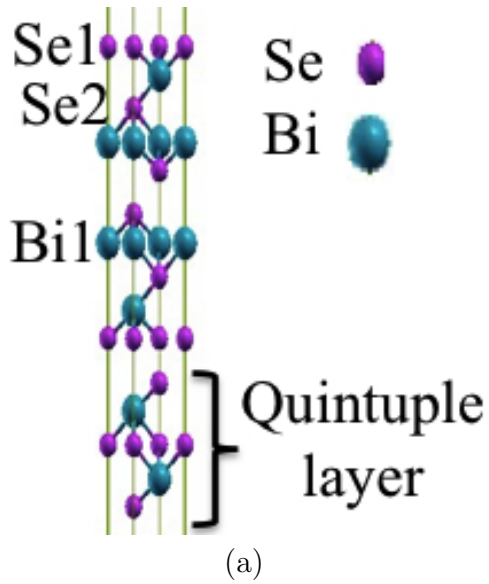


Figure 1.2: (a) Three quintuple layers of Bi_2Se_3 . Inside each layer the atoms form covalent bonds and each layer is held to its neighbor by Van der Waals forces. This image is from of Dr. Mal-soon Lee. (b) My Bi_2Se_3 local density of states measurement. The dotted lines show the Dirac cone. Specific features of the Dirac cone will be discussed in Chapter 4.

properties [10, 11, 12]. It was not until recently that Zhang *et al.* predicted Bi_2Se_3 , Bi_2Te_3 and Sb_2Te_3 to be strong topological insulators while their sister material, Sb_2Se_3 , was predicted to be a trivial insulator [6]. The topological surface state arises from strong spin orbit coupling that induces a p -orbital from Bi and Se to invert giving the surface state a finite skin depth [6]. Bi_2Se_3 has a single, nondegenerate Dirac cone at the Γ point (where $\vec{k} = \vec{0}$ in k -space), making it a very simple topological insulator [6, 13].

Bi_2Se_3 forms a quintuple layer of three Se nets sandwiching two Bi layers as shown in Figure 1.2 (a). The quintuple layers are held together weakly with Van der Waals forces; therefore, these materials are very attractive for STM because they cleave easily with scotch tape and the surface stays relatively clean. Prior work in our group showed that a Bi impurity five lattice sites down from the surface can show up in topography scans [14]. My research took a different approach to study point spectroscopy far from defects to see what unexpected interactions appear in the electronic structure seen in Figure 1.2 (b). I find that bulk states propagate to the surface and that the Dirac cone coexists with a two-dimensional electron gas. Neither of these effects have previously been described by scanning tunneling spectroscopy measurements.

1.2 Scanning Probe Methods

In 1982, Binnig and Rohrer [15, 16] revolutionized surface science bringing surface probes to the angstrom scale by inventing the scanning tunneling microscope (STM). A conducting tip is attached to a piezoelectric material that can expand and contract in all three spatial dimensions. This not only helps to bring the tip to within a nanometer of the surface, but also facilitates raster scans for topographical images. Without the ceramic piezoelectric

materials, the microscope would not have had the ability to scan precisely at the atomic scale. Once in tunneling range, controller electronics keep the tip from running into the surface by maintaining either a constant current or constant height using a feedback mechanism. The tunneling current, usually around 1 nA, is amplified and processed by a computer. By taking a series of these measurements an image of the electronic state of the surface is generated.

Tunneling between two metals separated by an insulating barrier had been understood for years before the advent of STM [17, 18, 19]. However, the popularity of the scanning tunneling microscopy technique fueled further interest in the area experimentally and theoretically [20, 21, 22]. Early research not only focused on studying different materials but also on creating different STM designs including the louse [23], single tube scanner[24], the beetle[25], and, a decade later, the walker [26]. Many different materials were scanned including metals [27], semiconductors [15], and biological materials [28]. Since its inception, it has been used to study many different areas of condensed matter physics. Topics of interest include superconductivity[29], charge density waves[30], atomic manipulation[31], and surface lattice structures[32].

Other techniques using the same mechanical principles as STM have splintered off to form many different sorts of measurements. Moreover the principles behind the scanning probe techniques had been the subject of research for years prior to the advent of precisely controlled piezoelectric devices. For instance, Kelvin probe measurements were well understood [33], and performing them in tandem with STM was a natural extension. As another example, scanning capacitance methods can measure single dopant molecules under a surface [34, 35, 36, 37], often used in conjunction with STM. Needless to say, over the past 30 years, scanning probe techniques have become a scientific staple.

Chapter 2

Apparatus and Technique

In this chapter, I will explain my apparatus and the scanning tunneling microscopy (STM) technique. I will begin by detailing the design parameters of the sample processing chamber that I made to achieve better sample surface quality for my thesis experiment. Then I will explain the physics of STM before explaining the details of my experimental setup.

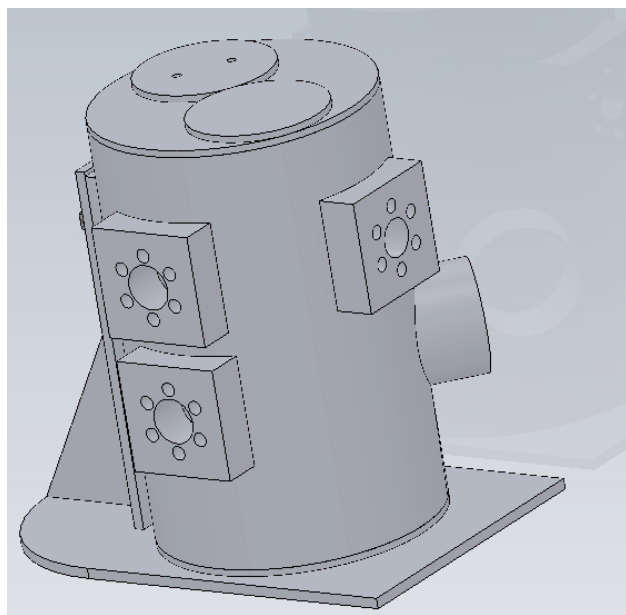
2.1 Sample Processing Chamber

Early in the experimental process as I started to attempt measurements on Bi_2Se_3 , I determined that exposing the sample to air for any length of time was detrimental to the surface quality. It is likely this contamination results from water or hydrocarbons in the air attaching themselves to the surface. I solved this problem by designing a nitrogen gas sample-cleaving chamber. To be successful, the chamber needed to maintain a nitrogen environment at all times. The sample must be loaded directly from the chamber onto the STM using a loading fork so it could be immediately placed under vacuum. These constraints dictated the geometry of the chamber. In order to ensure cleaving was easy to do and see, we used a tall

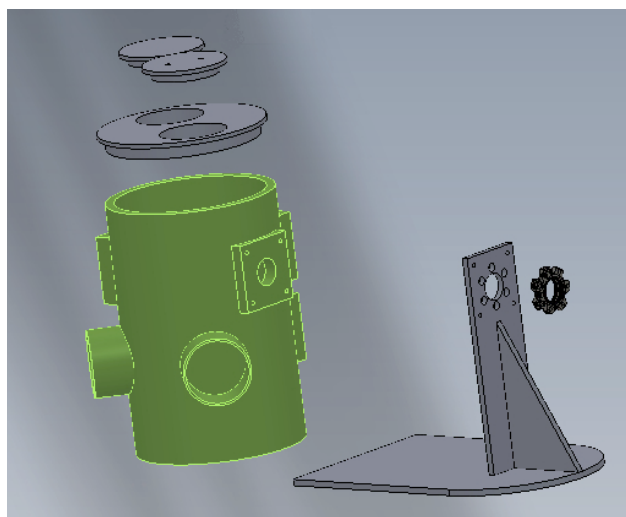
plexiglass tube. Tools needed to be easily loaded into the chamber. To that end, I included standard size ports on the back to which additional apparatus could be attached without breaking the nitrogen environment. The chamber included a removable lid and within the lid there were capped loading ports that could similarly be repurposed.

Figure 2.1 shows the chamber design. In addition to its excellent optical properties, plexiglass is easy to glue and is more durable than other materials with similar optical properties. All access port supports were likewise of plexiglass to prevent any leaks that might occur from trying to glue two unlike materials together. The entire central chamber tube is 14 inches tall and 10 inches in diameter to provide adequate work space. The arm access tubes in the front of the chamber are 4 inches in diameter to accommodate large hands. The lid and its inserts are sealed with vacuum grease to allow easy access for removing apparatus (for example: tape dispensers). Extremely large materials could be transferred through the main lid if required. The other small access port has two holes that allow nitrogen gas to continuously circulate through the chamber. Finally, the entire chamber tube is mounted on an aluminum support that provides adequate strength to hold up the transfer fork without compromising the integrity of the chamber.

After it was built by the machine shop, the chamber was attached to the cryogenic STM system shown in Figure 2.2. To minimize the cleaving chamber's air exposure, a sample loading chamber was added to one of the ports in the back of the nitrogen cleaving chamber. Nitrogen was then continuously circulated through both chambers and vented into the main laboratory to ensure all air remains purged from the system at all times. The only time the main chamber gets exposed to laboratory environment is when the gloves are changed or large items need to be removed or added. The quality of the sample surfaces and subsequent



(a)



(b)

Figure 2.1: My processing chamber. (a) The back of the chamber showing the exit to the microscope and two ports. The top port goes to a pressure relief valve that prevents the chamber from exploding the top off and exposing the contents to air. The lower port connects to a loading chamber so that the main chamber is always under nitrogen. (b) The top shows two access ports: one is for loading materials too big to come in through the loading chamber. The other supports the tubes that allow nitrogen to come in and out in a continuous flow through the chamber. The two protrusions are the glove ports. All of these tubes and lids are made of plexiglass to allow maximum light within the chamber. The support structure on the right is made of aluminum and provides the strength to support the loading fork.

data improved greatly with the addition of the cleaving chamber!

2.2 Scanning Tunneling Microscopy and Spectroscopy

Scanning tunneling microscopy operates on the principle of quantum tunneling through two conducting materials separated by a vacuum or air barrier. If the tip-sample separation is $\sim 5 \text{ \AA}$ and a voltage is applied to the sample relative to the tip, a picoamp or nanoamp scale tunneling current develops that is sensed with the help of a preamplifier. Without an applied voltage, electrons would freely tunnel from one side to the other and no net current would develop. In its most common operation mode, the tip can raster over a surface with the help of a feedback loop that keeps the tunneling current constant. By monitoring how far the tip is extended or contracted to maintain the current at each position in the scan range a computer builds up a topograph of the surface.

The simplest quantum-mechanical model of STM is a trapezoidal one-dimensional barrier of width d separating the sample and tip. A visual representation of this model can be seen in Figure 2.3 where the surface of the sample is taken to be at $z = 0$. The electronic wavefunction, $\psi(z)$, is governed by the one-dimensional time-independent Schrödinger equation:

$$-\frac{\hbar^2}{2m} \frac{\partial^2 \psi(z)}{\partial z^2} + U\psi(z) = E\psi(z) \quad (2.1)$$

where m is the electron mass, \hbar is Plank's constant divided by 2π , U is the average barrier height and E is the electron energy. $U - E$ is an effective barrier to overcome for tunneling. While outside the barrier, the solutions of the Schrödinger equation are sinusoidal. However, inside the barrier the wavefunction decays exponentially. The tunneling current is then

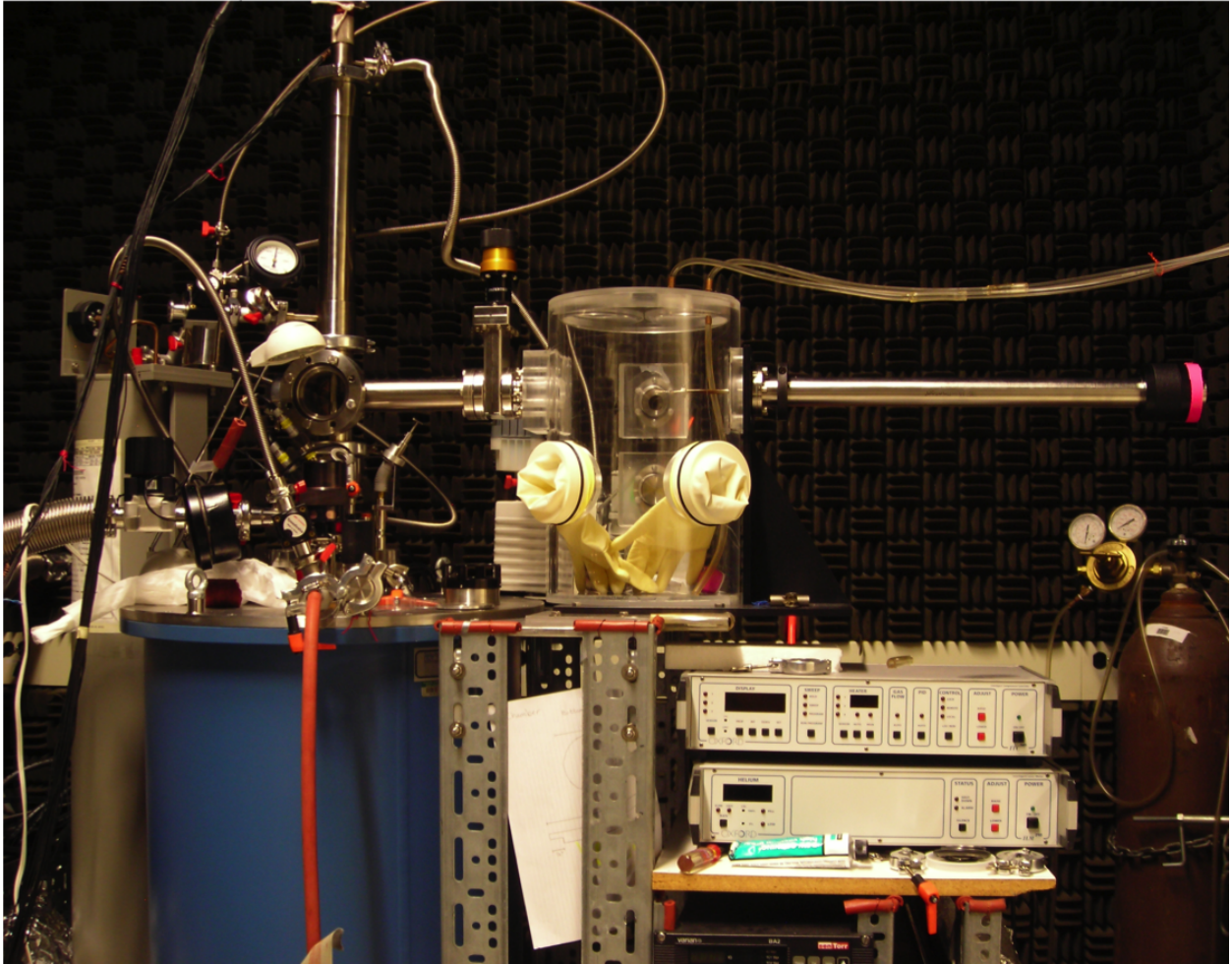


Figure 2.2: My experimental setup. The blue dewar in the lower left of the image is my cryogenic system discussed in Section 2.3.3. The sample processing chamber is in the center of the image with yellow gloves. The fork for transferring the sample is inside the steel tube to the right on the image (and has the pink marker on its end). The sample loading chamber is not visible as it is behind the nitrogen chamber itself.

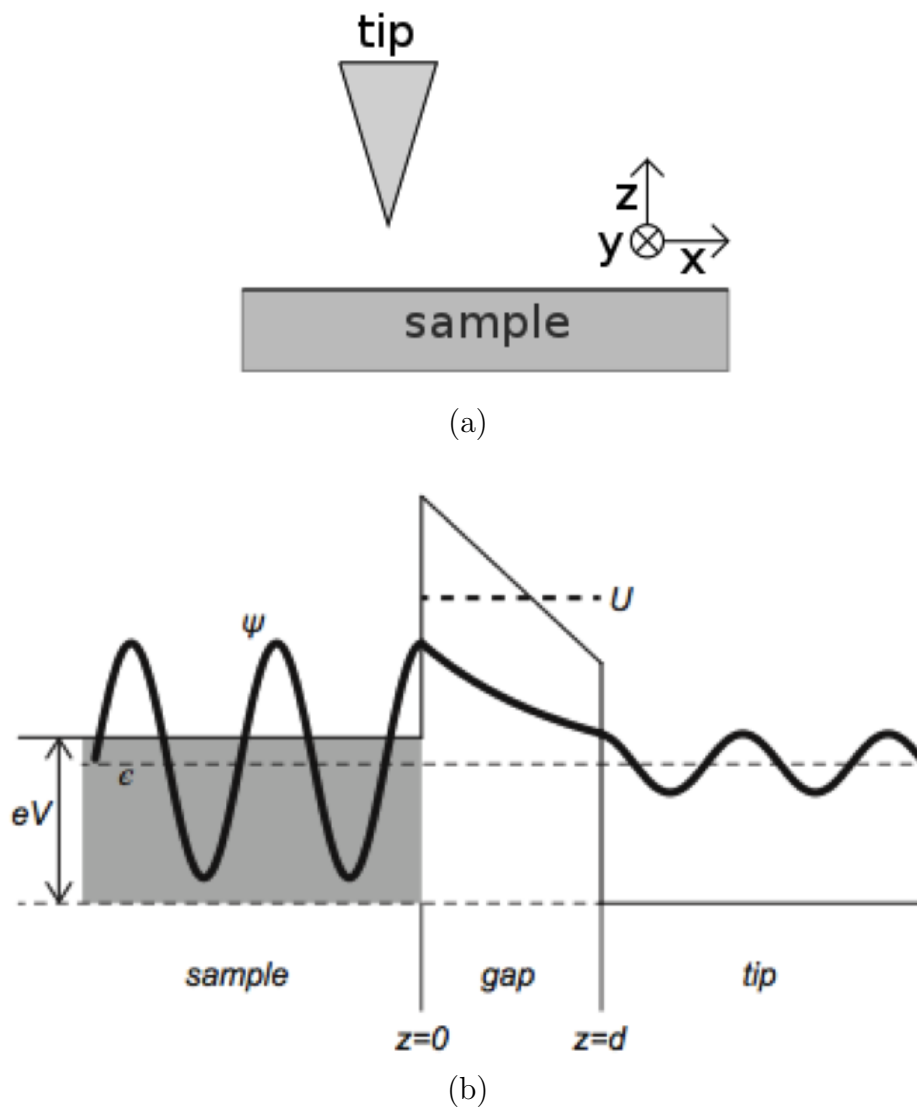


Figure 2.3: (a) Schematic of the tip and the sample. The sample is in the x - y plane and the tip is hovering above the sample in the z -direction. (b) A model of tunneling barrier showing the wavefunction decays exponentially in the gap [38].

proportional to the transmission probability through the classically forbidden gap; as ψ decays exponentially, so does the transmission probability which turns out to be:

$$I \propto \sum_n |\psi(0)|^2 e^{-2\kappa d}, \kappa = \frac{\sqrt{2m(U-E)}}{\hbar}. \quad (2.2)$$

This result highlights the importance of the width of the gap on the magnitude of the tunneling current. The constant, $\kappa = 0.51\sqrt{U-E} \text{ \AA}^{-1}$. Assuming the effective barrier (or work function) for platinum is 5 eV [39, 40], retracting the tip 1 \AA reduces the tunneling current by an order of magnitude. The success of STM at producing informative topographs is largely due to this exponential dependence on distance.

2.2.1 Physics

The coplanar tunneling barrier model of STM is particularly good at highlighting the importance the tunneling gap has on the current; however, it leaves out a lot of information about the surface and tip. In reality, the pointed shape of the tip affects the tunneling and while a realistic picture is perhaps too complex for this thesis, other models exist that relate the tunneling current to intrinsic material properties with few assumptions. In most cases, tip sample coupling is weak, and first-order perturbation theory can capture more of the picture. In other words, the proximity of the tip induces only a small change in the sample electronic wavefunctions, and vice versa. In this approach first put forward by Bardeen in 1961 on metal-insulator-metal systems[19], the tunneling current, I , is related to a tunneling

matrix element, M , between the tip and sample wavefunctions:

$$I = \frac{4\pi e}{\hbar} \int_{-\infty}^{+\infty} [f(E_F - eV + \epsilon) - f(E_F + \epsilon)] \rho_{tip}(E_F - eV + \epsilon) \rho_{sample}(E_F + \epsilon) |M|^2 d\epsilon. \quad (2.3)$$

Here, V is the bias voltage (the applied potential difference between the tip and sample), E_F is the Fermi energy, $f(E)$ is the Fermi distribution function, $\rho(E)$ is the density of states, and ϵ is the energy of the electrons. Equation 2.3 can be simplified when the thermal contribution, $k_B T$, in the Fermi distribution function is smaller than any significant features in the density of states. Then the Fermi function can be approximated by a step function and the tunneling current can be approximated as:

$$I = \frac{4\pi e}{\hbar} \int_0^{eV} \rho_{tip}(E_F - eV + \epsilon) \rho_{sample}(E_F + \epsilon) |M|^2 d\epsilon \quad (2.4)$$

So we see that the tunneling current is related to the density of electronic states of the tip and the sample. Provided the tunneling matrix does not change much at low energies around the Fermi level [17, 18], it can be assumed constant. Tersoff's and Hamann's [40] further simplification of Equation 2.4 by assuming that the tip's density of states is constant over the energy range of interest, which is reasonable for low voltages applied to metals [39, 40]. If the conduction electrons at the apex of the tip have a spherically symmetric wavefunction (an s-orbital on the tip) then Equation 2.4 becomes

$$I \approx \frac{4\pi e}{\hbar} \rho_{tip} |M|^2 \int_0^{eV} \rho_{sample}(E_F - eV + \epsilon) d\epsilon. \quad (2.5)$$

Therefore, a more accurate perspective on STM measurements is that all the electronic states from the Fermi level up to eV in the sample contribute to the tunneling current:

$$I \propto \int_0^{eV} \rho_{sample}(E_F + \epsilon) d\epsilon. \quad (2.6)$$

In other words, each position on the topograph is composed of all the electronic density of states that exist between the material's Fermi level and the applied bias energy, eV . When a surface feature, like an atom, has more accessible states than its surrounding environment, it will appear brighter. Varying the bias voltage is a good way to distinguish between features that are actually topography and those that are due to additional electronic states in that region. Suppose there is a localized defect atom with defect states at a particular energy. Once you scan below a voltage where the defect states are not active, the enhancement will disappear. Atomic protrusions, step edges, and other physical features remain.

Semiconductors samples are a bit more complicated. Tunneling out of the valence band is not necessarily the same as tunneling out of the conduction band. This can lead to voltage dependent images if the tunneling electrons are part of the conduction band or valence band. In GaAs [21, 20, 41] at positive voltages only the gallium atoms show up as enhancements in the scan because conduction band electrons are more localized on gallium. Negative voltages reveal the arsenic atoms. You only get the full picture of topography if you look at both positive and negative voltages. However, Equation 2.6 still holds provided the bias is much less than the work function [42].

In addition to surface topography, STM can be applied to probe the electronic spectrum of the sample. Scanning tunneling spectroscopy measurements at low temperatures essentially show the local density of states as a function of energy. We can see this by taking

the derivative of the proportionality in Equation 2.6 with respect to voltage produces an expression for dI/dV , also known as the tunneling conductance:

$$\frac{dI}{dV} \propto \rho_{sample}(E_F + eV) \quad (2.7)$$

dI/dV can be found by measuring I vs. V at a single sample location (i.e. while the tip is stationary) and numerically differentiating the result to find the slope at all voltages. However, to improve the signal to noise ratio, the local density of states can be measured directly using a lock-in technique and applying an oscillation to the voltage as the voltage is ramped over the energy range of interest. A comparison of different dI/dV curves at various spots on the same material is necessary to look at local changes in the density of states. Because the magnitude of the resulting curve depends directly on the tunneling gap, dI/dV is usually plotted with arbitrary units.

If the bias energy, eV , does become a significant portion of the tunneling barrier, then the simple picture in Equation 2.7 no longer holds. At these large voltages, the tunneling matrix elements becomes exponentially dependent on voltage and cannot be considered constant [39]. Fortunately, there is a painless and simple solution to normalize the dI/dV spectrum by I/V to get $d \ln I / d \ln V$ and remove the exponential dependence on voltage (some authors refer to this quantity as the logarithmic density of states). In this work, the relevant voltages are low and this normalization is not required.

2.2.2 Calibration

After a piezoelectric tube cracked, I rebuilt the microscope and it was necessary for me to calibrate it to determine the piezoelectric tubes' sensitivity. To that end, I used two standard

samples. Graphite's well-established atomic spacing provided an excellent way to calibrate the scanning tube in the x-y dimensions. The z-direction calibration was performed on a sample composed of a grid of conducting platinum pits of known depth. Figure 2.3 (a) shows the x, y and z directions with respect to the sample.

2.2.2.1 Graphite

Highly oriented pyrolytic graphite is a layered material of carbon atoms arranged in a hexagonal honeycomb pattern. Layers of graphite are bonded via weak Van der Waals forces, allowing a fresh layer to be easily cleaved by scotch tape. As seen in Figure 2.4 (a), only every other atom in the hexagonal lattice is visible in an STM image. Thus the carbon atoms appear to be in a triangular pattern. Step edges are a good way of determining if you have a very blunt tip that only has a few atoms protruding. A smeared step edge image means the tip is less than ideal. Spectroscopy on graphite can indicate if there is anything electronically active on the tip and demonstrate that it is a good metallic conductor. My routine was to use the graphite spectrum like those in Figure 2.4 to determine the quality of the tip before taking measurements on Bi_2Se_3 . The I-V curve for graphite is not quite linear and the density of states is a characteristic u-shape typical of the material as shown in Figure 2.4 (c).

2.2.2.2 Pt Pits

The platinum pit calibration sample consists of a grid of evenly-spaced square pits of 180 nm depth. Each pit is $5\ \mu\text{m} \times 5\ \mu\text{m}$ and separated from the next pit by $5\ \mu\text{m}$ in each direction. My microscope's maximum scan range is just over $5\ \mu\text{m}$, so it is rare to be able to image both edges of the pit at one time. Nevertheless, a corner is sufficient for calibrating the

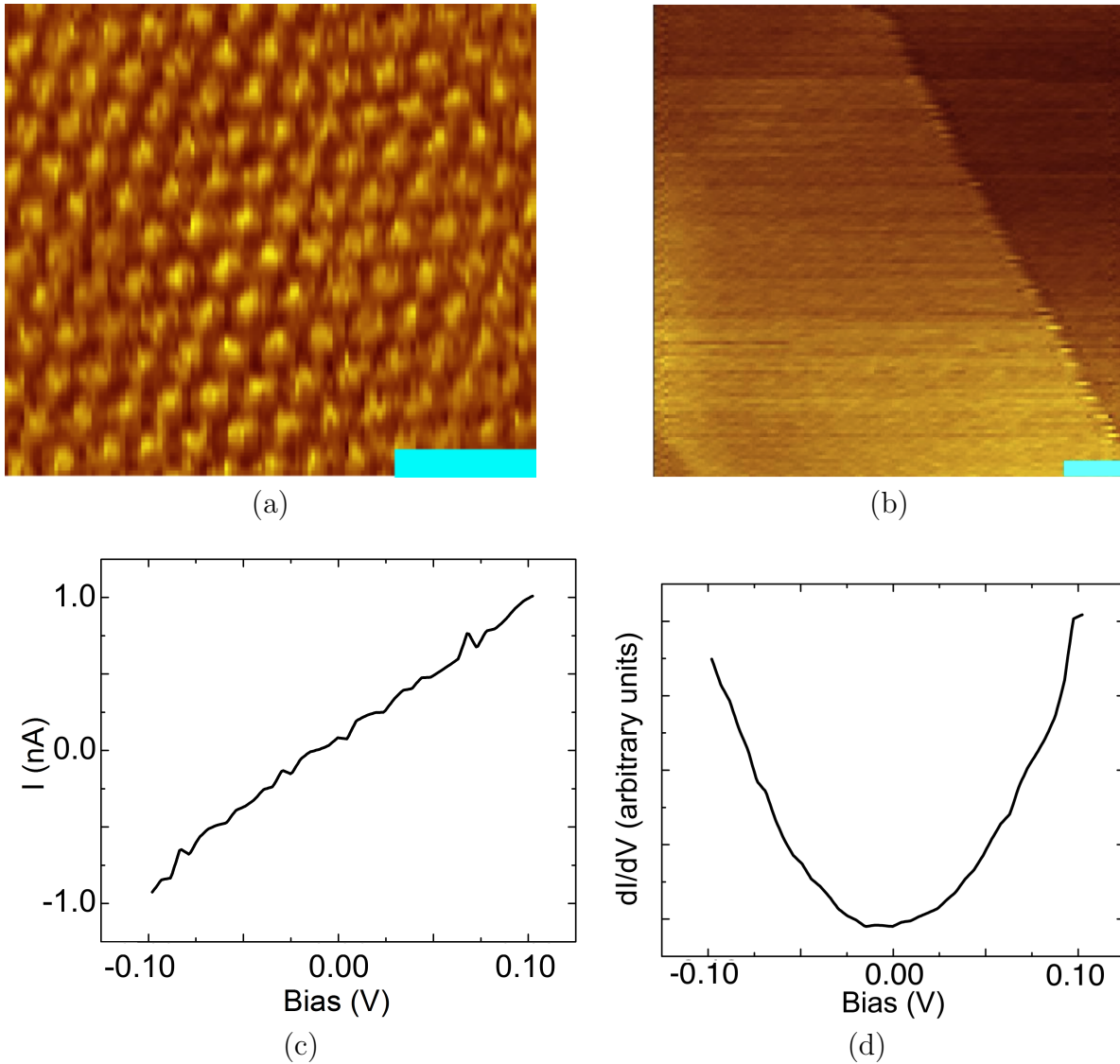


Figure 2.4: (a) Graphite atoms at a 1.0 nA tunneling current and 0.1 V bias. The scale bar is 500 pm. (b) This is an image of step edge of graphite. The spectra shown in (c) and (d) were taken on the smooth part of the image. Because the scale of this image is so much larger than (a), individual atoms are not resolved. The scale bar is 200 nm. (c) Shows linear I-V curve on graphite. (d) Density of states measurement on graphite.

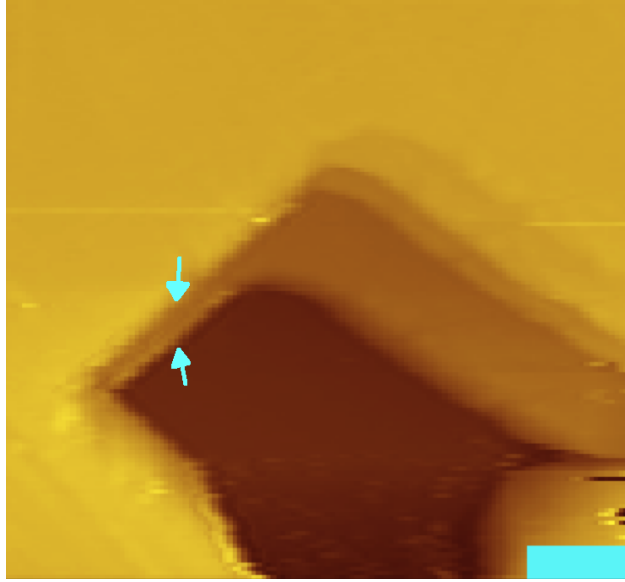


Figure 2.5: Pt pits sample where the scale bar is $1 \mu\text{m}$. The pit is $5 \mu\text{m} \times 5 \mu\text{m}$ and 180 nm deep. There is at least a double tip, possibly a triple tip in this case giving rise to multiple apparent edges as indicated by the arrows.

vertical (z) extension of my scanning tube. A calibration image is shown in Figure 2.5. The tip used to create this topography image is at least a double tip, and possibly has more tips around the side. The edge of the pit comes in pairs, indicating a double tip. We can see this in the image. For example, the upper-left part of the pit shows two edges as indicated by the arrows in Figure 2.5. This indicates that the left part of the tip has a double apex. Even with the multi-tip, the pit is confirmed to be 180 nm deep comparing the center of the pit to the edge.

2.3 Experimental Constraints and Setup

2.3.1 Besocke Type STM

The STM I rebuilt was of the Besocke type design(also known as the beetle), which consists of three carrier piezoelectric tubes that support the sample and one central scanning tube

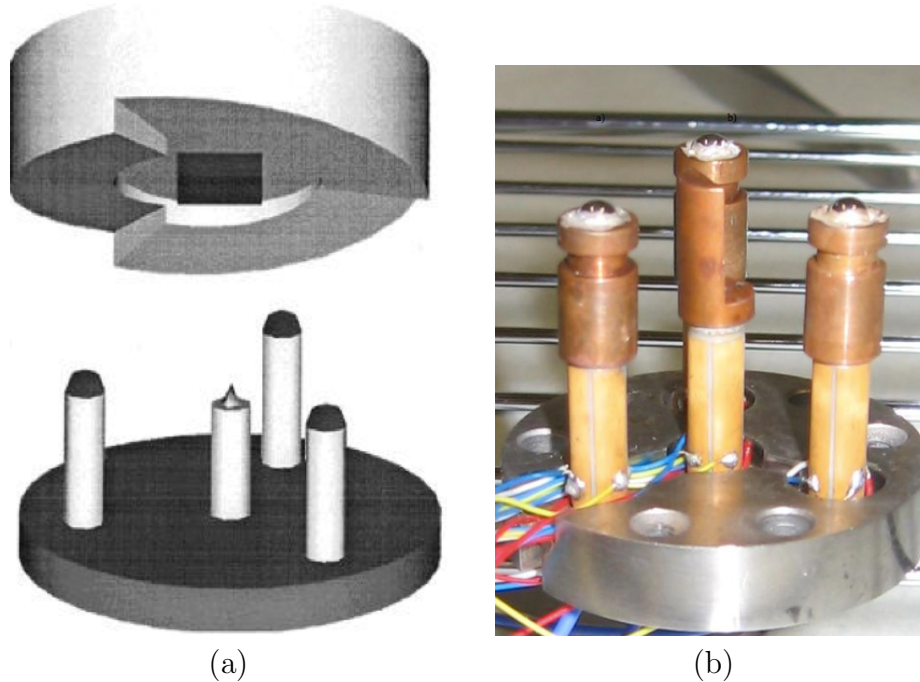


Figure 2.6: (a) Besoke design microscope where three piezoelectric tubes support a sample and a central tube scans the tip. (b) My microscope outside of its protective case.

seen in Figure 2.6. The three carrier piezoelectric tubes are responsible for fine positioning the sample and bringing it into tunneling range. During approach a sawtooth waveform is applied to these carrier tubes which slowly extend in the direction of twisting necessary to bring the sample into tunneling range and then quickly snap back to a neutral position. Friction keeps the sample in place during the slow movement and the fast return leaves the tubes supporting a slightly lower part of the sample ramps in what is called a stick-slip type approach [25]. After each cycle of the sawtooth, the scanning tube retracts during this fine approach and extends to determine if it is within tunneling range. The control program halts the approach as soon as tunneling current is detected.

The main advantage of the design is that all identical tubes are attached to a rigid base-plate, giving excellent mechanical stability [25]. Scanning range is determined to a large extent by the tube's geometry. A tube with thicker walls is more robust against vibrations,

but has a smaller range than a longer, thinner tube. To counter thermal drift during measurements, all four tubes are identical. The Besocke design has a stable construction that helps produce quality STM images.

2.3.2 Noise Isolation

Moreover, because the tunneling current is exponentially dependent on distance, vibrations on the scale of angstroms can have a large effect. When imaging something on such a small scale like atoms, even small vibrations can impair the ability to get a sensible image. There are two main sources of vibrations: sound (acoustic) and building vibrations (mechanical). To ensure minimal interaction with sound vibrations, the room is covered in polyurethane acoustic foam. More constant sources of mechanical vibration are from the building, which tends to shake at low frequencies (10-20 Hz). To isolate the system from the building vibrations, the microscope is mounted on four pressurized air springs and four optical table legs to decouple it from the floor. Lead bricks weigh the entire platform to decrease its lowest normal-mode frequency to about 1 Hz. Because this is far from the building frequencies, we see very little noise in the system due to building vibrations.

2.3.3 Cryogenic System

My STM is attached to the end of a stainless steel probe so that it can be lowered into a low temperature environment. The cryogenic system I used for my experiments is a standard Oxford Instruments refrigerator capable of operating at liquid ^4He and ^3He temperatures. My primary thesis data was acquired at liquid ^4He temperatures. The dewar itself consists of an inner sample tube sealed off from the probe entry port by a gate valve, as seen in Figure

2.7. Surrounding the tube is an inner vacuum chamber that can serve to insulate the sample tube from a surrounding main cryogen bath. As I always used the main bath to cool the sample tube directly, the inner vacuum chamber always had a small amount of exchange gas to ensure adequate thermal contact between the sample tube and the main bath. A transfer tube entry port on the top of the dewar allows easy access to the main bath through which to transfer the cryogen. To ensure efficient cooling, the main bath is thermally insulated by a outer vacuum chamber that also has mylar batting to help reflect heat from the outside.

In typical operation, the sample space is purged of all air to reach pressures of around 2×10^{-6} torr. The vacuum not only ensures the cleanliness of the surface of the sample, but also preserves the purity of the sample space within the dewar from contaminants. A ^4He exchange gas in the sample tube within the dewar helps the microscope equilibrate to the temperatures quickly.

Cooling the microscope is a process that takes several hours. It is important not to thermally shock the fragile ceramic piezoelectric tubes. To monitor the microscope's temperature, an Allen-Bradely resistor acts as method of gauging the temperature. The carbon-composite resistor has a resistance that changes significantly with temperature and has therefore been calibrated to act as a low temperature thermometer. Once the microscope is firmly seated in the bottom of the dewar, it is left to equilibrate overnight to avoid any thermal drift.

2.3.4 Tips

The quality of the tip on the STM is probably the biggest variable in the entire experiment. An important experimental consideration is the material and electronic structure of the tip;

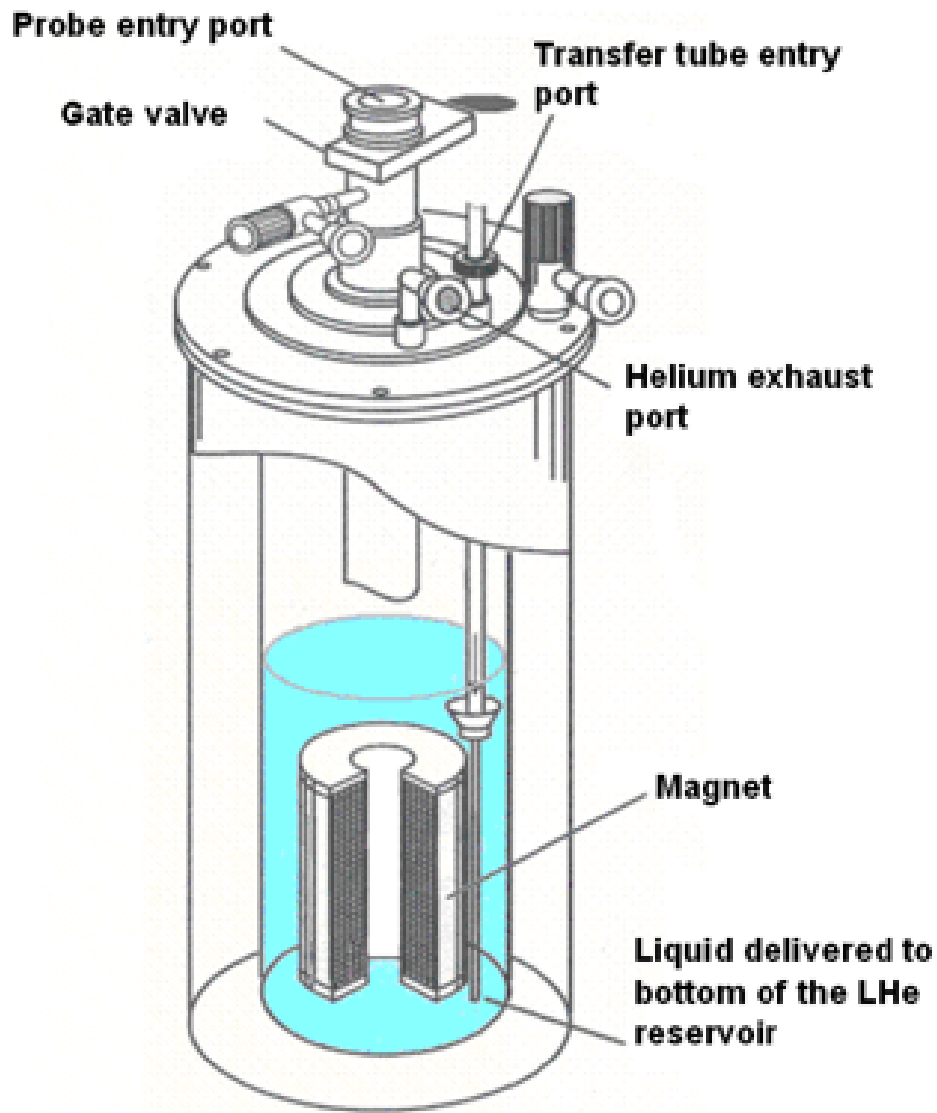


Figure 2.7: Diagram of the cryostat. The microscope mounts on the probe entry port and is isolated from the sample tube by a gate valve until it is under vacuum. The microscope can then be lowered slowly into the bottom of the dewar. The system is cooled by a main bath of nitrogen or helium. The transfer tube entry port is the site where liquid is transferred into the system. Gas from liquid boil off is released through the helium exhaust port [43].

when performing spectroscopy the resulting spectrum is a convolution of the density of states of the tip with the sample. I chose to use a metallic PtIr tip which has a flat density of states near the Fermi level and is chemically inert to avoid those problems. This choice is not critical: gold or tungsten tips would have been adequate. While performing measurements, I took great care to keep the tip free of any other material to ensure the integrity of the measurements. I used manually cut tips most often because they are convenient to re-cut and renew the apex. A more detailed discussion of tip preparation is in Section 6.4.

2.3.4.1 *In situ* Tip Cleaning Techniques

Even when I took great care to ensure the integrity of the apex of the tip, sometimes the tip became unstable. This can happen spontaneously during a scan or there may be a precipitating event, such as a crash. It is therefore extremely important for STM to have a variety of tools to rid the tip of the offensive particle or flake of foreign material on the apex.

The first tool I generally employed was shaking the tip. While the tip is far enough above the sample that there will be no chance of interaction between them, the tip is moved as quickly as possible over a large area in a raster pattern in hope that the offensive particle will be shaken loose. This technique is least damaging to the tip and the sample and has a good success rate for loose particles. For slightly more stubborn particles on the tip, I found a flat, clean spot on the sample and slowly dragged the tip over the surface with a high set tunneling current to reduce the tip sample separation. Both of these *in situ* approaches are safe to use during STM and capacitance measurements.

The most firmly attached particles might require field emission or evaporation to pull them off the tip. Some of the most clingy particles attach themselves to the tip during spectroscopy as I continuously ramp the voltage over a fixed point on the sample. The

smaller the voltage, the less aggressive the approach. For the most persistent particles, I would typically position the sample just out of tunneling range to widen the gap so that there is no possibility that the tip will smash the sample. With the tip grounded, I would then apply 150 V to the sample for five seconds before coming back into tunneling range at a new location on the sample. The only complication with this technique is that the fields involved can be strong enough to loosen a flake off a layered sample thus interacting with the tip and making the situation worse. This technique is so successful at removing particles from the tip that it also has a tendency to blunt the apex. However, a blunt tip is often better for spectroscopy, even if it is worse for resolving small length scales. When there is a lot of resources and time invested in a particular data run, including cooling the microscope, trying several methods to recover a tip *in situ* is justified.

If all else fails, the procedure to change the tip first involves slowly warming up the microscope. Then the entire microscope can be moved to the bench top to unsolder the mounted tip. It is possible that the existing tip can simply be recut with wire cutters, soldered back on, and retested for suitability. However, if the radius of curvature of the tip is important (and it was not for the thesis experiment described in Chapter 4) then it may be necessary to attach a tip that has been characterized by Scanning Electron Microscopy (SEM) to a new chip with conducting low-temperature epoxy. Before re-cooling the microscope, every tip must be tested at room temperature on a freshly cleaved sample in nitrogen to ensure its stability. If the tip has additional features in the density of states or cannot readily be used to produce high-quality images, then it is discarded and replaced before ever being used at low temperatures. Under ideal circumstances, warming the microscope, replacing the tip and re-cooling takes three days.

Chapter 3

An Introduction to Topological Insulators

In this chapter, I will set up the physics necessary to understand the conclusions in the next two chapters. I have taken a historical approach to the topic and will therefore include some discussion of materials like graphene that are not what I probed. However, these topics will help to explain key ideas related to topological insulators. I will then explain topological insulator physics and give an overview of the literature of a prototypical topological insulator, Bi_2Se_3 , to help you understand how my main result fits in with the overall picture.

3.1 Background

Over the last 80 years, band theory of solids has been a fruitful area of study in Condensed Matter Physics. One of the ways to model the static electronic structure of a crystal is using the tight binding model. This model captures the quantum mechanics of the lattice by treating electrons as tightly bound to the atoms in the lattice, analogous to atomic orbitals

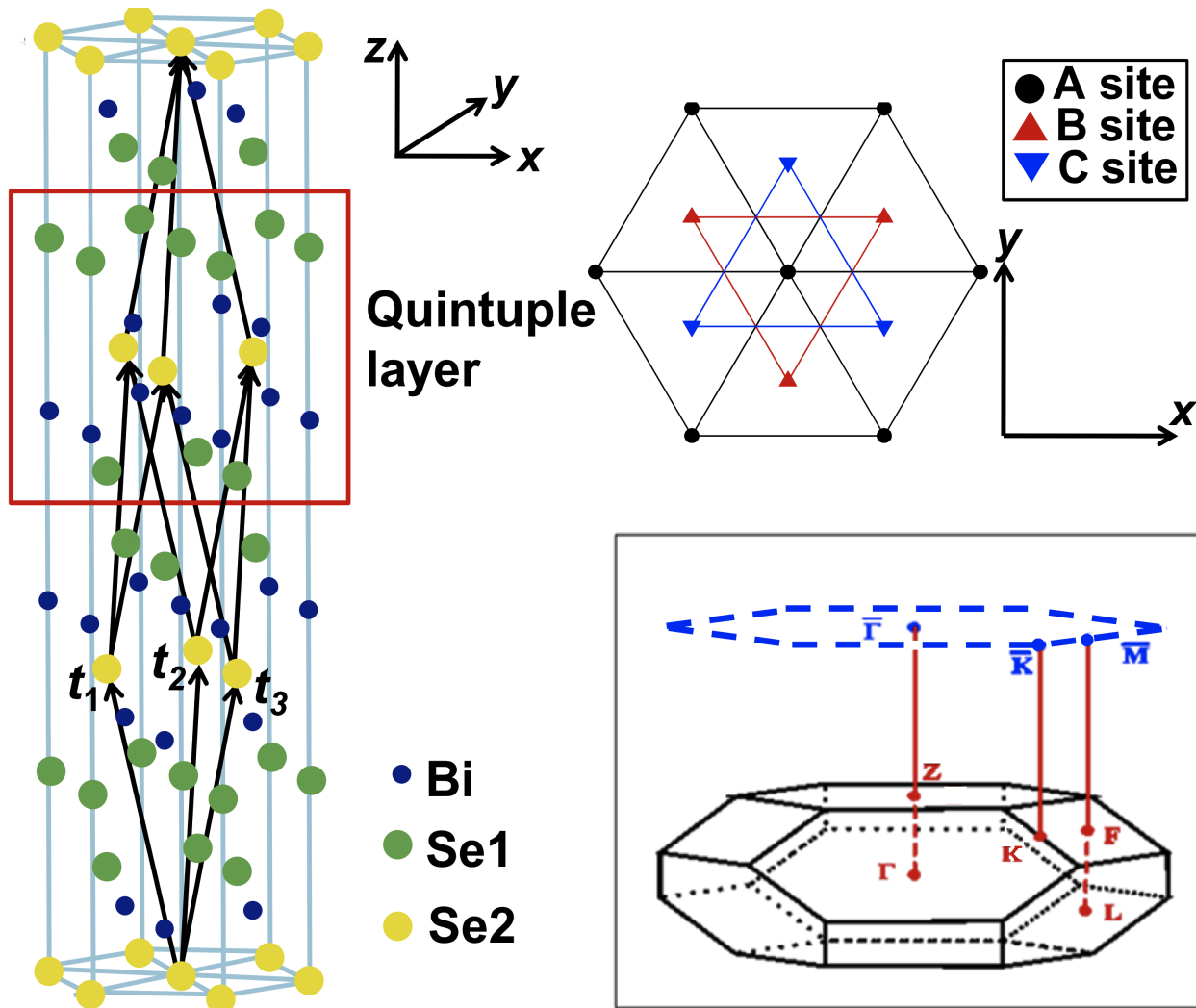


Figure 3.1: Figure from Zhang *et al.* [44] shows the unit cell in a crystal lattice of Bi_2Se_3 . Primitive vectors \vec{t}_1 , \vec{t}_2 , and \vec{t}_3 show equivalent translation vectors of the lattice. There are 3 inequivalent sites in the lattice, Bi, Se1 and Se2 that stack in inequivalent layers C(Se1)-A(Se1)-B(Bi)-C(Se2)-A(Bi)-B(Se1)-C(Se1). Viewed from above, this looks like a hex lattice with inequivalent layers marking out triangular lattices. In the bottom right, the three-dimensional unit cell is mapped out with its two-dimensional projection showing high symmetry points in k -space, Γ , M and K that are time reversal invariant momentum points for this crystal structure. Used under Creative Commons Attribution 3.0 Unported (CC-BY) license and all credit for creation of this figure goes to [44].

in isolated atoms. It is useful for situations when there is some overlap between atomic orbitals in a lattice, but the states are not extended enough that treating the atomic orbitals is irrelevant. As such, interactions with other electrons is limited; often only nearest neighbor hopping is considered [45].

The atomic positions in the crystal are mapped out in what is called a unit cell—the fewest number of atoms arrangements needed to make one repeating unit of the crystal. This structure can be transformed to find the reciprocal lattice called the Brillouin zone. Instead of atoms being mapped into real space, the structure is converted to momentum (k) space [45]. Momentum space highlights the importance of certain high symmetry directions in the crystal and these points are assigned letters. An example of a crystal and its reciprocal lattice is given in Figure 3.1. Its unit cell and primitive vectors of translation are drawn on the lattice in black. On the left part of the figure is a rhombohedral lattice supercell and its momentum space with 2D projections of both the lattice and the Brillouin zone [44]. Because of its layered structure, one unit cell must cover multiple layers to fully reproduce a crystal.

In the simplest case, ignoring spin for now, the tight-binding Hamiltonian consists of a hopping term to capture how electrons move between nearest-neighbors:

$$H = -t \sum_{n,n'} [\Psi_n^\dagger \Psi_{n'} + h.c.], \quad (3.1)$$

where Ψ and Ψ^\dagger are the annihilation and creation operators respectively. The indices n and n' refer to nearest-neighbors only, and the sum is therefore between nearest-neighbor pairs. The coefficient t dictates the strength of nearest neighbor hopping arising from lattice

potential effects. If it is 0 then no hopping will occur [45]. The strength of this hopping term may vary depending on which atomic orbitals are involved. d and f orbitals have strongly bound electrons that would make hopping less probable. Because they are usually the orbitals participating in the conduction and valence bands respectively, s and p orbitals would have a higher probability to hop to the nearest neighbor [46]. Electron wavefunctions are mapped out in to what are called Bloch wavefunctions to capture the lattice periodicity. Bloch waves have a plane wave component that captures the electrons' movement through free space and a component that captures the periodic potential from the lattice, $u_{n\vec{k}}(\vec{r})$. The wave functions appear as:

$$\psi_{n\vec{k}}(\vec{r}) = \exp^{i\vec{k}\vec{r}} u_{n\vec{k}}(\vec{r}) \quad (3.2)$$

where subscript n stands for the n -th electron state, \vec{r} are real-space vectors, and $\epsilon_n(\vec{k}) = \epsilon_n(\vec{k} + \vec{K})$. Here, $\epsilon_n(\vec{k})$ is the eigenenergy of the Hamiltonian defined by $\psi_{n\vec{k}} H = \epsilon_n(\vec{k}) \psi_{n\vec{k}}$. Bloch's theorem dictates that $\psi_{n\vec{k}}(\vec{R}) = \psi_{n\vec{k}}(\vec{r}) e^{i\vec{k}\vec{R}}$ and is one full translation in k space through a 2D band. Unless spin orbit coupling is explicitly added into Equation 3.1, any band calculated will be doubly degenerate [45].

3.1.1 Graphene Model

While my thesis experiment only encompasses the material Bi_2Se_3 , I have taken a historical approach to motivate the physics of topological insulators necessitating an explanation of a graphene model and the quantum spin Hall effect. First there will be a brief explanation of the quantum Hall effect and its topologically protected electronic surface state.

Electrons in the quantum Hall effect form edge states due to the large magnetic field that

are then impervious to backscattering. In the presence of a magnetic field, Hall conductance becomes quantized in unit conductance of $\sigma_{xy} = \nu e^2/h$ [47, 2] where ν is an integer. The quantum Hall conductance is fundamentally different from conduction through a normal metal and therefore represents a state of matter that is topologically different than other conduction states. To distinguish materials exhibiting the quantum Hall effect from normal insulators, Thouless, Kohmoto, Nightingale, and den Nijs developed a topological invariant, ν , called a Chern number or Chern invariant. This number is a way of distinguishing band structures that can be deformed into one another from those that cannot. It is a quantity that is robust against perturbations. From a theoretical perspective, perturbations are smooth deformations of the Hamiltonian. From an experimental perspective, materials of dissimilar Chern numbers have some conserved quantity that can be measured to high precision. A material that exhibits the quantum Hall effect, for example has a quantized Hall conductance that remains quantized even when defects are introduced into the system. However, the world is full of materials that do not exhibit quantized conductance and never can be made to do so. Another example of a Chern number is given in the following pages.

More recently, there arose interest in the quantum spin Hall effect, in part due to the scientific interest in spintronics applications. Unlike the quantum Hall effect, the quantum spin Hall effect does not require a magnetic field and is time reversal symmetry invariant due to spin-orbit interactions [4, 48, 49]. The quantum spin Hall effect has spin split edge states that counter-propagate on the edges. While the total current through this state is zero, the spin current has unit spin conductance $\sigma_{xy}^S = e/2\pi$ [50].

Because graphene is a 2D sheet of carbon atoms arranged in a hexagonal lattice, the discussion will focus on the 2D tight binding model of the quantum spin Hall effect in graphene.

These material bands require relativistic effects to calculate key band structure features. Spin-orbit coupling can result in time reversal invariant (\mathcal{T} -invariant) spin-dependent forces in a lattice. One such tight binding Hamiltonian which includes spin and spin-orbit coupling was introduced by Kane and Mele [48] for graphene.

Graphene is a two-dimensional material that has a hexagonal Brillouin zone where there are two inequivalent, K and K' points that form two triangular sublattices. When Kane and Mele [48] solved the tight binding model with spin-orbit interactions for a strip of graphene, an edge state emerges from the bands. Edge states with opposite spins travel in opposite directions, a sort of “spin filtered” state. The bands in k -space shown in Figure 3.2 (a) show the edge state in the bulk insulating gap of graphene that traverses the gap. These states persist so long as the spin-orbit term in the calculations dominates. Two states at $k_x = \pi/a$ form a Kramers doublet that is protected from any time reversal symmetric perturbations and are thus protected from elastic backscattering [4]. The linear relationship of the states that traverse the gap is relativistic.

For a band insulator, the surface states connect edges of like spins and no state traverses the gap. However, for the topological insulator in Figure 3.2 the spins switch partners across the gap while preserving spin. Therefore, the edge states are spin split. In fact, the state supported is predicted to be the quantum spin Hall state that carries a quantum of spin conductance. For this spin split, or “helical,” state to be a topologically distinct from an insulator, a single pair of spin-split edge states crosses the gap [50]. In a sense, the resulting edge state is half a metal in that only half the spins of a normal metal can travel in a direction. It is far more robust than a metal because electron’s states are extended and not impacted in the presence of disorder by Anderson localization. Moreover, it turns out that

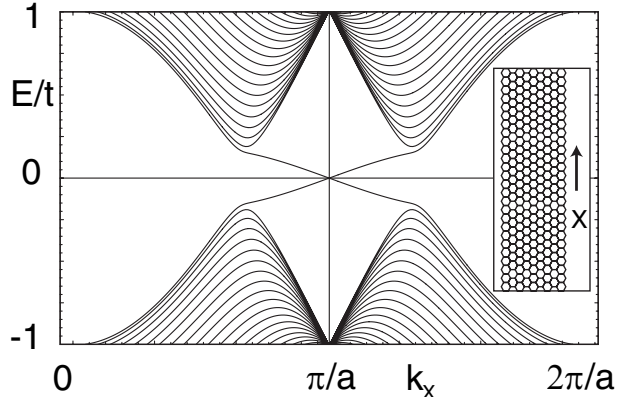


Figure 3.2: A calculation from Kane and Mele [48]. A single pair of edge states traverse the bulk insulating gap due to spin orbit coupling in a band structure calculation from a tight-binding model on a strip (in the inset) of graphene. Reprinted figure with permission from Kane, C.L. and Mele, E.J., *Physical Review Letters*, 95, 226801(2005). Copyright (2005) by the American Physical Society. Abstract can be viewed at: <http://prl.aps.org/abstract/PRL/v95/i22/e226801>.

an insulator can be one of two distinct things, a band insulator or a topological insulator [4, 51]. (This relates to a classification called the “ Z_2 index”).

The nature of the electrons on the surface of graphene is part of the states appeal. As the states cross in Figure 3.2 they form an “x” where energy and momentum of the band are linearly related as is the case for massless particles in free space. For this reason, the electrons are often called “relativistic.” At the center of the cross is a point called the “Dirac point” where both spins coexist with the same energy and absolute value of momentum. This point is protected by both inversion and time reversal symmetry [51].

Time reversal symmetry necessitates the existence of high symmetry points where $\vec{k} = -\vec{k}$. This typically happens at $\vec{k} = \vec{0}$ and on the band edge [5] and are called “Kramers degenerate points.” Figure 3.2 has a high symmetry point when $ka = \pi$. Away from these points, spin-orbit coupling causes the bands to split. Consequently, the topological state has an odd number of band crossings, while a simple insulator has an even number. The number

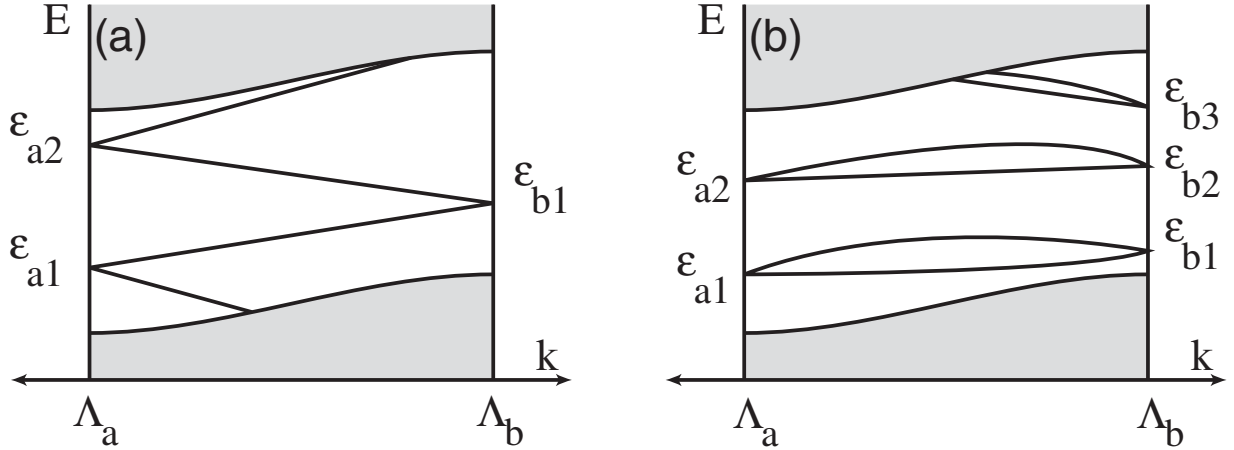


Figure 3.3: A schematic band structure showing Kramers pairs traversing the gap from Fu *et al.* [52]. (a) A schematic of a topological insulator that has an odd number of Fermi level crossings. (b) A schematic of a simple insulator that has an even number of crossings. There are still degenerate points at Λ_a and Λ_b but they are not topologically protected against deformation. Reprinted figure with permission from Fu, Liang and Kane, C.L., Physical Review B, 76, 045302 (2007). Copyright (2007) by the American Physical Society. Abstract can be viewed at: <http://prb.aps.org/abstract/PRB/v76/i4/e045302>.

of band crossings is the Chern number [53, 5]. Figure 3.3 illustrates the difference between simple insulators which have an even number of doubly degenerate pairs in the gap in (b) and a topological surface state with a single crossing in (a). Because these crossings cannot be deformed into one another, they are topologically distinct [52].

In summary, the tight binding model with spin-orbit coupling predicts many of the hallmarks of 2D topological insulators. (It predicts a Z_2 classification for topological insulators). There is a spin split edge [51] that is protected by time reversal symmetry that is robust against perturbation [48, 4, 49, 5, 52, 54, 7, 8]. Inside the insulating gap are relativistic edge states. The resulting quantum spin Hall effect has quantized spin currents on the surface where the currents of opposite spins move in opposite directions [4, 51].

3.1.2 HgTe/CdTe Wells

Subsequent experiments on graphene showed that its spin-orbit coupling was too weak to support a quantum spin Hall state [51]. Instead, the focus shifted to heavy elements known to have high spin-orbit coupling. Bernevig *et al.* [55] successfully predicted the existence of the quantum spin Hall state in HgCdTe quantum well structures that would be the first realization of the quantum spin Hall phase. They first predicted that placing HgTe, which has an inverted band structure with the p level above the s level, between a “normal” semiconductor band structured material, CdTe, would result in the quantum spin Hall state [55, 51]. Spin-orbit coupling in the Hg atoms make the band inversion happen. The state would only exist as long as the well width was above a critical well width of 6.3 nm. Below this critical width the normal band structure associated with the CdTe would persist through the well. However, above the width, the bands invert resulting in a quantum phase transition from a trivial insulator to a topologically protected quantum spin Hall insulator [51].

Konig *et al.* [56] performed transport experiments that first realized the quantum spin Hall state experimentally by measuring the conductance due to the edge states. Figure 3.4 shows the resistance measurement of their results. Below the critical width in sample I the resistance shows insulating behavior with the resistance on the order of $10^7 \Omega$. However at two well widths above the critical dimension, the quantum spin Hall state with a conductance $G = 2e^2/h$ associated with the top and bottom edges is realized. This was the first measurement of the quantum spin Hall state.

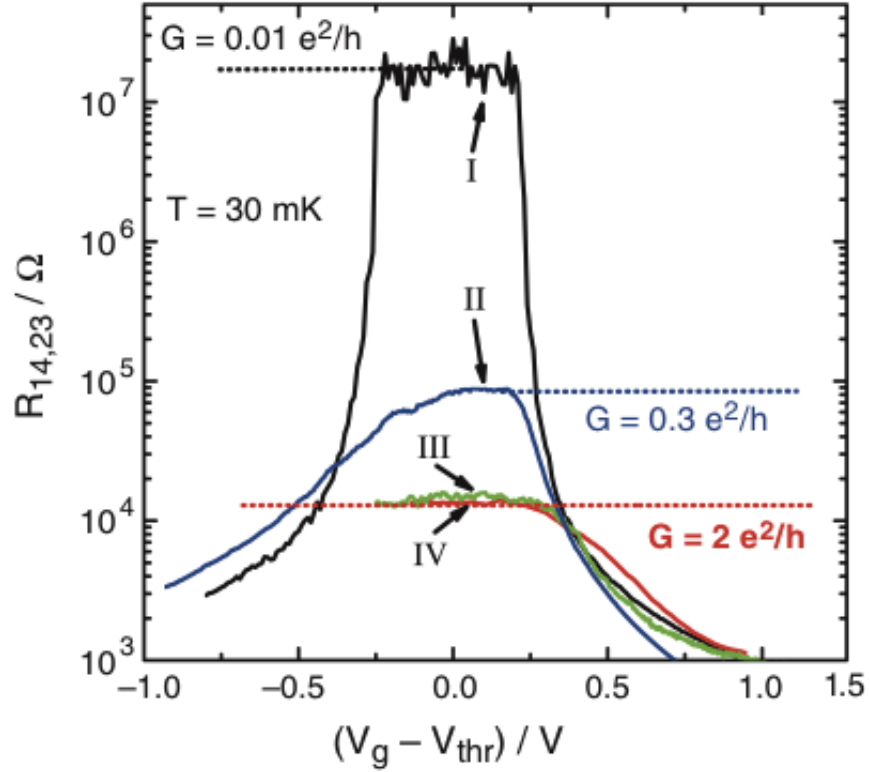


Figure 3.4: Figure adapted from König *et al.* [56]. Resistance measurement of CdTe/HgTe quantum wells that support the quantum spin Hall state. Sample I shows that the wells are insulating below the critical width. Sample II shows disorder due to temperature effects. Samples III and IV show that the conductance is precisely equal to $2e^2/h$ for two different well widths above the critical dimension. From M. Koenig, S. Wiedmann, C. Bruene, A. Roth, H. Buhmann, L. W. Molenkamp, X.-L. Qi, S.-C. Zhang, *Science*, 318, 766-770 (2007). Reprinted with permission from AAAS.

3.1.3 Three Dimensional Topological Insulators

While 2D topological insulators can be distinguished by a single Chern number, three dimensions adds three more integer Chern numbers, one for each of the xy , yz , and xz planes [5]. While this leads to several different possibilities, they can really be divided into three categories: simple insulator, weak topological insulator, and strong topological insulator. Strong topological insulators have a Chern number $\nu_0 = 1$ and corresponds to an odd number of Kramers pairs on the surface. A trivial and weak topological insulators have a Chern number $\nu_0 = 0$ [5, 57].

Edge states no longer have the same meaning once you extend a discussion to three dimensions. Although there are three other Chern numbers that only arise in three dimensions, only ν_0 is independent of the reciprocal lattice primitive vector, and therefore does not depend on the reciprocal lattice direction. If $\nu_0 = 0$ the material can be a trivial insulator or a weak topological insulator. A trivial insulator has either 0 or 4 number of Dirac points enclosed by the Fermi surface. The states in a trivial insulator are extremely localized and not topologically protected.

One way to extend a two-dimensional material into three dimensions is to create a stack of the two-dimensional material. This does create a state that has topological protection in one dimension. However, because it is not topologically protected in the direction the stack was built, this state is “weak” such that disorder will destroy it [52, 57]. A two-dimensional Fermi surface modeling the stack would enclose two Dirac cones, one from each 1D edge state. However, there is another way to extend to three dimensions. If the Fermi surface encloses a single Dirac cone there will be an odd number of band crossings in any direction in k -space [52]. Thus it is topologically protected because a single band crossing cannot be

transformed into any other state without first closing the gap. Such a state can arise due to spin-orbit coupling and is called a strong topological insulator [57]. The strong topological insulator has an odd Chern number and $\nu_0 = 1$. Like a quantum spin Hall state, a strong topological insulator is robust against defect scattering due to its topological protection. It forms a two-dimensional layer on the surface of a strong spin-orbit coupling material. Amazingly, momentum and spin are always perpendicular to each other in this topologically protected state [57].

In summary, a three-dimensional strong topological insulator is characterized by a two-dimensional metallic state on the surface of the material. A key idea is that due to spin-orbit coupling, momentum is locked perpendicular to the spin [52, 51, 58, 59]. To form a topologically protected state that is robust against small perturbations, time reversal symmetry must be preserved [52, 59]. The strong topological state supports an odd number of Dirac cones, which means that there can only be an odd number of crossings of the Fermi level [51, 60].

3.1.4 Early Studies on $\text{Bi}_{1-x}\text{Sb}_x$

$\text{Bi}_{1-x}\text{Sb}_x$ was one of the first well studied three-dimensional topological insulators. Bismuth had long been known to be a good candidate for supporting a quantum spin hall phase [50]. The spin-orbit coupling in bismuth is very strong, which helps it support a spin current [61]. Antimony is likewise an element with strong spin orbit coupling roughly about one third of bismuth and serves to tune the spin-orbit coupling strength so that the alloy will be a strong topological insulator by perturbing the bands just enough that they invert [52, 59].

3.1.4.1 ARPES

Hsieh *et al.* experimentally realized the three-dimensional Dirac cone in $\text{Bi}_{0.9}\text{Sb}_{0.1}$. In their work they resolved the five band crossings that distinguished the predicted topological insulating regime where the conduction and valence bands had inverted [60]. The topological insulating phase in a bismuth alloy is significant because when there is less antimony in the crystal, the bands do not invert and the alloy remains a weak topological insulator with an even number of band crossings [59, 52].

3.1.4.2 Quasiparticle Interference Patterns

STM measurements showing snowflake-like scattering patterns really sparked excitement in topological insulators. Modulations in the density of states appear when electrons elastically scatter from the impurities, mixing eigenstates of different momentum, k . These eigenstates mix along quasiparticle contours of constant energy in momentum space [62]. When different momentum states, k_1 and k_2 , interfere after scattering, modulations in the local density of states arise with wavelength $\lambda = 2\pi/|q|$ where $q = k_1 - k_2$. This can be measured with a scanning tunneling microscope; differential tunneling conductance scans in real space expose these modulations called Friedel oscillations. Taking the Fourier transform of the differential conductance image yields the momentum-space information on the wavefunctions. This technique is called Fourier-Transform STS (FT-STs) [62]. In other words, when quasiparticle interactions with the bulk states are sufficiently strong, bulk states can scatter off surface impurities in a way that can be imaged directly by the STM.

$\text{Bi}_{1-x}\text{Sb}_x$ forms a disordered crystal alloy with plenty of opportunities for the topological surface state to scatter off of Sb impurities. The conductance map of Figure 3.5 (a) appears

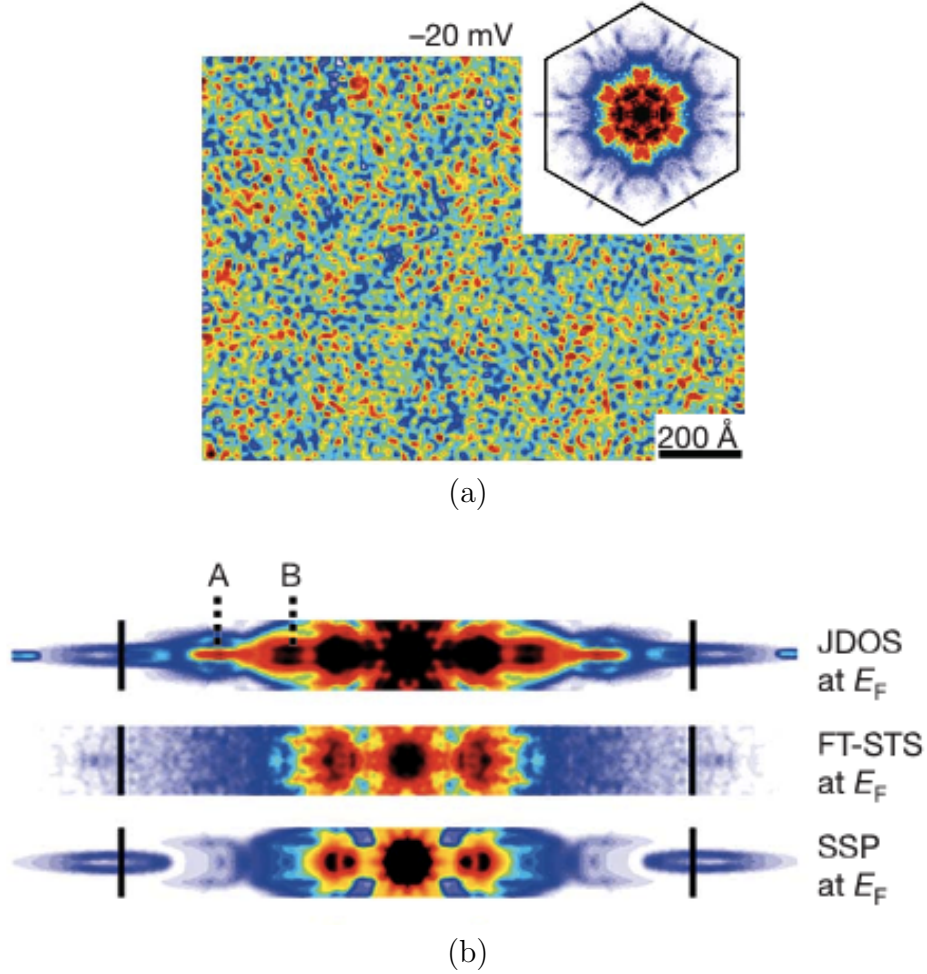


Figure 3.5: (a) Adapted from [58]. Bi_{0.92}Sb_{0.08} dI/dV map with the Fourier transform of the image inset. The snowflake pattern shows the six-fold symmetric scattering in k -space. Some scattering directions are forbidden. (b) Adapted from Figure 4 in reference [58]. The scattering patterns are only duplicated when spin-dependent scattering is accounted for in calculations. Reprinted by permission from Macmillan Publishers Ltd: NATURE (P.Roushan, J.Seo, C.V. Parker, Y.S. Hor, D.Hsieh, D.Qian, A.Richardella, M.Z. Hasan, R.J. Cava, and A.Yazdani. “Topological surface states protected from backscattering by chiral spin texture,” *Nature*, 460, 11061109, (2009)), copyright (2009)

to be quite messy and disordered, but the Fourier transform of the image into momentum space reveals elegant complex snowflake patterns. These intricate scattering patterns cannot be simulated without performing a calculation that use a matrix connecting like spins, suppresses rotations of spins and forbids scattering into opposite spin states in what they refer to as spin-dependent scattering probability (SSP). Figure 3.5 (b) shows that a similar calculation of the joint density of states (JDOS) that does not include spin in any way fails to capture these intricate patterns. The strong topological insulating nature of the material is therefore quite robust against disorder because the spin selective rules hold over distances larger than the disorder [58].

3.2 Bi₂Se₃ Background

3.2.1 Structure

Bismuth Selenide, Bi₂Se₃, is a strong topological insulator with a rhombohedral lattice structure. A layered material, Bi₂Se₃ has covalent bonds inside and each quintuple layer (QL) is held together by Van der Waals forces. Each quintuple layer is approximately 1 nm high [63]. As seen in Figure 1.2, a quintuple layer consists of Se-Bi-Se-Bi-Se bonds. This layered structure makes them ideal for surface experiments, as a new surface can be cleaved with scotch tape to reveal a clean black mirror-like surface, with a single Dirac cone on the surface [6]. This was shown schematically in Chapter 1, Figure 1.1. Figure 3.6 shows the calculated band structure of Bi₂Se₃ including the single Dirac cone that makes it a model topological insulator calculated by Dr. Mal-soon Lee. The computational technique is density functional theory introduced in Section 4.3.

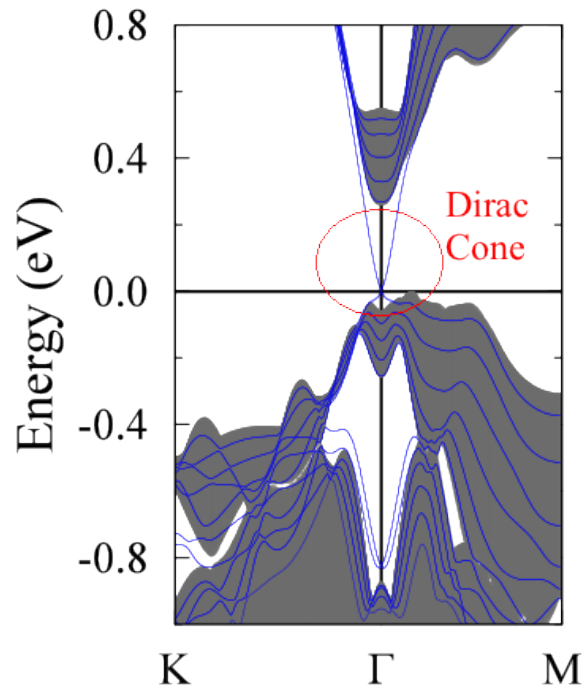


Figure 3.6: Density functional theory calculation of the Bi_2Se_3 bulk [gray] and 6 quintuple layer calculation of the Dirac cone in blue. The single Dirac cone on the surface is circled in red. Figure courtesy of Dr. Mal-soon Lee.

Bi_2Se_3 and Bi_2Te_3 had long been studied for their thermoelectric properties [14, 10, 64]. Because of its interest as a thermoelectric material, many effects that would later be examined for their interactions with the surface state were already known before topological insulators had even been predicted. In 2004, Dr. Sergei Urazhdin was the first to characterize clover-like and triangular defects from Se vacancies and Bi substitutions [14, 10]. Angle-resolved photoemission spectroscopy (ARPES) studies identified the time dependence of the surface state forming on Bi_2Te_3 and attributed it to band bending at the surface [64].

In 2009, Zhang *et al.* [6] did the first theory calculations predicting that Bi_2Se_3 , Bi_2Te_3 and Sb_2Te_3 were strong topological insulators. When spin orbit coupling is added to band calculations, the p_z bands from the conduction and valence band hybridize, inverting the bands and creating a Dirac cone. Since then, there has been keen experimental interest on investigating the topological insulator surface state on these materials.

Bi_2Se_3 has been studied by countless groups trying to realize aspects of the topological insulating state and how it interacts with other physical effects. The helical spin texture in Bi_2Se_3 was realized using circular dichroism ARPES measurements which identified that opposing momentum states also have opposite spin structure [65]. That spin structure persists even at room temperature [66], an important characteristic for spintronic applications. Consistent with its topological protection, the weak electron-phonon coupling experiments show the surface state persists unperturbed [67, 68]. Because there is potential to mix with the bulk, measurements of the Landau levels show that they are suppressed on the left, valence side arm of the Dirac cone and follow uneven spacing consistent with Dirac electrons on the other arm [69, 70, 71, 72] potentially from mixing with the bulk. Transport studies have attempted to reduce the bulk contribution and realize the dissipationless spin current

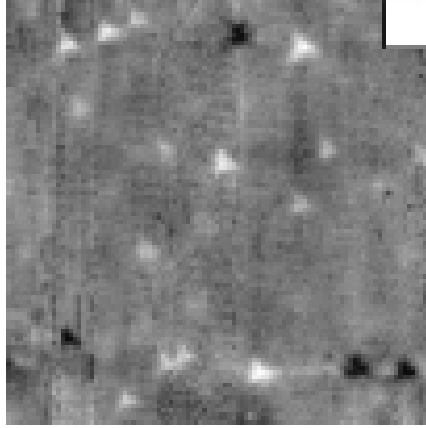


Figure 3.7: Triangular defects on Bi_2Se_3 where the bright triangles are attributed to bismuth on a selenium site substitutions. The scan range is $65\text{ nm}\times 65\text{ nm}$. Topograph from Urazhdin *et al.* [10]. Reprinted figure with permission from S.Urazhdin, D.Bilc, S.Mahanti, S.Tessmer, T.Kyratsi, and M.Kanatzidis. Physical Review B, 69(8):085313, 2004. Copyright (2004) by the American Physical Society. Abstract can be viewed at: <http://prb.aps.org/abstract/PRB/v69/i8/e085313>

for years by various means [73, 74, 75, 76]. Recently, a research group revealed they had realized metallic, ambipolar gapless conduction without any bulk contribution [77]. The charge carriers of the surface state have been examined by optical conductivity measurements [78] and transport measurements [73, 77, 75, 74, 76] have been found to agree. Some groups have focussed their studies on thin films (i.e. [63, 79]) and others on bulk crystals (i.e. [14, 80, 81]) and show weak anti-localization effects. Even ignoring the studies involving dopants, the last four years have been extremely fruitful for research on the Bi_2Se_3 surface states.

3.2.2 Dopants and Defects

Many experiments use doped crystals to look at electronic interactions with the defect states. Non-magnetic elements like Cd [73] and Ca [80, 81, 82, 83, 75] are added to make the sample more p -type to shift the Fermi level toward the Dirac point. This characteristic is desirable in any transport-like measurement and for spintronic applications to realize a completely

spin split state. The dopants can help to realize a dissipationless spin current because local disorder does not destroy the topologic state. Amazingly, copper dopants intercalated into the Van der Waals gap have been shown to create a superconducting state [84, 65].

In order to test how robust the surface state is to magnetic perturbations, magnetic dopants like Mn [80], Cd [73], Cs, Gd, Rb [85], and Co [86] all show the surface state to persist when the magnetic order is weak. However, enough Fe doping can open up a gap and destroy the Dirac cone [51]. Bi_2Se_3 nanoribbons doped with iron exhibit a minimum in resistance associated with Kondo effect [87] but often otherwise leave the topological state undisturbed [88, 81, 89] unless there is magnetic order to open the gap [88].

STM measurements showed how these defect states influence the topography. Dr. Sergei Urazhdin pioneered STM studies on Bi_2Se_3 . He attributed triangular defects seen in Figure 3.7 to bismuth substituted on a selenium lattice site (Bi_{Se}). These triangular defects appear as clovers in differential conductance maps. The shape of the electronic enhancement is attributed to p bonds lining up from the lowest Se layer in the top quintuple layer terminating on the surface with three bright spots and are not of topographic origin [14]. Triangular defect states that do not change the local density of states (LDOS) in their vicinity are attributed to interstitial bismuth between the top two layers locally creating a strain on the lattice [10]. Because the triangular defect states are voltage dependent, they are known to be part of the electronic structure of the material and not topography. These conclusions have been accepted as the most likely explanation of triangles that are just part of the surface and mark the locations of subsurface dopants. STS studies of dopants show they create a resonance within the bulk gap that can obscure the Dirac cone close to the defect [10, 90]. These resonances depend on the location with respect to the defect state's center [10, 90, 89];

the impurity strength diverges as the Fermi level approaches the Dirac point and a pure spin split state is realized [90]. These resonance states can occur at a variety of different voltages relative to the Dirac point depending on how a dopant goes in and its electronic contribution to the crystal.

A resonance state in the spectroscopy measurements relates to the voltage. The triangular defects may appear bright or dark. Se vacancies appear as bright triangles at positive voltages relative to the Dirac point when the state is empty [82, 91] and dark triangles at negative relative voltages [92]. It acts like a double donor [93]. Native Bi_2Se_3 tends to be n-type due to selenium vacancies. Bi vacancies are far less common. Density functional theory calculations on common dopants show that Bi vacancies act like a triple acceptor [93]. These same calculations show that bismuth on a selenium site acts as an amphoteric dopant that is an acceptor for n-type materials, which is consistent with bright triangular defects described in reference [14]. Other dopants like Ca [82] and Cu [84, 94] also show bright triangles at positive relative voltages and are likewise viewed as substitutional dopants.

Unlike $\text{Bi}_{1-x}\text{Sb}_x$ and Bi_2Te_3 , Bi_2Se_3 quasiparticle interference patterns are partially suppressed on the surface and often do not reveal quite as rich patterns. Conductance maps of defects on the surface reveal clover patterns [14], but very few wave patterns. Some groups have speculated that quasiparticle scattering is suppressed by mixing with the bulk state in the helical Dirac fermion regime [95, 96]. These interference patterns can only arise from scattering off defects within the layers that overlap with the topological state [97, 86]. As such, adsorbates on the surface are not responsible for scattering the topological insulating state and topographic features like flakes or warped surfaces can impact quasiparticle scattering [97]. Conductance maps on the surface of related material, Bi_2Te_3 , support this

conclusion by showing standing waves that result from scattering off step edges that show strongly damped oscillations from a step [98]. Once scattered, topological insulating states can decay into bulk states via low energy electron-electron interactions and defect scattering [96].

3.2.3 Surface Potential Fluctuations

On the surface, deep defect states influence the topological insulating state by creating an energy landscape, i.e. potential fluctuations, that influence the surface [80]. While the disorder may locally shift the Dirac point relative to the applied voltage, the topologic surface state persists under the influence of this bulk disorder [80]. Moreover, magnetic impurities break time-reversal symmetry and ought to allow backscattering. However, Beidenkopf *et al.* showed that quasiparticle interference patterns are not altered by the magnetic impurity, Mn [80]. They also showed that quasiparticle interference patterns are suppressed when the average disorder length is approximately that of the topological insulator's interference pattern wavelength [80]. The topological insulating state screens the bulk disorder over approximately 26 nm in Bi₂Te₃ doped with Mn. The minimum of the local density of states, e.g. the Dirac point, shifts in space locally on the surface due to the underlying defect pattern. The Dirac cone and bulk bands are otherwise unchanged by the bulk doping. However, there is an offset of the Dirac cone in tunneling spectroscopy from zero energy. The vertical offset of the Dirac cone has been observed in thin films [79] and bulk crystals [80, 71, 95, 10], but its origin was either ignored [80, 95, 14, 10] or explicitly stated as of an unknown origin [71].

Because the bulk provides other decay paths, it is important to know when the surface

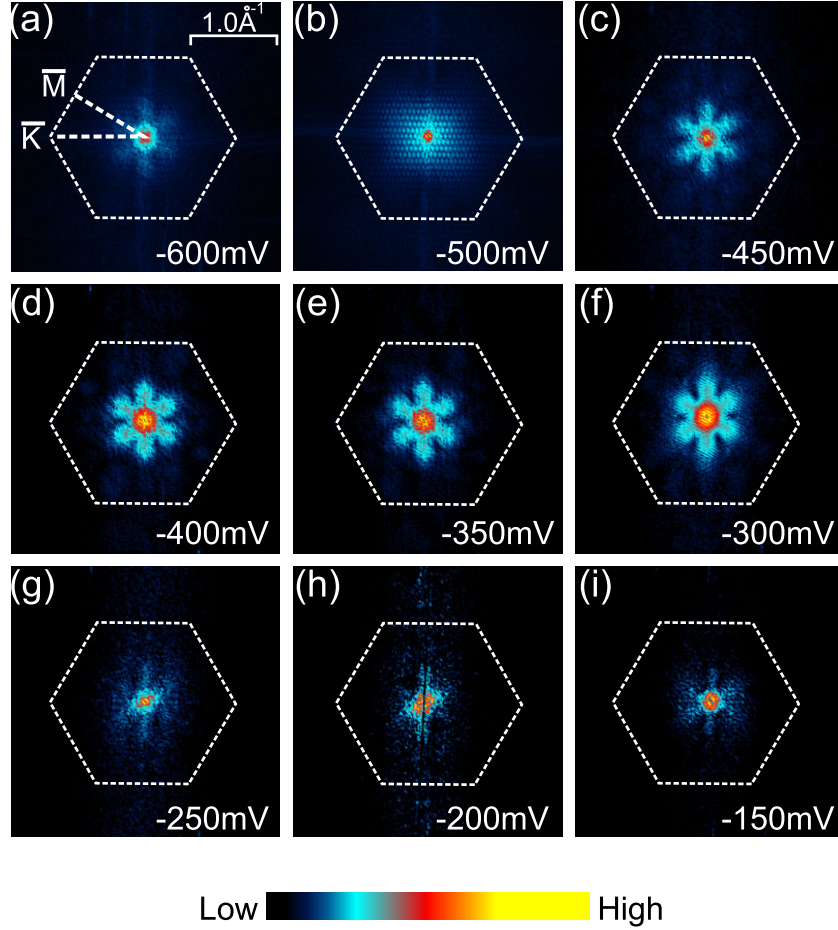


Figure 3.8: Quasiparticle scattering data from Kim *et al.* [95]. The six-fold symmetry gets smeared by the bulk valence band when the voltage is less than -500 meV and by the bulk conduction band when it is greater than -250 meV. Scattering is enhanced in the Γ -M direction and suppressed in the Γ -K. At some voltages, they 6-fold symmetry is less clear. (a) and (b) show the smearing of the topological state due to the valence band and (g)-(i) show the smearing due to the conduction band. Reprinted figure with permission from S.Kim, M.Ye, K.Kuroda, Y.Yamada, E.Krasovskii, E.Chulkov, K.Miyamoto, M.Nakatake, T.Okuda, Y.Ueda, K.Shimada, H.Namatame, M.Taniguchi, and A.Kimura. Physical Review Letters, 107:056803, (2011). Copyright (2011) by the American Physical Society. Abstract can be viewed at: <http://prl.aps.org/abstract/PRL/v107/i5/e056803>.

state interacts with the bulk. Quasiparticle interference patterns from Kim *et al.* suggest that bulk mixing may obscure the quasiparticle interference. Figure 3.8 shows that the 6-fold symmetric pattern in k -space gets smeared out; this effect was attributed to overlap with bulk states [95]. (To be clear, this picture for bulk mixing is very different from my analysis presented in Chapter 4). The scattering patterns are enhanced along the Γ -M direction and repressed along Γ -K in k -space in both ARPES patterns and QPI patterns. The Reference [95] study also identified other quasiparticle interference pattern measurements on Bi_2Se_3 , showing that the central maximum in the Fourier transform is enhanced by the surface state mixing with the bulk, particularly in the valence band below the Dirac point [95].

Photocurrent measurements show that bulk and surface current mixing also occurs in measurements that use a spin-polarized laser to measure the spin dependent photocurrents. The photon drag effect allows spin-polarized excitations to relax through bulk valence channels instead of just inducing a spin-dependent current when the incident photon interacts with the opposite spin/momentum channel through the surface helical Dirac cone [99]. Band structure calculations show an overlap with the Dirac cone and some bulk states [100]. It is speculated that this not only interferes with quasiparticle scattering, but that it also suppresses Landau level formation in Bi_2Se_3 [101].

3.2.4 Band Bending

Subsurface charges or the application of electric fields can cause shifts in the surface electronic structure; this effect is called band bending. In both Bi_2Te_3 [64] and Bi_2Se_3 [102], band bending effects due to contamination or layer decoupling can make the surface state shift with time. Some measurements show that the Dirac cone forms and shifts over a period of

a few hours. This localized band bending is credited with shifts in the Dirac point energy between ARPES and STM measurement of up to 120 meV [69].

Band bending is responsible for quantum well formations in the top layer of the material. When the surface is exposed to different chemicals, be it incidental environmental contamination or intentional (i.e. [77]), band bending on the surface forms a two-dimensional electron gas (2DEG) over the period of a few minutes to hours depending on concentration [103, 102] and temperature [102, 101]. ARPES and transport measurements have identified a variety of contaminants that can cause the 2DEG formation.

Other contamination effects, including water [104], show a split band to appear out of the conduction band, perhaps by chemically altering the surface. High levels of carbon monoxide can confine both the conduction and valence bands due to extreme band bending [103]. ARPES measurements show the Dirac cone shifts upon exposure to molecules of N_2 and air [101]. Brahlek *et al.* showed that in transport measurements O_2 and water exposure decreases the number of two-dimensional carriers where N_2 and vacuum can nearly restore the original transport characteristics given a week. Other studies on 2DEG formation show that in extreme cases of band bending where the bending exceeds the width of the valence band, both the valence and conduction bands can become confined simultaneously [103]. Band bending on the surface is no small matter.

Figure 3.9 shows Bianchi *et al.*'s ARPES measurements of a two-dimensional electron gas coexisting with the topological surface state on Bi_2Se_3 . In Figure 3.9 there is the energy vs. momentum ARPES data of the linear topological insulating Dirac cone and a parabolic band coming down from the region of the conduction band. The sharpness of the rim is an indication of a two-dimensional state, and the three-dimensional bulk state above it appears

diffuse. To determine the source of the 2DEG, the authors confirmed this band bending was due to extrinsic defects and not a crystal reorganization using LEED. Because of the time dependence of band bending, quantum well forms over time and this data was collected after the crystal was three hours in a vacuum during which time the Dirac point shifting to lower energies. While the 2DEG can coexist with the topological state, the Dirac cone must become wider in k -space to accommodate the 2DEG and has more scattering channels into which it can decay [102]. Elsewhere in their work, Bianchi *et al.* show the inner circular 2DEG state is clearly distinguishable from the hexagon topological insulating state [102]. The hexagonal shape not only becomes more pronounced with atmospheric exposure [101] but it is related to the six-fold symmetry of the Bi_2Se_3 system and is one of the characteristics that is different from the closely related topological insulating material, Bi_2Te_3 , whose Fermi surface has a hexagram shape [105, 13]. The topological state deviates from its hexagonal state and evolves with energy through the Dirac point, where it is a bright focused spot [102] before it joins the valence band at -0.5 eV.

The mechanism of the 2DEG formation is something that is debated. Some groups advocate that a chemical modification of the surface shifts the bands [106]. Indeed, it is standard practice in transport to treat the surface with molecules to prevent Se vacancy formation [107, 77, 100]. Others advocate that the molecules intercalate into the Van der Waals gap and the expansion alone drives 2DEG formation [101]. STM measurements which are sensitive to defects on the surface or intercalated defects have never reported indications of a 2DEG formation. Theory calculations reject the chemical modification explanation and instead advocate that the chemicals intercalate between the layers with causes the Van der Waals gap to expand [108]. They show that as the 2DEG forms in the top quintuple layer, the

topological surface state is displaced to the second quintuple layer in stoichiometric Bi_2Se_3 . Because of the sensitivity of tunneling on distance in STM measurements, the implications of these calculations are that as a 2DEG forms, the Dirac cone would not be as prominent in the density of states.

Clearly, Bi_2Se_3 has a lot of rich physics. Band bending can confine the conduction band and sometimes even the valence band. Therefore, the topological surface state may coexist with a 2DEG. Quasiparticle scattering experiments show the spin split nature of the surface as scattering is suppressed in the Γ -K direction. Bulk mixing obscures the interference patterns and contributes to the muted nature of pattern development. Despite these potential non-topological effects, to the simplicity of the Dirac cone, Bi_2Se_3 is a model topological insulator.

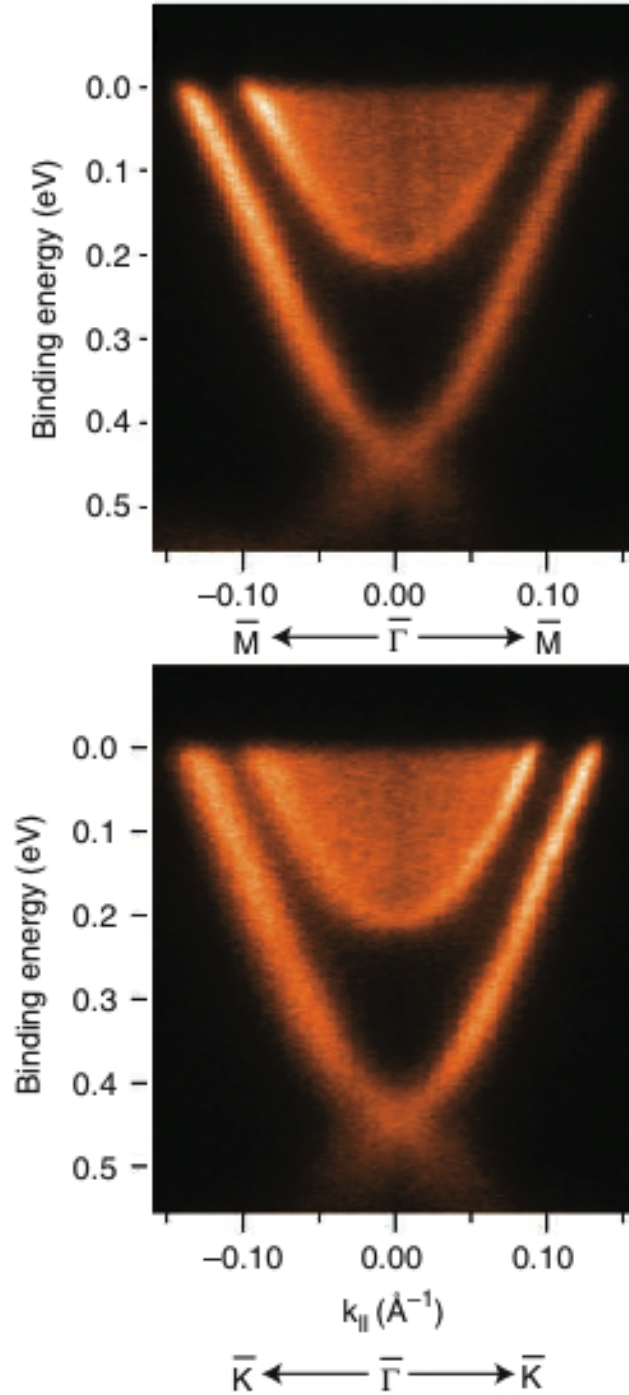


Figure 3.9: ARPES measurements on Bi_2Se_3 showing effects of the top quintuple layer separating from the crystal [102] E vs. k of the Dirac cone is shown with the 2DEG evident as the bright rim surrounding the diffuse conduction band edge. The Dirac cone is the outer x shaped feature with the Dirac point at the center of the x. Reprinted by permission from Macmillan Publishers Ltd: NATURE COMMUNICATIONS (M.Bianchi, D.Guan, S.Bao, J.Mi, B.B. Iversen, P.D.C. King, and P.Hofmann. “Coexistence of the Topological State and a Two-Dimensional Electron Gas on the Surface of Bi_2Se_3 ”. Nature Communications, 1:128, 2010.), copyright (2010)

Chapter 4

Measurements of States on the Surface of Bi_2Se_3

The topological surface state has exciting characteristics described in Chapter 3 that may be exploited for device applications. It is therefore important to know what other states on the surface are competing with the topological state as they may limit applications. In the next sections, I will show that there is a bulk contribution to the electronic structure on the surface of Bi_2Se_3 in the spectroscopy. There is also an indication that a two-dimensional electron gas contributes a feature in the density of states.

4.1 Sample Overview and Procedure

The crystals I studied were grown in the Kanatzidis group by Duck-Young Chung and Jung-Hwan Song by slowly cooling an elemental mixture from 850°C , which is a common preparation technique for bulk crystals. Samples of Bi_2Se_3 with 2%, 4% and 8% excess bismuth were prepared and the purity was established by powder x-ray diffraction. The 2%

samples showed no impurity phases, while the 4% doped sample had some Bi₂Se₃ and the 8% doped sample had BiSe impurity phases. Although they could not guarantee that all the additional bismuth was taken up by the crystal, unit cell analysis on the crystals showed that the lattice expanded a bit as more excess bismuth was added, indicating that more was taken in by the lattice.

To take measurements, a crystal of 1 mm or less in thickness and a few mm wide of Bi₂Se₃ was taken from the ingot. In general, parts of the ingot that were in the curved bottom of the growth tube did not cleave well and were avoided. A sample disk was cleaned with acetone and isopropyl alcohol to remove any dirt and oil. Once cut with a razor to size, a tiny dot of silver paint was placed in the center of a sample disk to dry for half an hour. Once dry, the mounted sample was inspected to ensure it still lay flat on the sample disk. Any edges of the sample that had been engulfed in silver paint were trimmed to ease the cleavage process. The sample was cleaved with scotch tape to expose a mirror-like surface for initial testing. It is easiest to remove any huge steps at this time. After bench top testing, the molybdenum disulfide powder was applied to the sample ramps to aid the walking process before the entire sample was loaded in a two stage process into the sample processing chamber discussed in Section 2.1. The microscope was evacuated of all impurities by pumping it to a hundred mtorr. The crystal was cleaved in the chamber, being careful to ensure a mirror-like surface without any part of the flake sticking up much higher than the surrounding area to prevent tip crashes. Finally, the sample was loaded into the microscope in its N₂ gas environment, isolated from the chamber and the microscope was pumped out overnight to a pressure of 3×10^{-6} torr.

One of the characteristic features of Bi₂Se₃ doped with excess bismuth is bright triangular

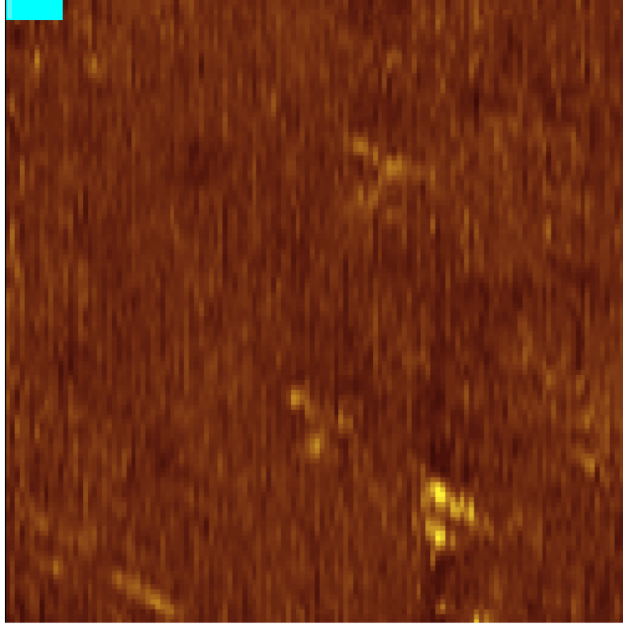
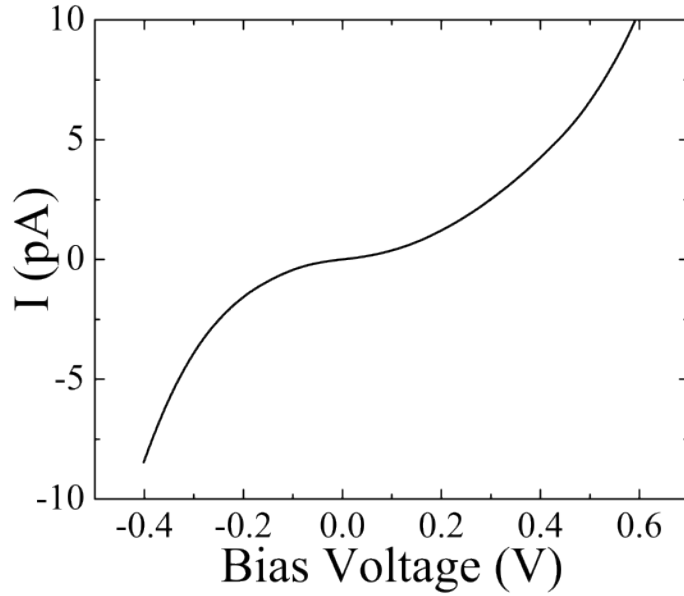


Figure 4.1: Characteristic triangles from bismuth substitutions on selenium sites in Bi_2Se_3 doped with 4% excess Bi. Image is at 4.2K with -0.8 V bias and 0.50 nA set current. The scale bar is 3 nm.

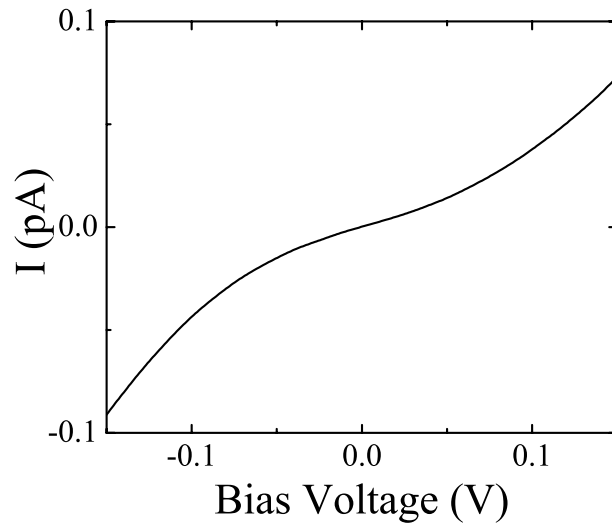
enhancements discussed in Section 3.2.2. Figure 4.1 shows triangles I measured on the surface of Bi_2Se_3 with 4% excess bismuth. This finding confirms that the samples exhibit the qualities that are expected, and that the sample processing chamber does result in a sufficiently clean surface.

4.2 Spectroscopy Measurements on Bi_2Se_3

I applied STM at 4.2K to perform spectroscopy on Bi_2Se_3 doped with 4% excess Bi. All spectroscopy measurements were consistently made on sample locations far from defects to ensure the spectrum was of the pure Bi_2Se_3 state. In a material with a band gap, the slope of I-V curves goes to zero in the gap. Figure 4.2 (a) shows the I-V curve. We see that the slope described in Section 2.2.1, dI/dV , is never zero at any bias voltage. By focusing on the low voltage region (± 0.15 V) in Figure 4.2 (b), it is even more clear that the slope is

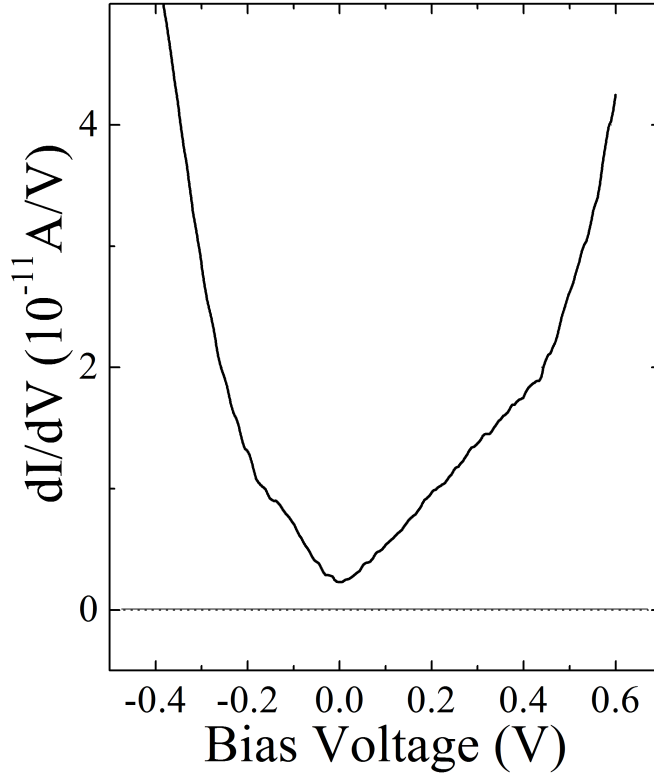


(a)

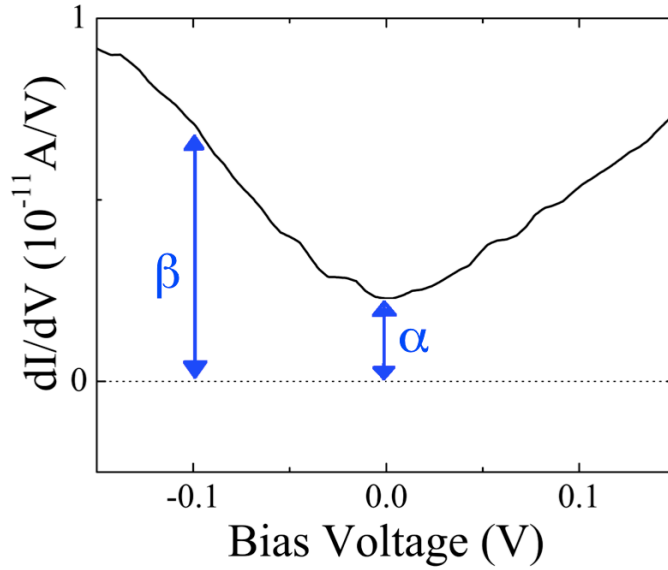


(b)

Figure 4.2: (a) The calculated I-V curve on Bi_2Se_3 doped with 4% excess Bi at 4.2K. (b) The same I-V curve expanded in the region of the Dirac cone. The slope does not go to zero at zero voltage, indicating there are states in the gap. Due to an analog to digital issue in the electronics, the current was calculated from the dI/dV curve in Figure 4.3 (a). The dI/dV curve was measured directly from using the lock-in amplifier as described in Section 2.2.1 and therefore did not experience the same analog to digital issue.



(a)



(b)

Figure 4.3: (a) Density of states on Bi_2Se_3 doped with 4% excess Bi at 4.2K where the linear region of the Dirac cone is between ± 0.15 V. The Fermi level is in the center of the gap. There are additional states that lift up the bottom of the Dirac cone. The curve is an average of 150 curves taken successively to reduce the signal to noise ratio. (b) The density of states only in the region of the Dirac cone showing parameters α and β , described in the text.

nonzero. The nonzero slope indicates that there are states in the gap. If the basic picture of Bi_2Se_3 is completely described by only a single Dirac cone that resides inside an insulating band gap, there should be a point where there are truly no states. At the point the slope of the I-V curve, dI/dV would have to be zero. By examining only the I-V curve, it is clear that other physics is in play.

Stoichiometric Bi_2Se_3 is n-type, meaning the current is predominantly carried by electrons. The Fermi level tends to be pinned to the conduction band edge due to Se vacancies in the crystal [109]. We suspected that the excess Bi would tend to shift the Fermi energy, E_F . In Figure 4.3, we see from the horizontal axis that the excess Bi almost perfectly compensates and the Fermi level is at zero volts. While this is not essential to the analysis, it is still a nice feature of the data that several research groups have strived to achieve. The clear V-shaped Dirac cone is in the region of ± 0.15 V. With respect to the vertical axis, we see that the Dirac point is lifted up from zero. This is just another visual depiction of how dI/dV never goes to zero; there is always an offset of the Dirac cone.

To determine that the offset of the Dirac cone, or “background”, was intrinsic to the system and not an artifact, I compared spectroscopy in different spots on the sample and different doping levels of Bi. In Bi_2Se_3 spectroscopy, I compared the ratio of the height of the offset, α , to the height of the Dirac cone at -0.1 V, β , as drawn in Figure 4.3(b). Because the scale on density of states measurements is arbitrary, it is necessary to compare the ratio of feature heights when comparing different spectroscopy curves. In this case, the choice of β is arbitrary; it could have been chosen to be anywhere in the Dirac cone so long as the comparison is at the same cone heights between spots on the sample. For the data shown in Figure 4.3, $\beta/\alpha = 2.87$. I repeated the same measurement at different locations within the

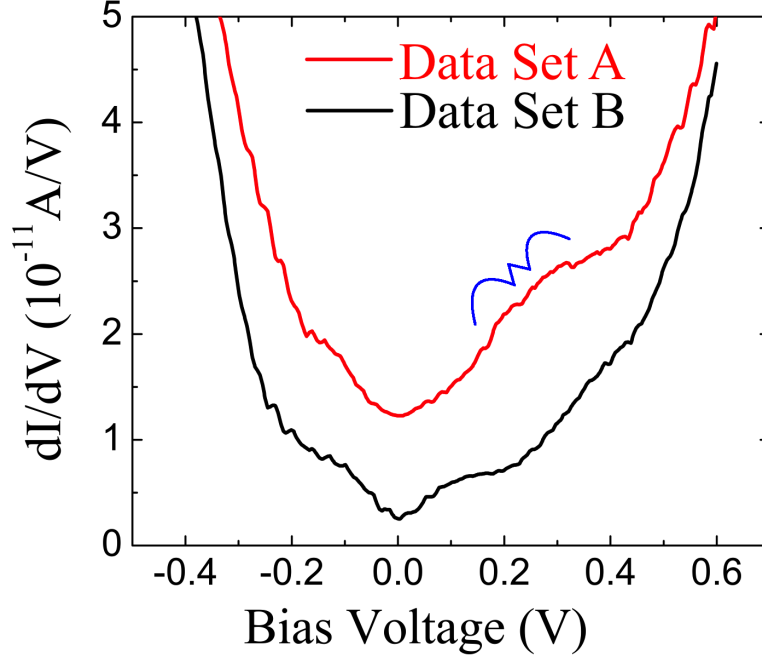


Figure 4.4: Density of States where each of the curves is an average of 50 measurements. Data set A was taken before Data set B without manually moving the tip. Data set A has been offset by one tick mark to ease visual comparison. A blue bracket has been drawn to highlight the enhancement. We speculate the tip drifted during the measurement, causing the feature at +0.2 V to change.

sample at 4.2K and the ratio β/α is consistent within 15%, which is the error expected due to scatter in the data. Given the consistency between these measurements, I concluded the offset is an intrinsic feature of Bi_2Se_3 .

While the Dirac cone and the background states do not depend on the measurement location within the sample, the spectroscopy features above +0.2 V is location dependent. Figure 4.4 shows the density of states on Bi_2Se_3 far from defects. Above +0.2 V the curves show progressively enhanced density of states. Each of the curves plotted is an average of fifty curves. There were another 50 curves between Data Set A and Data Set B that show an intermediate step between the enhancement and depression at +0.2 V that has been removed for clarity. The apparent dip at +0.2 V arises where the Dirac cone is no longer lifted up by the shoulder states. Calculations in the following discussion showed only that the shoulder

extended past the Dirac point, but how far beyond the Fermi level the Dirac cone extended was unable to be determined.

I believe that any differences in each of the three successive curves arise from thermal drift during the measurement. In other words, the spot on the sample the measurement began is not the same point the measurement ends. Similar enhancements and depressions have been observed at other locations on this sample. However, this data set is unique in that I see an evolution between them.

4.3 Analysis of the Bi_2Se_3 Spectrum

Density functional theory (DFT) is a computational technique to find the electronic structure of periodic quantum mechanical systems. It is a way of approximately solving the Hamiltonian using only the density of electrons in space. To analyze my data, Dr. Mal-soon Lee working with Professor S.D. Mahanti performed DFT calculations. The calculations were performed using the projector augmented wave (PAW) methods as implemented in the commercially available VASP package. The Perdew-Burke-Ernzerhof (PBE) generalized gradient corrected exchange-correlation functional were used in the calculation. To fully solve the band structure, spin orbit interactions were included. Theoretical details of the calculation can be found in Reference [110].

Figure 3.6 shows the bulk calculation in gray and a 6 quintuple layer (QL) slab calculation in blue with the Fermi energy at the Dirac point. While a single Dirac cone transverses the gap, the bulk has a shoulder state in the Γ -M direction similar to calculations by Xia *et al.*[100], Yazyev *et al.*[111], and Kim *et al.*[95]. The same state appears in the calculations performed by Dr. Mal-soon Lee shown in Figure 4.5 (a) and Figure 4.7 marked by the red

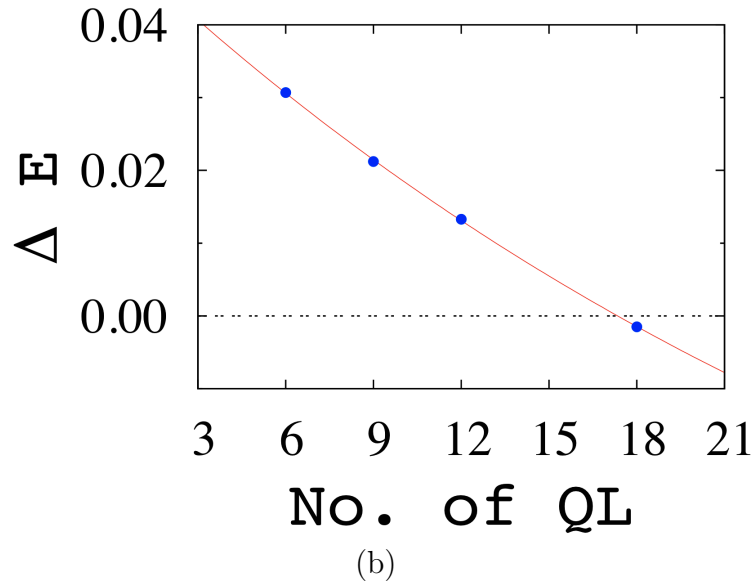
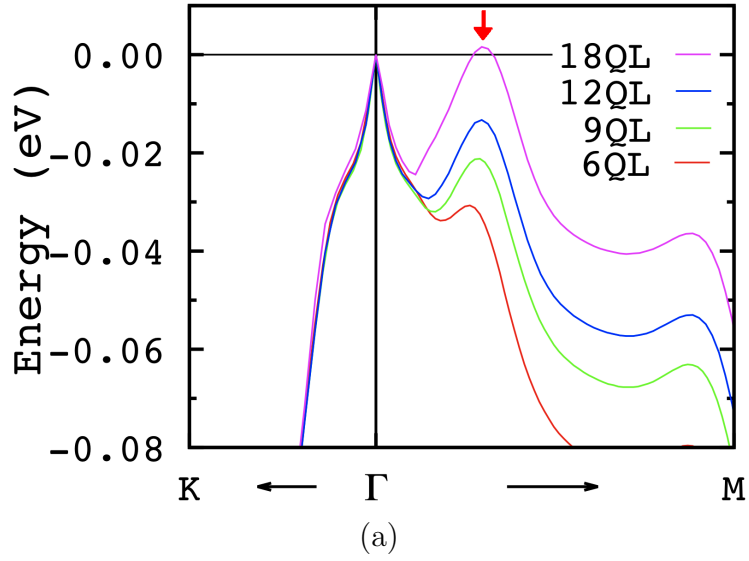


Figure 4.5: (a) Valence band calculation with increasing numbers of QL. The shoulder state in the Γ -M direction increases in energy and eventually crosses the Dirac point. (b) Graph of the change in energy with QL. Eventually the height of the shoulder will reach a bulk value as the number of QL increases. Figure courtesy of Dr. Mal-soon Lee

arrows.

Prior to this work, nobody had studied systematically how increasing the number of quintuple layers in a slab calculation increases the shoulder's energy. Slab calculations of Bi_2Se_3 seen in Figure 4.5 (a) from 6-18 QL show how the energy of the shoulder increases with the number of QL which indicates that they probably originate in the bulk. However, the Dirac cone states do not change as the number of quintuple layers increases which demonstrates that the topological surface state is well established by 6 QL. To match the energy scales, the Dirac points of each slab were aligned with the Fermi level at zero voltage. The Dirac cone itself is due to the presence of the surface and is not present in any bulk calculations.

We see from Figure 4.5 (a) that the shoulder in the $\Gamma - M$ direction of k-space is getting higher in energy as the number of QL increases. Figure 4.5 (b) shows the trend of the change in energy, ΔE , which is the difference between the top of the Dirac cone and the maximal shoulder energy. ΔE becomes more negative with increasing QL. This is consistent with the energy of the Dirac cone becoming comparable with the height of the shoulder. By an 18 QL slab, the energy height of the shoulder exceeds the Fermi level and ΔE becomes negative. Extrapolating from the graph, the energy will eventually level out at some sort of constant "bulk" value if the number of quintuple layers is increased further. Extra states at the Fermi level would indeed add to and lift the Dirac cone. Hence, these shoulder states are then excellent candidates for explaining the background in STS measurements as an interplay of surface and bulk states.

Figure 4.5 (a) shows that shoulder states exist at the right energy to mix with the topologic surface state in the region of the Dirac cone. To fully explain my measurements,

these electronic states need to reside in the top layer of the material. Because of the tunneling current's exponential dependence on the tunneling gap distance, described in Section 2.2, STS measurements are most sensitive to the topmost atom, Se1, and to a lesser extent the Bi1 atom immediately below it. In other words, these shoulder states need to have spectral weight on the surface for STM to measure them. Only if the shoulder state resides on the surface can it explain why dI/dV never goes to zero at the Dirac point in Figure 4.3.

Figure 4.6, also calculated by Dr. Mal-soon Lee, contrasts the partial density of states (PDOS) from the Dirac cone (Region I) with the shoulder states (Region II). These calculations are for a 6QL slab because anything thicker would be computationally prohibitive. As expected, the contributions to the partial density of states from the Dirac cone resides primarily in the Se1 and Bi1 on the topmost quintuple layer within the gap. In the middle QL, there are no contributions from Region I in the gap but Region II dominates. There is a big contribution to the density of states in the middle QL Se1 from the shoulder states and a lesser contribution from the middle QL Bi1. The fact that the shoulder states dominate in the middle, bulk-like, region of the slab agrees with the bulk calculations found in Xia *et al.*[100] and Kim *et al.*[95]. To determine if the shoulder states are present on the surface, one needs to look for a peak in the top layer Se1 at approximately -0.3 V, the energy of the shoulder state for a 6QL slab. In Figure 4.5 (a), there is indeed a big peak in Se1 on the topmost layer and it is even evident in the Top QL Bi1. While the shoulder states may originate in the bulk-like part of the slab, they are still present in the top quintuple layer that is probed in STM measurements.

To highlight these results pictorially, Dr. Lee calculated the partial charge density contribution from just the shoulder states for a 6 QL slab and from the bulk calculations in Figure

4.7. The shoulder states in from bulk calculations are selenium-like, meaning that they have a higher spectral weight near Se atoms, depicted with red halos throughout the quintuple layers. While most of the charge from shoulder states in the slab calculation is centered around the Se atoms in the middle of the slab, we see that there is some finite charge density near the top of the top quintuple layer which would be accessible to tunneling. (Figure 4.6 is better at showing the relative intensities of the Dirac cone and the shoulder states on the surface).

In summary, the calculations show how there are bulk states that reside on the surface that have the potential to contribute to STM measurements. STM is not sensitive to the momentum of the electrons, so any states available at the Fermi level will contribute to tunneling. Hence, the shoulder states sum with the Dirac cone states, giving rise to the offset, α in Figure 4.5 (a), seen in my density of states measurement. In other words, we believe there is an interplay between the bulk and topological surface state in Bi_2Se_3 that STM probes.

4.4 Analysis of Two Dimensional Electron Gas on the Surface

Figure 4.4 shows how over the course of a long measurement, there is a feature above +0.2 V that begins as an enhancement and then becomes a depression in the density of states. In Section 4.2, I speculated that the tip may have drifted during the course of the measurement so that the area of the sample the tip was probing at the beginning was not the same as the one it was probing at the end. Due to reasons about to be expanded upon, the tip may have

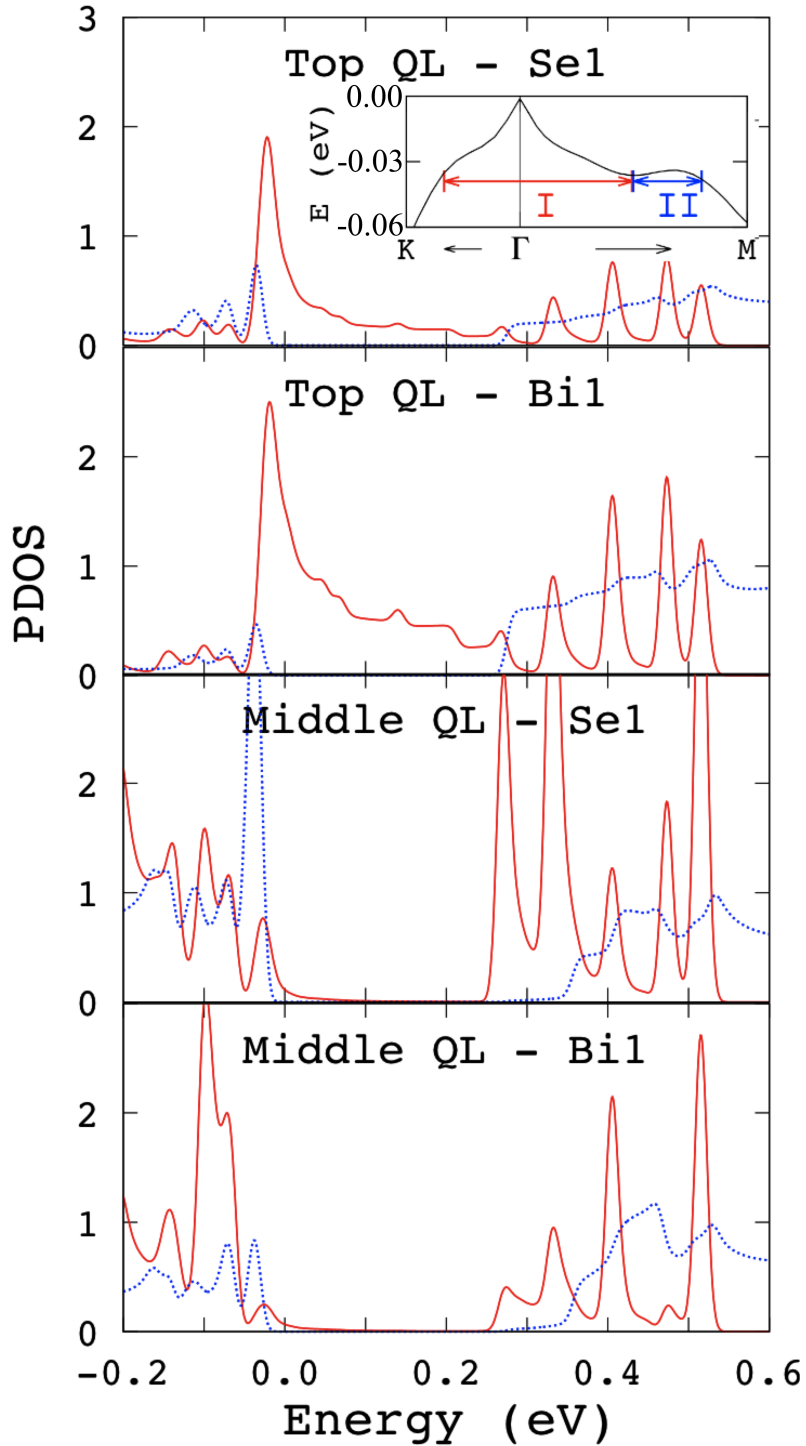


Figure 4.6: Partial density of states (PDOS) calculations performed by Dr. Mal-soon Lee on a 6 QL slab. The inset shows the parts of k-space that contribute to Region I and Region II. The contribution to PDOS from the Dirac cone is depicted in red. It resides primarily in the top layers within the bulk band gap. The contribution from the shoulder states (blue) have the largest contribution in the middle QL, however it has a finite contribution in the top QL Se and Bi atoms. In this case, the peak is just to the left of zero energy (the Fermi level) for this rather thin slab.

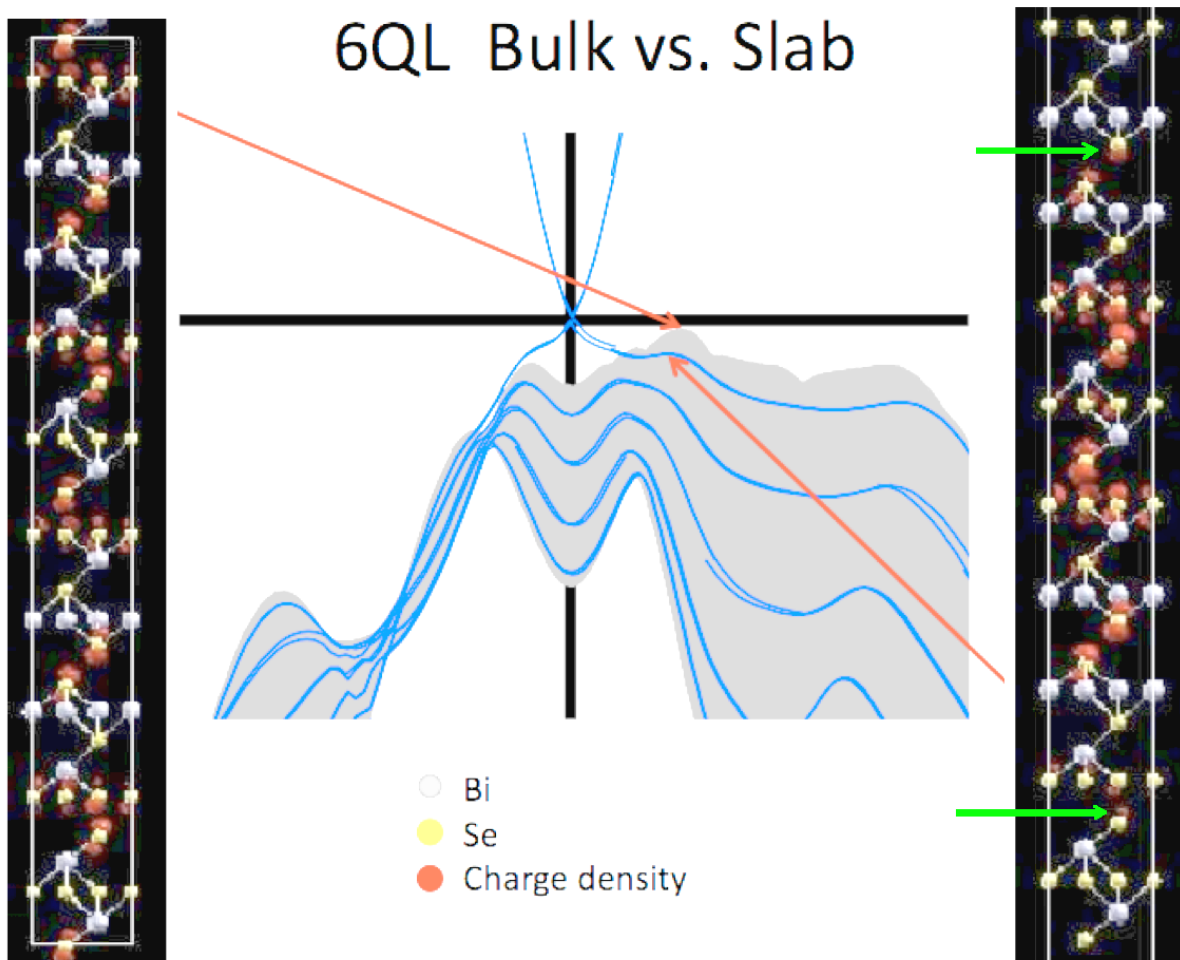


Figure 4.7: Comparison of bulk and slab calculations. This contrasts the partial charge density from bulk band structure calculations (gray in the band structure) on the left side of the image with those from the slab calculations (blue in the band structure calculations). The Se are yellow, the Bi atoms are blue-gray and the the intensity of the red halos depicts how strong the charge density is at that region. No halo means there is no significant charge density. The bulk calculations show the partial charge density is mostly distributed on the Se atoms in all layers equally. The partial charge density on the slab calculation on the right is primarily located on Se atoms as well, but has the highest density in the middle layers (the bulk-like area of the slab). However, there is some charge density on Se atoms in the outermost quintuple layers shown by the green arrows. Figure courtesy of Dr. Mal-soon Lee

drifted from an area of the sample where the top QL was less connected to where it was more connected. The readily cleavable surface on Bi_2Se_3 leaves the possibility for the top layer to be less bound in some areas. The Van der Waals gap between the top two layers may widen during the cleaving process or later when a strong field is applied to the crystal. Impurities may also contribute to layer separation. Clearly, if one QL were completely separated from the crystal, the extended electron wavefunction may resemble a two-dimensional electron system.

Few groups have studied the formation of a 2DEG on the surface of topological insulators. The explanations from ARPES studies focussed on the effects of impurities. Some studies have shown that separating the top layer from the subsurface layer increases causes the conduction band edge to move into the gap and localizes the 2DEG in the top layer [102, 103, 112]. Common impurities that are believed to cause layer separation are oxygen[106], CO [103], water [104], and other adsorbates [112, 102, 81], many of which are common vacuum contaminants. Theoretical calculations support the possibility that the layer is more loosely bound in some areas by predicting a two-dimensional electron gas sets up on the top quintuple layer.

To explore these ideas more carefully, Dr. Lee performed similar DFT calculations to those in Section 4.3. Figure 4.8 shows her results that support the idea that a 2DEG may have set up on the surface of the material. We see that an increase in the physical separation gap between the top two quintuple layers of thirty to fifty percent causes the lowest band of the conduction band to extend into the gap. The shape of this band is parabolic like a 2DEG. For the data shown in Figure 4.4, as the STM measurement progresses I believe the tip is drifting from a more separated region to a less separated region removing the enhancement

in the density of states by the end of the measurement. The enhancement to the LDOS cannot be from other sources like Se vacancies because not only was there no evidence in the topography, but also the enhancement appears at a higher energy than Se vacancies [91]. Moreover, there is no other electronic evidence of an impurity of the surface of any kind even though we were probing with a blunt tip. As further spectroscopic evidence, the Dirac cone is not as sharp of a V shape between +/-0.1V in Data Set A as Data Set B.

Menshcikova *et al.* [108] calculated the partial charge density of the Dirac cone with an increasing layer separation. Their partial charge density calculations showed that the 2DEG pushes the Dirac cone into the second quintuple layer, which would reduce the Dirac cone's contribution to my STM measurement. Interestingly, the background states are not effected by 2DEG formation.

In summary, there is some evidence that a 2DEG may have locally formed on the surface due to layer separation. Dr. Lee's calculations show that when the Van der Waals gap between the topmost quintuple layers expands, a 2DEG comes down from the conduction band and resides at +0.2 eV above the Fermi level. This voltage is same energy that the enhancement appears in my measurement in Figure 4.4 leading to the possibility that there is a 2DEG in the top quintuple layer of some of my Bi₂Se₃ sample.

4.5 Bi₂Se₃

As a comparison, I looked at an undoped crystal of Bi₂Se₃ previously used by Dr. Sergei Urazhdin. Figure 4.9 (a) and (b) show the current-voltage and density of states curves. In this case, the curves are averages of only five curves, and the higher noise level reflects it. The Dirac cone is not very pronounced, but the background that lifts up the center of the

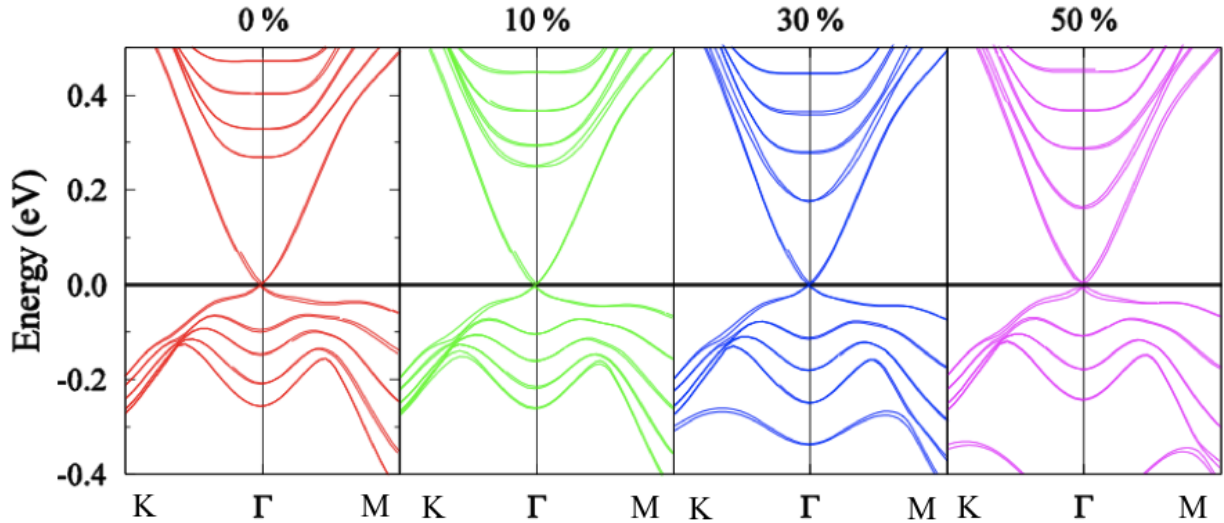


Figure 4.8: Band structure calculations of a 6 QL slab of Bi_2Se_3 for which the top QL is separated from the others. The percentages refer to how much additional separation is given to the top QL. We see as the top layer detaches, the bottom of the conduction band drops into the gap and forms a two-dimensional electron gas on the surface. Figure courtesy of Dr. Mal-soon Lee.

gap is still clearly there. The whole curve is shifted to more negative voltages than the 4% doping in Section 4.2 making it more n-type than that sample. This shift is consistent with the previous conclusion that Bi tends to restore the Fermi level to the center of the gap. Its n-type nature is probably from Se vacancies [14]. The enhancement described at +0.2 V in Section 4.4 associated with the 2DEG has also shifted with all the bands. Consistent with previous conclusions, a 2DEG formation obscures the Dirac cone. Undoped Bi_2Se_3 shows many of the same spectral hallmarks of the pristine Bi_2Se_3 I probed in Sections 4.3 and 4.4. Excess bismuth doping only serves to shift the band structure all at once and not relative to each other as was described in reference [101]. Doping only fills in the selenium vacancies and shifts the bands, but does not alter the topological state. Moreover, these measurements on the undoped sample take place at 77K instead of 4.2K in Section 4.2 demonstrating that temperature effects do not impact any of the previous conclusions. Figure 4.9 (c) shows an

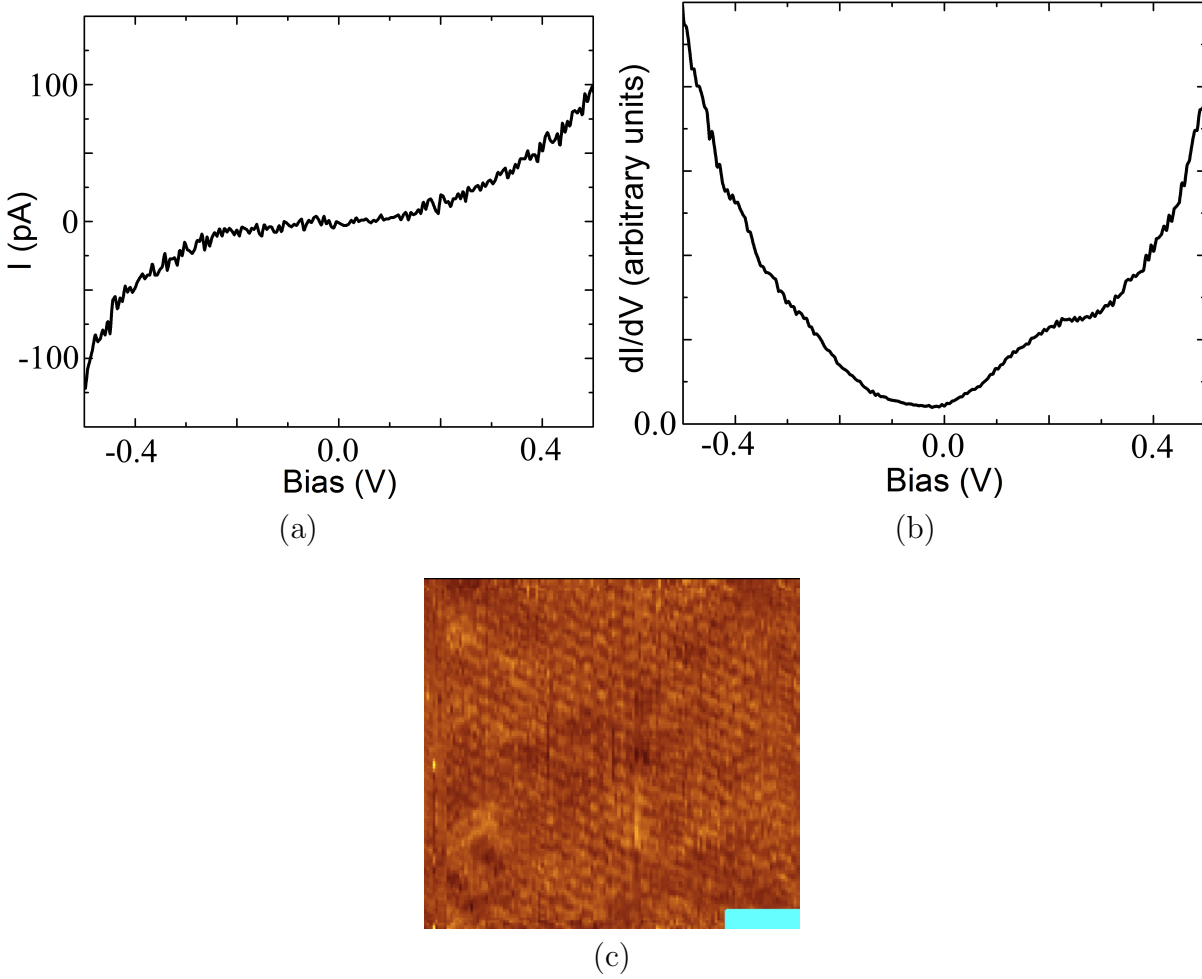


Figure 4.9: STM data at 77K. Both the (a) I-V curve and the (b) density of states are an average of 5 curves. (c) Atoms on the surface of Bi_2Se_3 at -0.20 V and 0.1 nA. Scale bar is 1.6 nm.

atomic resolution image of the surface where there is evidence of the dark smudginess I have come to associate with all of these samples, which will be expanded upon in Chapter 5. In short, neither temperature effects or doping alter characteristic features of Bi_2Se_3 samples. There is an interplay of bulk states with the topological surface state between samples which is not altered by doping and a 2DEG can potentially set up on the surface of the material.

Chapter 5

Other Measurements of Bi_2Se_3

This chapter gives an overview of different samples I examined, but does not directly impact the analysis of my primary results in Chapter 4. This chapter should be seen as supplemental information as it is focussed on empirical observations. It covers additional information about my primary sample of Bi_2Se_3 doped with 4% excess bismuth, as well as samples with 2% and 8%. Details about the sample quality can be found in Section 4.1.

5.1 $\text{Bi}_{2.02}\text{Se}_{2.98}$

All my earliest studies on topological insulators were on $\text{Bi}_{2.02}\text{Se}_{2.98}$. Most of the measurements took place before the processing chamber was installed so there was more surface contamination. The final cleave took place in the laboratory environment before the sample was placed in the microscope, pumped down to a pressure of 3×10^{-6} torr overnight and cooled to a temperature of 77K. The biggest challenge for these samples was finding a spot that was clear enough to get any kind of meaningful image. Many scans had debris that often attached to the tip, necessitating tip recovery techniques fairly often. Nevertheless, I

was able to scan many topographic features that appeared in every doping level of Bi_2Se_3 studied.

For instance, Figure 5.1 (a) shows the top selenium layer of $\text{Bi}_{2.02}\text{Se}_{2.98}$. There is no electronic impurity signature in this scan range. The dark spots in Figure 5.1 (b) seem to have a slight triangular shape and originate from a selenium vacancy [92, 91]. Dark triangular features are often imaged in Bi_2Se_3 and can appear right alongside bright triangles originating from interlayer Bi substitutions [10].

Impurities should have an electronic signature on a sample. If they are truly part of the sample and not some debris on the surface, the apparent topography of impurities will change with the voltage. Figure 5.2 shows both surface contamination and electronic defect states. These images were taken in succession with only the bias voltage changing between them. Rows of atoms are also visible across the images. The upper right hand corner of all the images has a bright blob that is independent of voltage. In many of the scans, there is streakiness that extends down the image from that corner. This smearing is common in scanning probe measurements when there is something unstable that is not securely attached to the sample or tip. This observation leads to the conclusion that it originates with the surface contamination and not interlayer Bi, which creates triangular topographic features that are independent of voltage [10]. The tip and the sample are interacting that causes artifacts in the topography image. Elsewhere in the image in the scans at -0.50 V in Figure 5.2 (a) and (c) there are bright blobs in the upper left corner and close to the middle of the image. Unlike the surface debris, these two enhancements disappear at -0.55 V in Figure 5.2 (b) and at -0.4 V in Figure 5.2 (d). The reason the defect states do not appear as triangular is unknown but could be an artifact of the tip, but the defects are behaving like

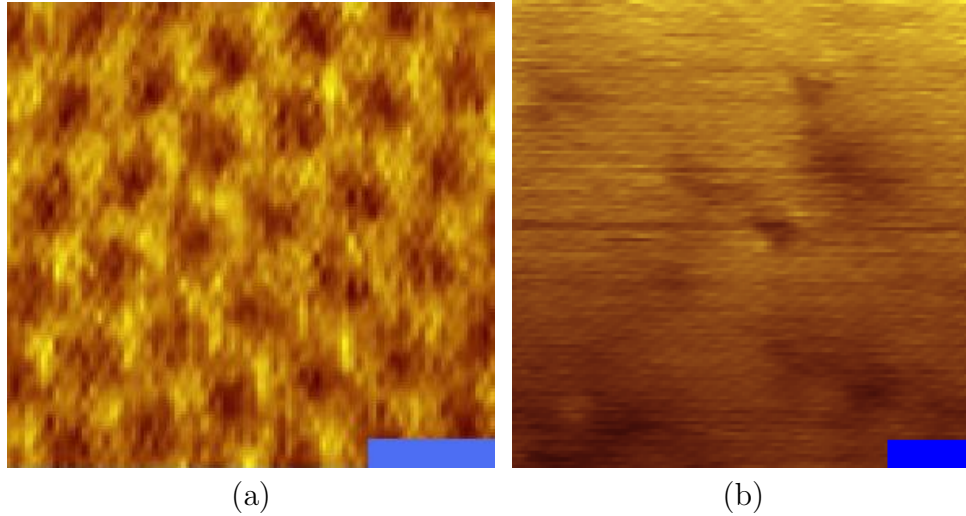


Figure 5.1: Data taken at 77K without the chamber. (a) Atoms on the surface of $\text{Bi}_{2.02}\text{Se}_{2.98}$ at a set current of 0.11 nA and -0.5 V. Scale bar is 3 Å. (b) Dark pits seen all over the $\text{Bi}_{2.02}\text{Se}_{2.98}$ potentially caused by surface contamination. Scale bar is 17 Å.

Bi substitutions from reference [14].

5.2 $\text{Bi}_{2.04}\text{Se}_{2.96}$

Here I give additional measurements on what turned out to be my primary sample, Bi_2Se_3 doped with 4% excess Bi. Even with a processing chamber, there tended to be a little bit of debris on the surface of $\text{Bi}_{2.04}\text{Se}_{2.96}$. Many times images were so streaky that there are no meaningful features on the surface. Defect states can be hard to discern when the surface is shifting. The tip was compromised and dragging the tip to refurbish it was not very helpful. Field emission tended to work best, but was only reliable at high voltages. After a few recoveries at 150 V, the tip became extremely blunt. Topography images were then featureless but the spectroscopy was excellent. Consequently, some of the best spectroscopy curves, like that in Figure 4.3 had a completely featureless topography image taken in tandem. Nevertheless, many topography features were evident on the surface of $\text{Bi}_{2.04}\text{Se}_{2.96}$.

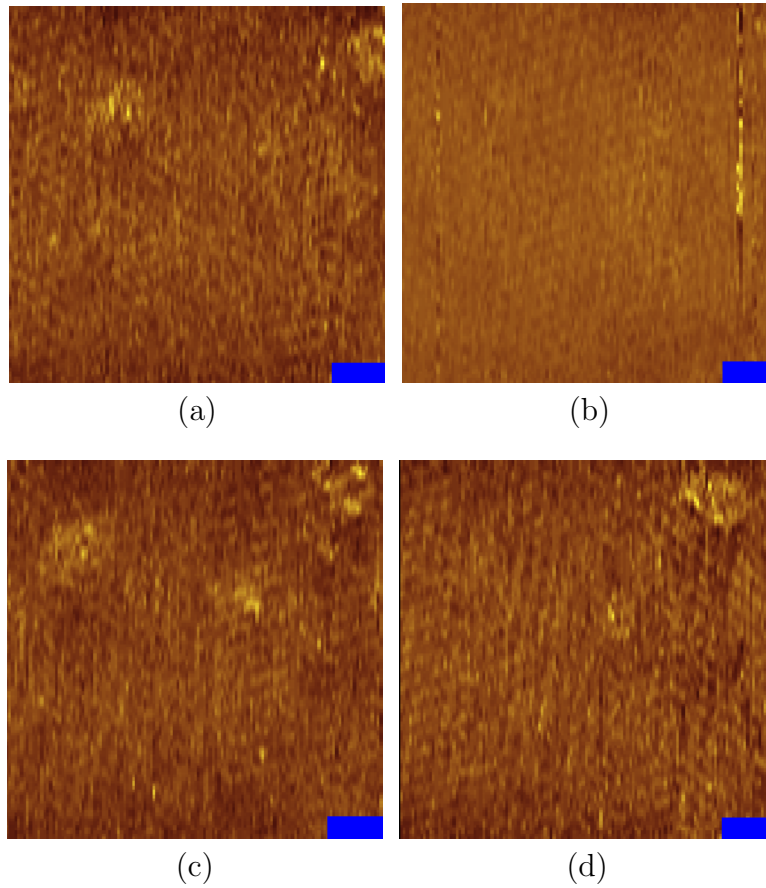


Figure 5.2: Defects on the surface of $\text{Bi}_{2.02}\text{Se}_{2.98}$ at 0.5 nA set tunneling current and 77K. Scale bars are 7 Å. Each image is taken in sequence at a bias voltage of (a) -0.5 V (b) -0.55 V (c) -0.50 V and (d) -0.4 V. The bright spot in the upper right corner of every image is surface contamination. Impurities in the crystal are visible in the upper left in (a) and (c).

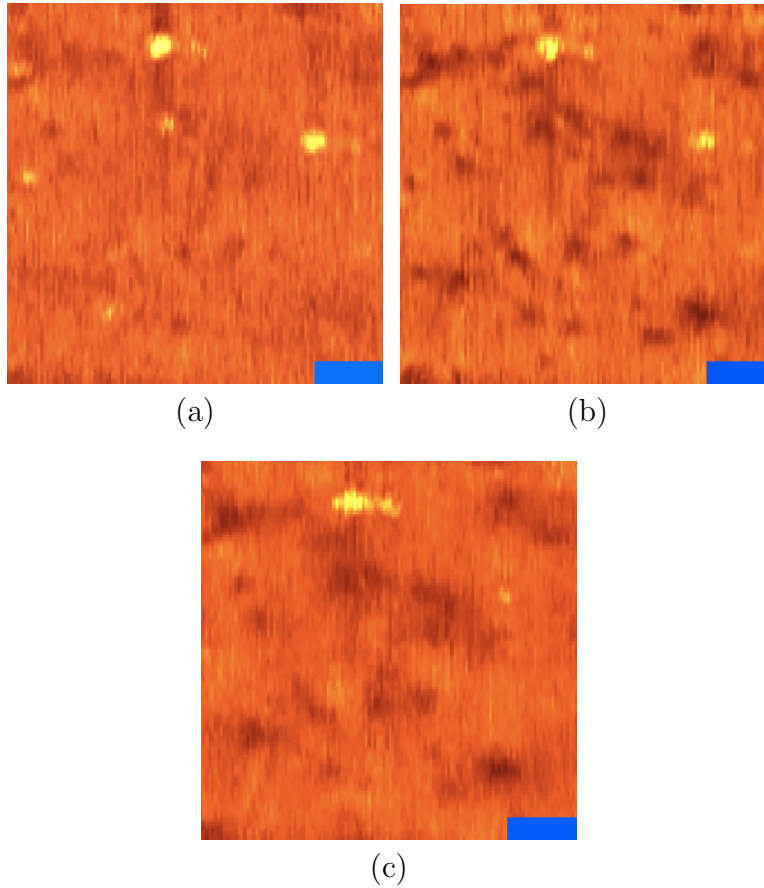


Figure 5.3: Defects on the surface of $\text{Bi}_{2.04}\text{Se}_{2.96}$ at 0.5 nA set tunneling current and liquid helium temperature. Each image is taken in sequence at a bias voltage of (a) -0.80 V, 36 pA (b) -0.49 V, 73 pA and (c) -0.29 V, 52 pA. Dark impurity spots become more diffuse with changing voltage. Bright specs of surface contamination also visible in every image. Scale bars are 3.3nm.

Because it seemed to routinely cleave with fewer step edges than other doping levels, this sample was the most extensively studied material.

Dark blobs appear all over the sample. They definitely have some electronic origin because they are sensitive to voltage. As Figure 5.3 shows, the dark blotches become darker, less diffuse and better resolved as the voltage changes. There is also debris in the upper right corner of this sequence. Some of the bright spots are electronic features because they are active at the same bias as the triangular defects in Figure 5.4 (a). Because the bright irregular blobs are much larger than the triangular defects, the large features, while voltage

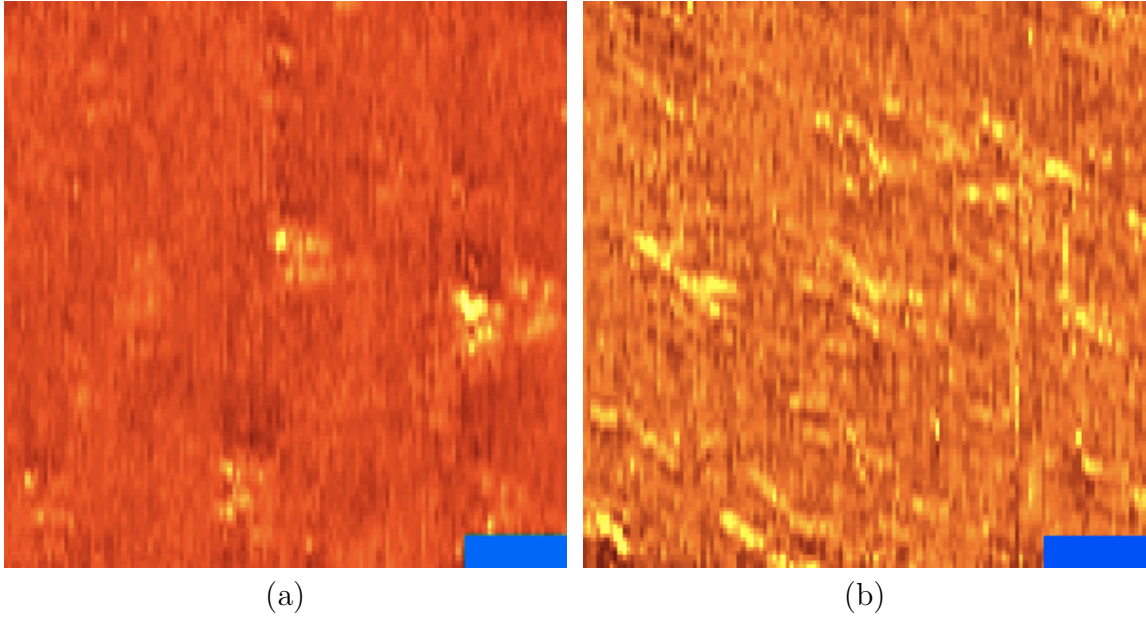


Figure 5.4: Data taken at 4.2K. Scale bars are 3.3 nm.(a) Bright triangular defects on the surface of $\text{Bi}_{2.04}\text{Se}_{2.96}$ at a set current of 60 pA and bias voltage of -0.80 V. (b) Clusters of triangular defects arranging in strings at 60 pA and -0.79 V.

independent, are likely from some surface debris and not the interlayer Bi described in reference [10].

The characteristic bright voltage dependent triangular defects [14] appear in scans of $\text{Bi}_{2.04}\text{Se}_{2.96}$. Figure 5.4 (a) shows relatively isolated defects. Each triangle is about 7nm across, similar to Urazhdin *et al.*. Sometimes the defects cluster in a way that makes them appear as lines in the images instead of just isolated triangles. These lines in Figure 5.4 (b) are parallel because triangles all point the same direction due to their perturbation on the lattice electronic structure[10].

The same features of triangular defects and pits persist at liquid nitrogen temperatures. Figure 5.5 (a) shows several triangular defects all over the image. While there are clusters of defects, they do not seem to arrange themselves into strings of defects in the same way as Figure 5.4 (b). Unfortunately, the lack of concentrated regions of defects limited my ability

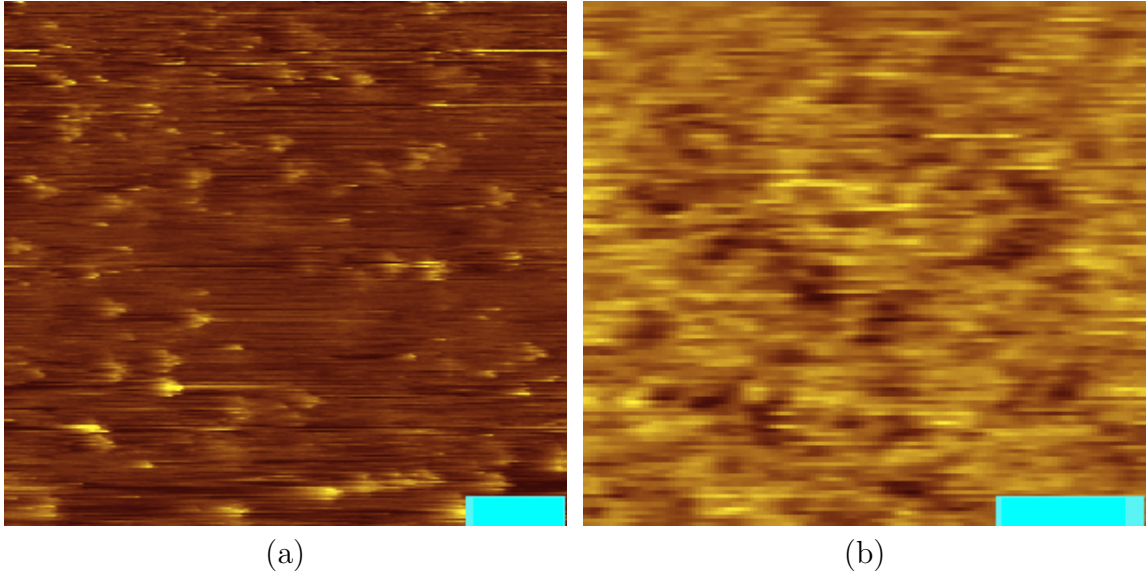


Figure 5.5: Data taken at 77K. (a) Bright triangular defects on the surface of $\text{Bi}_{2.04}\text{Se}_{2.96}$ at a set current of 24 pA and bias voltage of -0.48 V. Scale bar is 17 nm. (b) Pits on the surface at 118 pA and -0.38 V. The scale bar is 67 nm.

to image these defects with Kelvin probe. The dark spots also persist at 77K. They are quite large, often tens of nanometers across. While these are electronically different from the surrounding area, they do not locally change the capacitance signal. If they do represent any difference in the electric field from the sample, they are electronically screened over a distance of approximately 20-30nm. This length scale is comparable to the screening length calculated for Bi_2Te_3 of 26 nm in reference [80].

5.3 $\text{Bi}_{2.08}\text{Se}_{2.92}$

I spent the least amount of time on the eight percent doped sample. Most of the time I spent studying these samples also took place before the cleaving chamber was installed. Of all the samples I worked with, this one was the most difficult to get a good cleave where large areas of the sample were step edge free. This sample would flake up quite a bit more

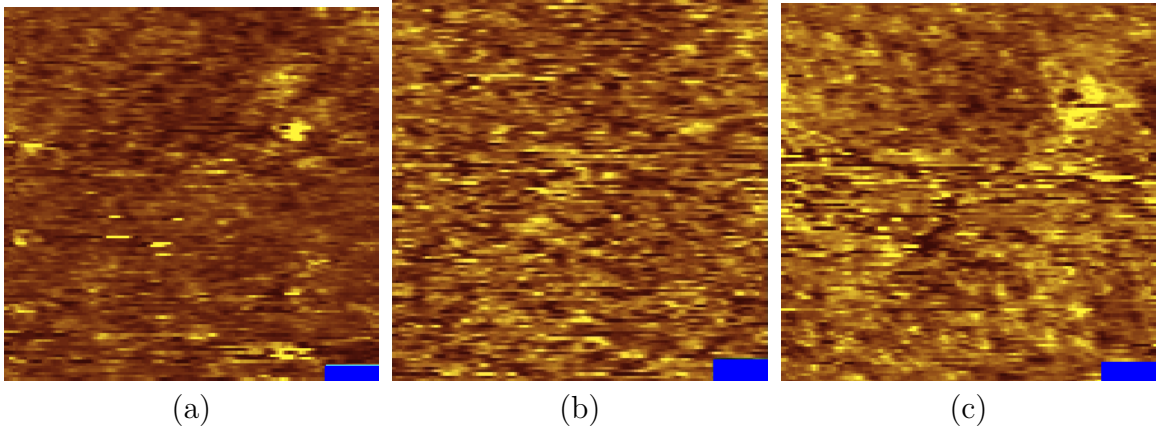


Figure 5.6: Data at 77K, scale bar is 3.3 \AA and set current 1.02 nA. (a) -0.6 V (b) -0.3 V and (c) -0.6 V. There is both surface contamination, atomic resolution and a voltage-dependent defect in the upper right corner.

than the others. Perhaps due to the high doping level, that $\text{Bi}_{2.08}\text{Se}_{2.92}$ leaves a lot more surface residue from the last cleave than any of the other crystals. It is fairly common to see a few tiny grains on the mirror like surface after cleaving any crystal with scotch tape. I have always interpreted these bits as coming from the fracture that occurs around the step edges as the scotch tape is peeled away. In 8% doping, the fine dust is more wide spread (so are the step edges) and is adhered to the surface well enough that it cannot be dislodged with N_2 gas. A data run on the sample after the chamber was installed was short in part because of all the particles that still remained on the sample that contaminated the tip. As you can see from Figure 5.6, there is quite a bit of surface contamination leading to a streaky image. Nevertheless, there is still a visible electronic lattice in each of these images. In the upper right corner of Figure 5.6 (a) and (c), there is not only a tiny piece of surface contamination, but a larger bright spot that disappears in (b). While 8% excess bismuth does show features characteristic of Bi_2Se_3 , it is not the best sample to probe the Bi_2Se_3 state.

In summary, all of the samples of doped Bi_2Se_3 show similar features. Dark spots, most likely from Se vacancies, appear on all of the samples, but so do voltage-dependent bright

spots from bismuth on a selenium site substitutions. These electronic structure signatures are distinguishable from the debris that covers the surface.

Chapter 6

Other Scanning Probe Methods

6.1 Capacitance and Kelvin Probe Circuit

For scanning capacitance measurements, the apex of the tip is essentially a nanometer-size capacitor plate and the nanometer scale piece of the sample below represents the other capacitor plate. Just like a large capacitor, if charge enters the sample, image charge of the opposite sign appears on the tip. Another way to say this is that electric field emanating from the sample induces image charge on the tip.

Largely the same circuit is used in both Kelvin probe and capacitance measurements. It consists of a tip and two high electron mobility transistors (HEMT) on a gallium arsenide chip. Gold pads sputtered on the GaAs allow the circuit connections to be made with a wire bonder. Low temperature conducting epoxy adheres the HEMTs and tip to the chips. I assemble all the chips in the lab.

The two HEMTs in Figure 6.1 serve very different purposes. The bias HEMT serves to tune the measurement HEMT to its most sensitive region for the measurement. In addition,

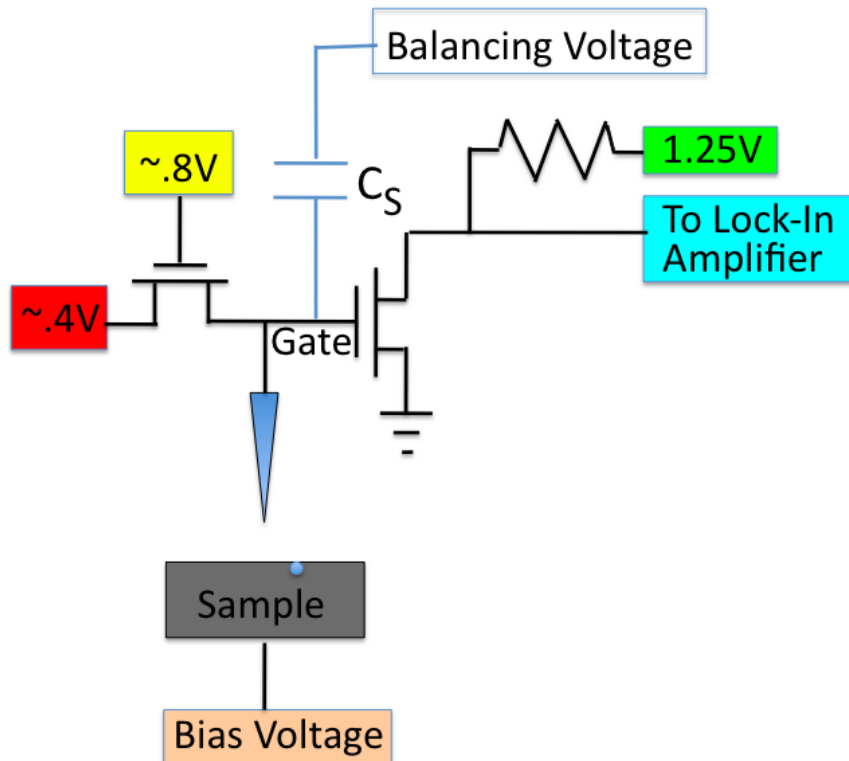


Figure 6.1: HEMT circuit diagram: The standard capacitor (line drawn in blue) is only included for capacitance measurements. Oscillations are applied either to the bias voltage for capacitance measurements or by oscillating the tip above the sample in Kelvin probe. The lock-in amplifier detects the change in capacitance on the tip due to these oscillations.

the bias HEMT has a large impedance on its source-drain channel that ensures all the charge that oscillates on the tip goes to the gate of the measurement HEMT. Any charge oscillating on the tip then changes the effective resistance of the source-drain channel to be measured by the lock-in amplifier. The charge sensitivity of the circuit is $.16e/\sqrt{Hz}$ at 77 K [113].

The measurements the circuit is able to make are limited by other sources of capacitance and noise in the system. Warming of the system is minimized by keeping the power dissipated by the circuit low, in the microwatt range. As seen in Figure 6.2, this requirement puts the device in the linear region of the source-drain characteristics.

Part of measuring anything with this HEMT circuit is a background capacitance. The largest source of capacitance is the capacitive coupling between the gate and source-drain channel for the measurement HEMT. This capacitance, C_{in} , is around 0.3pF and impacts the voltage signal that reaches the lock-in amplifier. There is also a self-capacitance from the circuit's size, which is minimized by keeping the tip-HEMT distance as small as possible.

6.1.1 High Electron Mobility Transistor

A high electron mobility transistor (HEMT) is a field effect transistor mediated by a two-dimensional electron gas. The surface of the transistor has gold pads that provide ohmic contact to the sub-surface material for integration into a circuit. A layer of electron-rich $Al_xGa_{1-x}As$ donates some of its electrons to the undoped GaAs layer below, creating a highly mobile two-dimensional electron layer. The conducting properties of the electron layer are mediated by voltage applied to the gate. Therefore, any voltage applied to the gate changes the effective resistance of the source-drain channel.

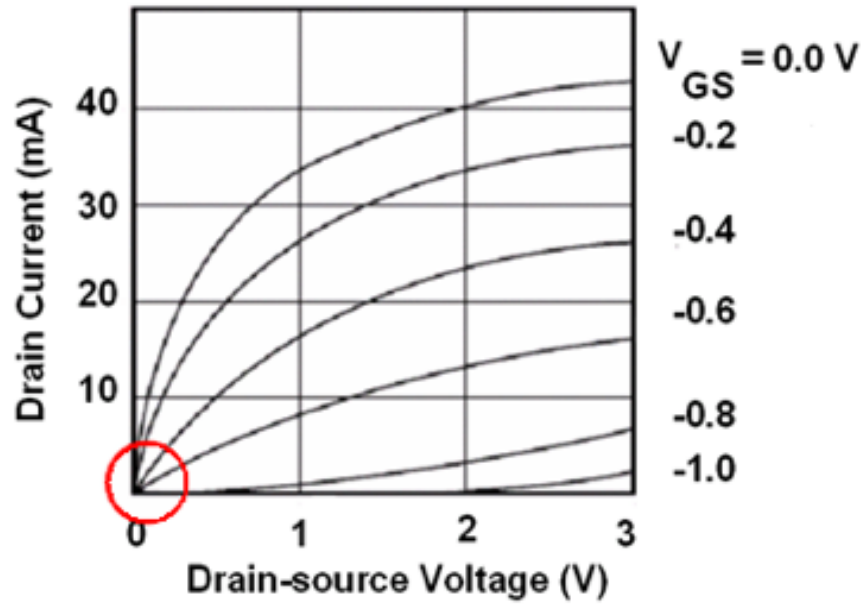


Figure 6.2: The plot shows the drain current vs. the drain-source voltage of a HEMT at different gate voltages. Varying the gate voltage changes the effective resistance of the source-drain channel. The HEMT is operated in the linear region circled in red to minimize power output [43].

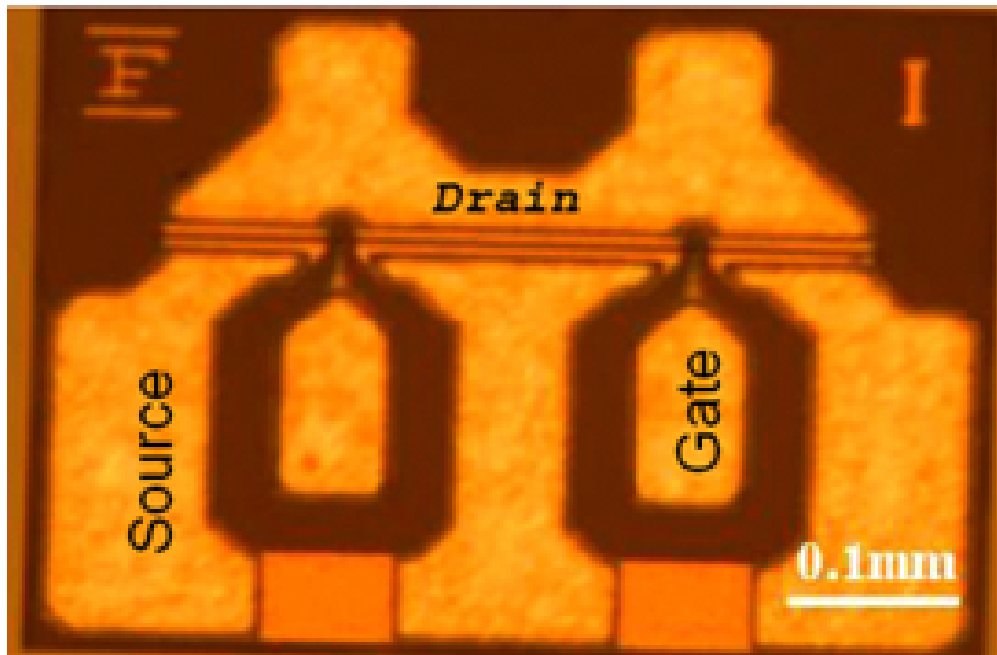


Figure 6.3: A photograph of the Fujitsu model FHX35X HEMT. The size of the device is $\sim 500 \mu\text{m}$ across [43].

6.2 Capacitance Measurement

The capacitance measurement uses the HEMT circuit to detect charges entering the sample, which induces charge on the tip. The capacitance measured depends on the geometric capacitance, C_{geo} , which is due to physical features of the tip and sample and on the compressibility or thermodynamic density of states of the sample, $\frac{dn}{d\mu}$, relating to the electronic states through the equation:

$$\frac{A}{C_{meas}} = \frac{A}{C_{geo}} + \frac{1}{e^2 \frac{dn}{d\mu}} \quad (6.1)$$

The tip-sample distance is fixed about 1nm above the sample. The electric field from the sample lands on the tip as it is scanned over the surface. The capacitance measurement can be used to detect defects within the surface provided they are charge sinks [34] .

6.2.1 Physics

The HEMT circuit measures charge oscillating on the tip, q , in response to charge entering the sample due to a voltage oscillation, V_{AC} applied to the sample. The charge oscillations are sensed by the tip as an image charge oscillating in phase with the voltage oscillation, V_{AC} – finally causing an oscillating voltage on the gate of the measurement HEMT. Not all of the electric field lines emanating from the sample land on the apex of the tip; many land on other areas of the macroscopic tip wire. These contribute to a background capacitance which is constant (independent of the tip’s apex position). To subtract away this background signal, a signal oscillating at the same frequency but 180° out of phase as the V_{AC} is applied to a standard capacitor, depicted as C_S in Figure 6.1.

The gate and source-drain channel of the measurement HEMT have an effective capacitance C_{in} which is approximately 0.3 pF which limits the sensitivity of the circuit. The self-capacitance can be minimized by making the tip-circuit distance as small as possible, so that its contribution is approximately 0.1 pF.

The total capacitance, including the background signal is usually $C_{tip-sample} = 20$ fF (2×10^{-15} F. Voltage on the gate in Figure 6.1 is related to the voltage at the lock-in amplifier, $V_{lock-in}$, by a gain factor, G . Therefore, $V_{lock-in}/G$ is related to V_{AC} and the capacitive impedance by the voltage divider equation:

$$\frac{V_{lock-in}}{G} = V_{AC} \frac{Z_2}{Z_2 + Z_1} \quad (6.2)$$

where $Z_1 = (i\omega C_{tip-sample})^{-1}$ and $Z_2 = (i\omega C_{in})^{-1}$. G depends on electronics external to this HEMT circuit and is approximately unity. The frequency of oscillation is ω . Equation 6.2 can be further simplified by realizing that $C_{in} \gg C_{tip-sample}$ and will only become increasingly greater if you account for the circuit's self-capacitance which only adds to C_{in} . Therefore, $V_{lock-in} = \frac{C_{tip-sample}}{C_{in}} V_{AC}$ with respect to the tip's charge, and the signal is $q = V_{lock-in} C_{in} = C_{tip-sample} V_{AC}$. To maximize the signal on the lock-in amplifier, $C_{tip-sample}$ should be as large as possible. Maintaining the smallest gap between the tip and sample achieves this end because capacitance varies inversely with the distance between the electrodes. The transistor was chosen to minimize C_{in} . Increasing V_{AC} increases the signal, but any increase of V_{AC} will reduce the energy resolution of the measurement. The typical frequency of the sample voltage excitation is 20 kHz. The typical amplitude of oscillation is 0.1 V peak to peak. With regard to the noise level, at 0.3 K the circuit achieves an amazingly low charge noise of $0.01e/\sqrt{Hz}$, where e is the electron charge

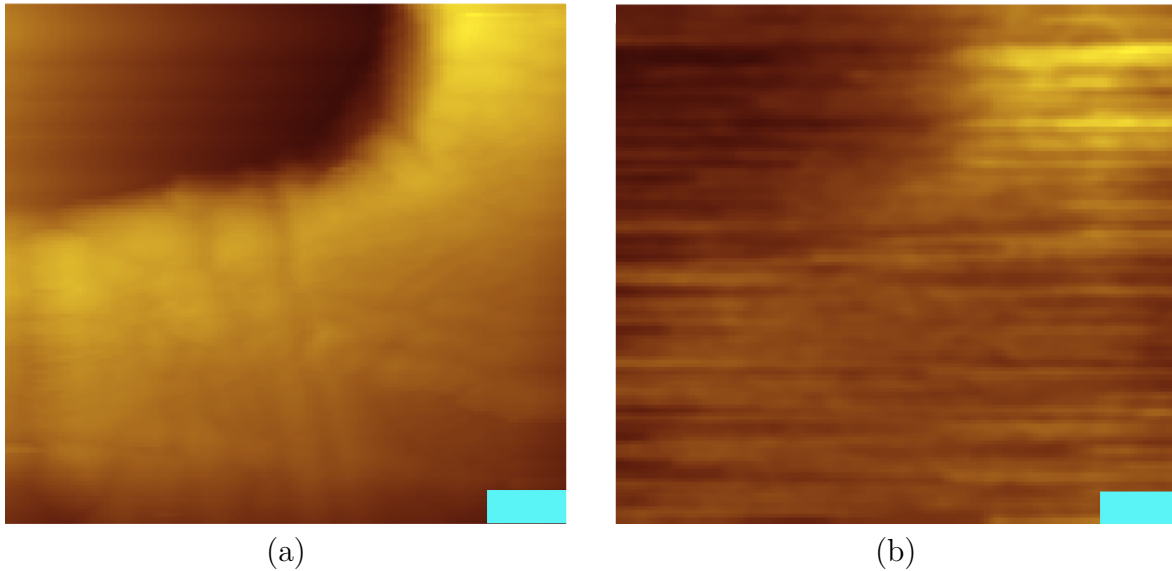


Figure 6.4: (a) Topography image of the corner of a pit. (b) Capacitance image in the same region as (a). Both are imaged at 77K, the scale bars are 330nm long and were taken with an etched tip.

6.2.2 Demonstration

In addition to charging signals, the capacitance measurement is sensitive to changes in topography. The Pt pits sample serves as a good proof-of-principle sample. In Figure 6.4, the edge of a pit is clearly visible in the upper left corner of the scan range. This same edge appears in the capacitance. In this case, the contrast is due to a geometric capacitance.

6.3 Kelvin Probe Measurement

The Kelvin probe method employs an oscillating tip connected to the charge sensing circuit. It measures electric field patterns emanating from the sample and is sensitive to any field that is not screened away. Local measurements can measure the work function of the metal [114] and can also be applied to image surfaces [37].

6.3.1 Physics

In Kelvin probe measurements, the voltage oscillations the lock-in amplifier detects originate from physical oscillations of the tip. As the tip extends, more electric field lines from the sample terminate on the tip than when it retracts. The resulting signal on the HEMT circuit is proportional to the change in capacitance (or charge) with distance. However, there is no electric field between the tip and the sample at a particular tip voltage, called the nulling voltage or contact potential (V_{null}). If $V_{tip} = V_{null}$, the voltage on the lock-in is not sensitive to distance. The charge the lock in senses is not only sensitive to the oscillation amplitude of the scanning tube, Δz , but also its height above the sample, z_0 . Moreover, the signal charge on the lock-in consists of the actual charge signal, Δq , in addition to an offset signal, q_0 , that arises from stray AC electric field landing on the HEMT gate.

$$\begin{aligned}
 q_0 + \Delta q &= \frac{A\epsilon_0}{z_0 + \Delta z} (V_{tip} + V_{sample} - V_{null}) \\
 &= \frac{A\epsilon_0}{z_0} \frac{1}{z_0 + \frac{\Delta z}{z_0}} (V_{tip} + V_{sample} - V_{null}) \\
 &\approx \frac{A\epsilon_0}{z_0} \left(1 - \frac{\Delta z}{z_0}\right) (V_{tip} + V_{sample} - V_{null})
 \end{aligned} \tag{6.3}$$

where A is the area of the measurement, V_{tip} and V_{sample} are the voltage of the tip and sample respectively and ϵ_0 is the permittivity of free space. Only the oscillating part of this equation will be sensed by the lock-in amplifier, so Equation 6.3 simplifies to:

$$q_{lock-in} = \frac{A\epsilon_0}{z_0^2} \Delta z (V_{null} - V_{tip} - V_{sample}). \tag{6.4}$$

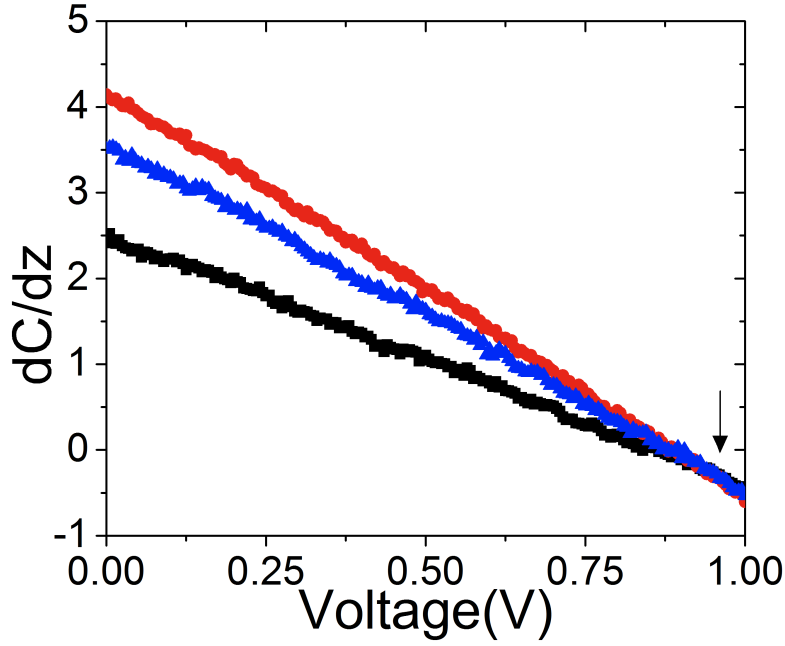


Figure 6.5: Nulling voltage measurement on Bi_2Se_3 . The arrow shows the voltage where all the curves intersect (0.9 V). Because there is a -0.43 V applied to the tip relative to the sample, the nulling voltage here is $0.9 - (-0.43) = 1.23$ V.

(For simplicity, Equation 6.4 assumes $q_0 = 0$.) By this relation, the signal is insensitive to the tip distance whenever $V_{sample} = V_{null} - V_{tip}$. In practice, the tip is at a voltage set by the source of the bias HEMT to keep the measurement HEMT in its sensitive region and only the voltage applied to the sample can be varied. To find the nulling voltage the Kelvin probe signal versus voltage is measured at a mean tip distance above the sample, z_0 . This measurement is then repeated at two or more other different z_0 above the sample. All these are plotted on the same graph. Because only the nulling voltage is insensitive to distance, the voltage at which the curves intersect is V_{null} . The nulling voltage in Figure 6.5 is actually 1.2 V when one accounts for the offset from a voltage applied to the tip as well as the sample.

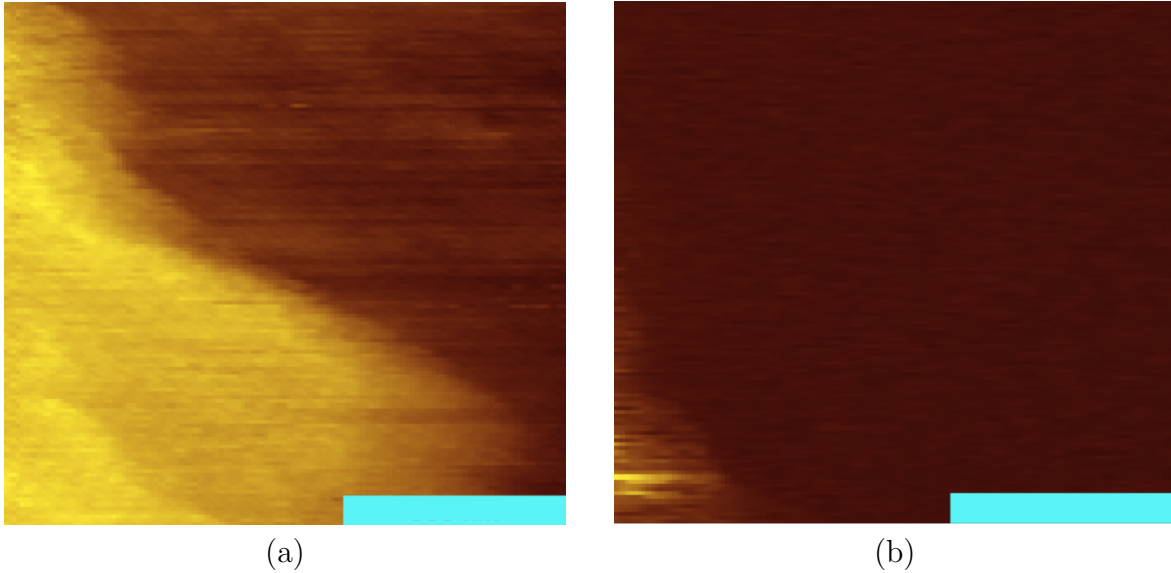


Figure 6.6: Bi_2Se_3 topography (a) and Kelvin probe (b). In this case, the Kelvin probe image is nearly featureless because the signal is dominated by the high plateau in the lower left. The topography image shows two step edges, where each step is 1 nm high. The Kelvin probe scan must be within half a nanometer of the sample – even one nanometer beyond does not contribute. The scale bar is 170 nm on both images. The amplitude of oscillation is 1 nm.

6.3.2 Demonstration

The tip is held at a constant height above the sample for scanning Kelvin probe images and the oscillation is applied on top of it. Due to the limitations of an RC charging time constant from my cables, the largest frequency I can perform measurements at is 1 kHz, which limits the sensitivity of the HEMT. The only way to increase the signal is to increase the amplitude of the oscillation. However, it is extremely important to limit the amplitude of the oscillation so that the tip does not repeatedly tap the sample anywhere in the area of the scan. All Kelvin probe measurements were performed at 77K.

The relevance of the distance to the sample in Kelvin probe mode of operation is most clearly illustrated in Figure 6.6. In this case, the tip is only measuring changes due to a geometric capacitance. The topography image in Figure 6.6 (a) shows a double step on the

layered material, Bi_2Se_3 , where each step is one nanometer tall. While the tip is closest to the sample, a mere 0.5 nm away, the step shows up in Kelvin probe scans. There is not even a hint of a step just one and a half nanometers below the tip. Hence we see that Kelvin probe imaging has limitations for surfaces that have height variation of more than a few nanometers.

The distance to the sample is not the only relevant dimension in Kelvin probe measurements. Unlike STM, where the atom protruding farther than the rest does the imaging, the radius of curvature of the tip limits Kelvin probe resolution. In the topography image in Figure 6.7, a trench crosses the Bi_2Se_3 sample that is 1nm deep and 4nm wide and is denoted by an arrow. Other dark blotches in the image are likely due to defects. A few hours later, a Kelvin probe image of the same location shows the electric field emanating from the edges of the trench as a bright line. However, the trench's field is 13nm across, three times as large! This discrepancy is actually a good indication that the tip used was large compared to the size of the trench and demonstrates that the tip's radius matters more for capacitance type measurements [115]. To be sure, Figure 6.7 does illustrate that Kelvin probe imaging is useful to map out the patterns of electric field; such as the higher field emanating from the edges of the trench.

6.4 Tips

For capacitance and Kelvin probe measurements, the shape of the tip determines the resolution of an experiment. A blunt tip will not be able to resolve fine features, so it is important to have a tip whose radius of curvature is smaller than any feature of interest on a sample. The ideal tip is one that is cylindrically symmetric with as small of a radius of curvature as

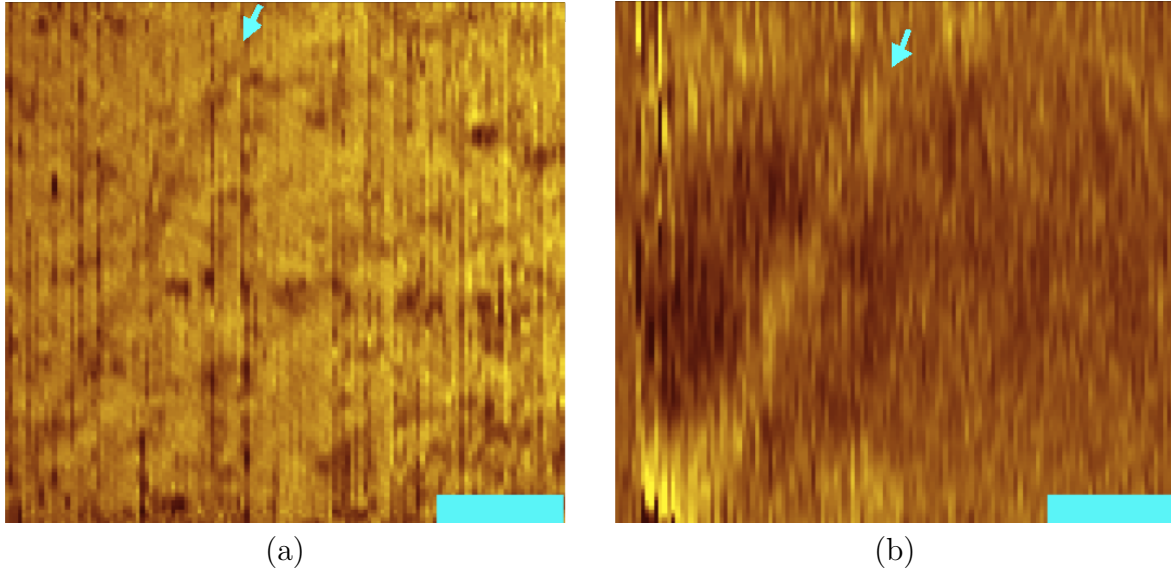


Figure 6.7: Bi₂Se₃ topography (a) and Kelvin probe (b), Here we see a scan showing a trench indicated by an arrow. The trench is three times as wide in Kelvin probe as topography. The Kelvin probe scan had a 1 nm amplitude of oscillation on the tip at the nulling voltage and was 1 nm above the sample. The scale bars are both 33 nm. The tip may have drifted over the four hours between the topography scan and the Kelvin probe scan

possible. In my experiments, it was desirable to resolve electronic variations on the sample of approximately 10nm, so I paid a great deal of attention to the tips. I examined a couple hundred tips with the Scanning Electron Microscope (SEM not to be confused with the STM I did in my thesis measurements) to determine their suitability for the capacitance or Kelvin probe experiment. For previous discussion about tips see Chapter 2.3.4.

6.4.0.1 Etched

Prior members of the group had repeated success with etched tips. Etched tips are made of Pt(.8)Ir(.2) wire that is electrochemically etched to a fine point and then rinsed with detergent to get rid of residual chemicals. We purchased etched tips from Agilent. After reviewing thirteen etched tips with a scanning electron microscope, I determined that it was unlikely that I would find one that had a 20 nm radius of curvature. Most tip's radius of

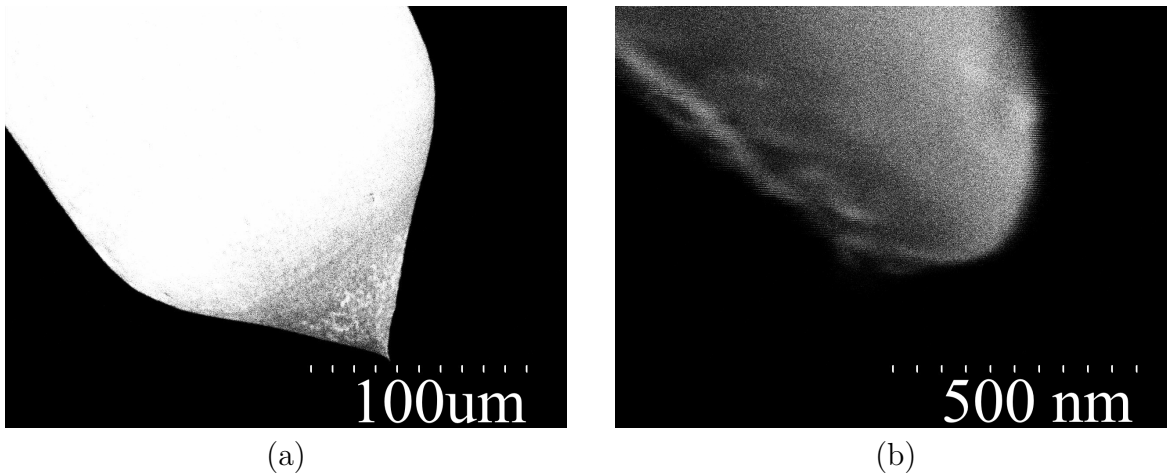


Figure 6.8: SEM image of an etched tip made by Agilent with a tip radius of curvature of 100 nm. Both (a) and (b) are the same tip with different scales.

curvature was well over 100 nm as seen in Figure 6.8. Many tips visually had white debris even around the apex, however, surprisingly, they consistently produced stable tunneling images.

6.4.0.2 Cut

Cut tips produced the most variation of all the types of tips I examined. While all were cut from the same Pt(.8)Ir(.2) wire, some were extremely blunt and others had a large aspect ratio. Many tips could be determined unsuitable by visual inspection. Over one hundred cut tips were examined with SEM and about 40% had a radius of curvature of 25 nm or more. An additional 20% were used for STM measurements, where resolution and tip shape are less directly related. In STM, for example, a step edge will be better resolved with a sharp tip, whereas a blunt tip might smear the edge out. Figure 6.9 shows tips with a 20 nm or less radius of curvature.

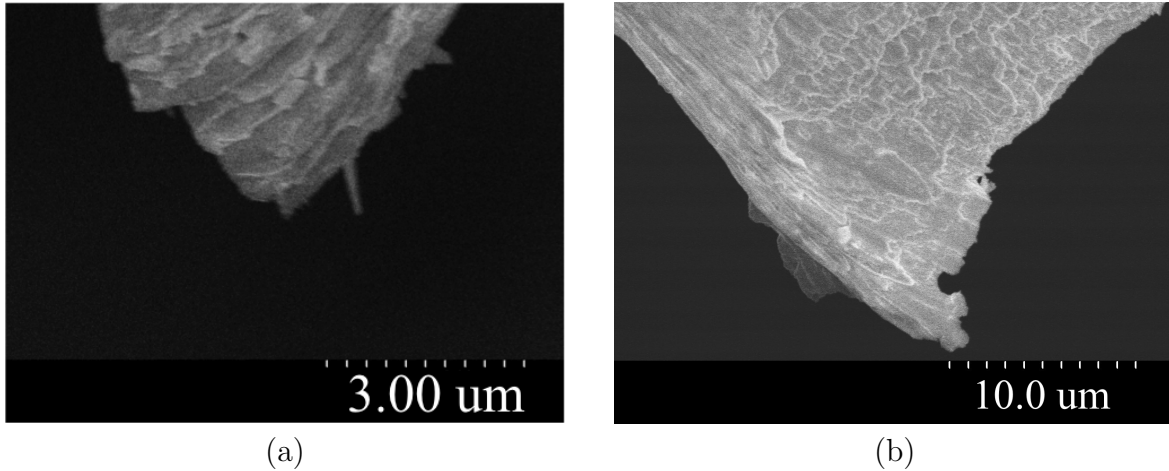
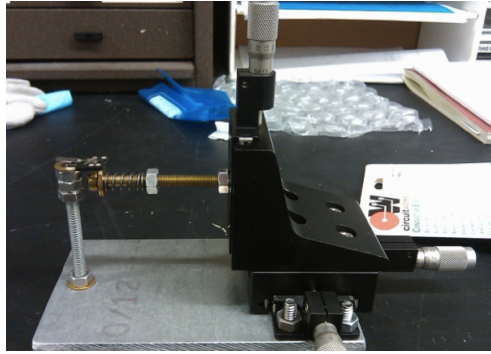


Figure 6.9: Cut tips with a radius of curvature of 10 nm and 25 nm.

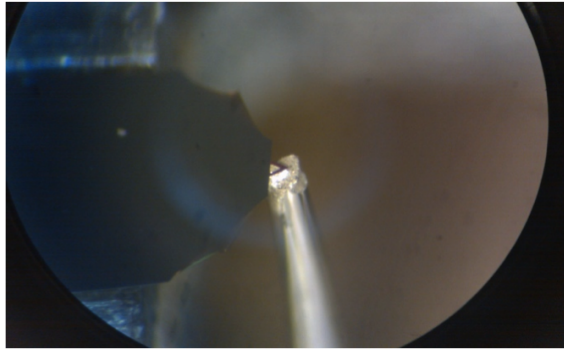
6.4.0.3 Ultrasharp

With tip size being extremely important for capacitance or Kelvin probe measurements, I wanted a way to make tips with a radius of curvature 20 nm or less reliably. It needed to be something that was inexpensive compared to tips already on the market. Furthermore, the tips needed to be able to be fabricated with apparatus already existing within our laboratory or for common use in the Keck Microfabrication facility (which excluded fabricating our own nanotube tips). Because undergraduates were going to ultimately develop, optimize and execute the ultrasharp tip fabrication, no multi-step technique requiring harsh chemicals was appropriate.

Ultrasharp tips were therefore fabricated from ultrasharp silicon nitride AFM tips attached to a PtIr wire with conducting epoxy, a technique developed by Mark Regalla and perfected by both Andrew Belcher and Eric Goodwin. To make the tips conducting, a 2nm layer of gold was evaporated onto the apex of the tip. Each tip was examined with SEM to determine the radius of curvature and ensure that the apex of the repurposed AFM tip was higher than the epoxy. We did not want to tunnel through epoxy because it would



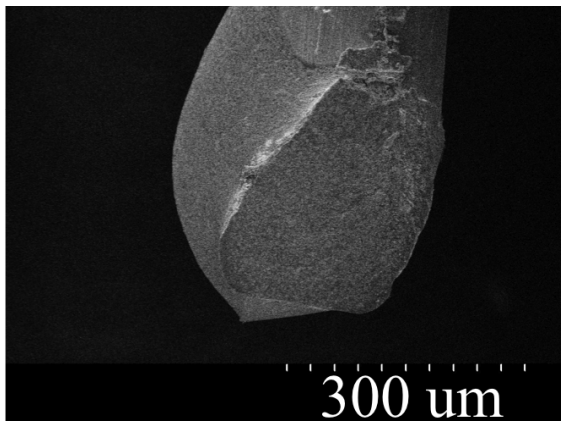
(a)



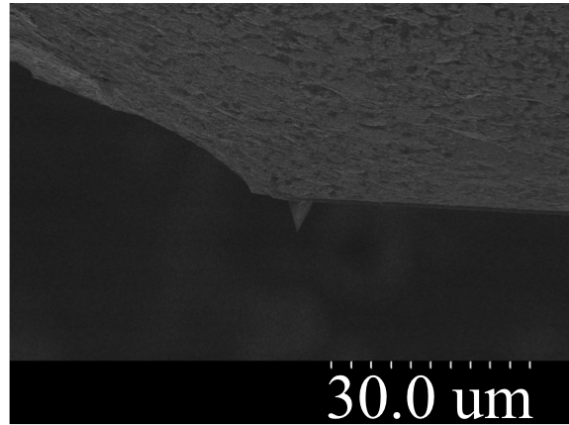
(b)

Figure 6.10: (a) The micropositioner used to assemble the ultrasharp tips. It finely positions a Pt(.8)Ir(.2) wire with respect to a AFM cantilever. (b) A view through the microscope used to see tip placement on the epoxy. The triangular cantilever is touching the conducting epoxy.

cause instabilities and have a larger radius of curvature than the AFM tip. Many tips ended up not having cylindrical symmetry, which made placing them on the HEMT circuit more challenging. Of the tips that were not engulfed by epoxy, many had a radius of curvature of 20-25 nm and there were some that was just over 10nm. Ultimately, the ultrasharp tip fabrication cost did not justify continuing to make them.



(a)



(b)

Figure 6.11: Ultrasharp tip with radius of curvature of 10 nm. (a) All components of the tip are visible: the cantilever, conducting epoxy, and Pt(.8)Ir(.2) wire. This tip has nice cylindrical symmetry. (b) The apex of the tip is the highest point.

Chapter 7

Conclusions

7.1 Summary

Even with the Bi_2Se_3 topological simplicity, there are other effects that coexist in the surface layers that may have an impact on future experiments. My measurements show bulk-like wavefunctions overlap with the topologically protected Dirac cone on the surface. The interplay between the shoulder states and the Dirac cone states presents potential competing channels for scattering to take place. As the top quintuple layer separates from the crystal, a two-dimensional electron gas can form on the surface and likewise overlap with the Dirac cone. Menshcikova *et al.* showed that a 2DEG can push the topological state into the second highest quintuple layer, which might reduce the amplitude of the Dirac cone that overlaps with the surface, perhaps complicating applications [108].

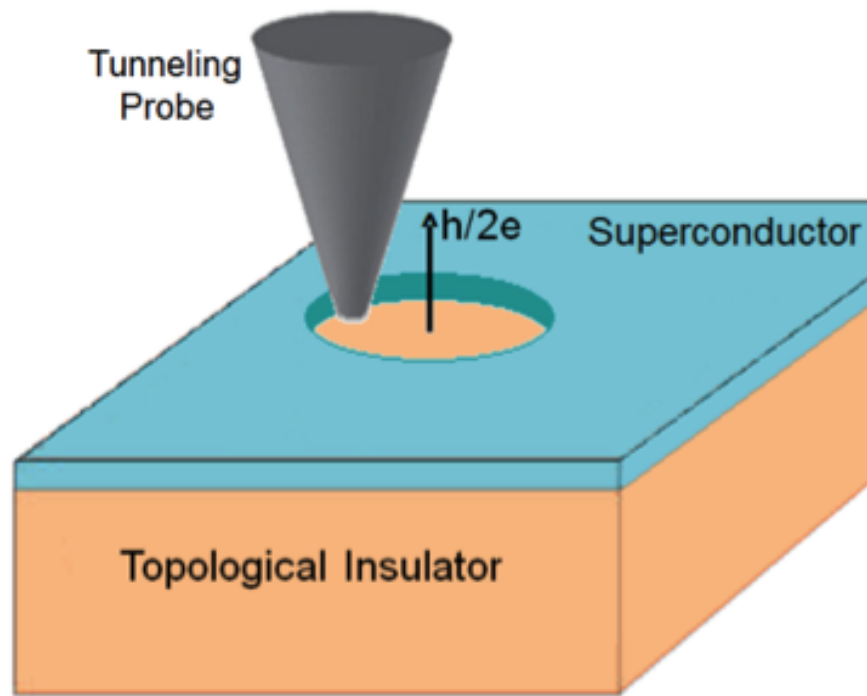


Figure 7.1: Schematic of the proposed experiment. An STM tip will probe vortices in an superconducting antidot patterned on a topological insulator to search for Majorana modes [51]. Figure from Dr. Stuart Tessmer.

7.2 Future Directions

The first experiment planned by my successor, Matthias Muenks, will probe small superconductor islands on a large Bi_2Se_3 crystal to explore the superconducting/topological insulator interface. When a superconductor is interfaced with a topological insulator many exotic effects are predicted, the most exciting of which is the Majorana fermion [9]. The Majorana fermion in this context is a particle that is its own hole. Because inversion symmetry is broken at the surface of a topological insulator, putting a topological insulator in close proximity to a superconductor induces unconventional p-wave order [9, 116].

The proximity effect occurs when a normal metal is interfaced with a superconductor [117]. Cooper pairs leak into the normal metal leaving a reduction of Cooper pairs in the superconductor. This effect should also be present when interfacing with topological insulator, but at present nobody has successfully obtained local density of states measurements to confirm it. Now that I have characterized the surface of Bi_2Se_3 , the next focus in the group will be to explore these effects. The plan for the first measurements is to evaporate a superconducting material like Nb, Pb or PbBi until it forms random superconducting islands on the surface of the Bi_2Se_3 crystals to study the superconducting local proximity effect in this hybrid system. Once these experiments are successful, future experiments are planned which require the superconductor to be patterned on the topological insulator, like that in Figure 7.1. By probing the holes in these patterns, Matthias Muenks hopes to find the predicted Majorana Fermion [9, 118, 119].

BIBLIOGRAPHY

BIBLIOGRAPHY

- [1] R. Prange and S. Girvin, *The Quantum Hall effect*. Graduate texts in contemporary physics, Springer-Verlag, 1987.
- [2] D. Thouless, M. Kohmoto, M. Nightingale, and M. Denny, “Quantized Hall Conductance in a Two-Dimensional Periodic Potential,” *Physical Review Letters*, vol. 49, no. 6, pp. 405–408, 1982.
- [3] S. Murakami, “Quantum Spin Hall Effect and Enhanced Magnetic Response by Spin-Orbit Coupling,” *Physical Review Letters*, vol. 97, no. 23, p. 236805, 2006.
- [4] C. Kane and E. Mele, “ Z_2 Topological Order and the Quantum Spin Hall Effect,” *Physical Review Letters*, vol. 95, p. 146802, SEP 30 2005.
- [5] J. E. Moore and L. Balents, “Topological Invariants of Time-Reversal-Invariant Band Structures,” *Physical Review B*, vol. 75, no. 12, p. 121306(R), 2007.
- [6] H. Zhang, C.-X. Liu, X.-L. Qi, X. Dai, Z. Fang, and S.-C. Zhang, “Topological Insulators in Bi_2Se_3 , Bi_2Te_3 and Sb_2Te_3 with a Single Dirac Cone on the Surface,” *Nature Physics*, vol. 5, pp. 438–442, May 2009.
- [7] X.-l. Qi, T. L. Hughes, and S.-c. Zhang, “Topological Field Theory of Time-Reversal Invariant Insulators,” *Physical Review B*, vol. 78, no. 19, p. 195424, 2008.
- [8] X.-l. Qi, “Inducing a Magnetic Monopole with Topological Surface States,” *Science*, vol. 1184, no. 323, 2009.
- [9] L. Fu and C. Kane, “Superconducting Proximity Effect and Majorana Fermions at the Surface of a Topological Insulator,” *Physical Review Letters*, vol. 100, p. 096407, Mar. 2008.

- [10] S. Urazhdin, D. Bilc, S. Mahanti, S. Tessmer, T. Kyratsi, and M. Kanatzidis, “Surface Effects in Layered Semiconductors Bi_2Se_3 and Bi_2Te_3 ,” *Physical Review B*, vol. 69, p. 085313, Feb. 2004.
- [11] J. Choi, H. Lee, B. Kim, S. Choi, J. Choi, J. Song, and S. Cho, “Mn-Doped V2VI3 Semiconductors: Single Crystal Growth and Magnetic Properties,” *Journal of Applied Physics*, vol. 97, MAY 15 2005. 49th Annual Conference on Magnetism and Magnetic Materials, Jacksonville, FL, NOV 07-11, 2004.
- [12] J. Choi, H.-W. Lee, B.-S. Kim, H. Park, S. Choi, S. C. Hong, and S. Cho, “Magnetic and Transport Properties of Mn-doped Bi_2Se_3 and Sb_2Se_3 ,” *Journal of Magnetism and Magnetic Materials*, vol. 304, pp. 164–166, SEP 2006.
- [13] Y. L. Chen, J. G. Analytis, J.-H. Chu, Z. Liu, S. K. Mo, X. L. Qi, H.-J. Zhang, D. H. Lu, X. Dai, Z. Fang, S. Zhang, I. R. Fisher, Z. Hussain, and Z.-X. Shen, “Experimental Realization of a Three-Dimensional Topological Insulator, Bi_2Te_3 ,” *Science*, vol. 325, pp. 178–81, July 2009.
- [14] S. Urazhdin, D. Bilc, S. Tessmer, S. Mahanti, T. Kyratsi, and M. Kanatzidis, “Scanning Tunneling Microscopy of Defect States in the Semiconductor Bi_2Se_3 ,” *Physical Review B*, vol. 66, p. 161306, OCT 15 2002.
- [15] G. Binnig, H. Rohrer, C. Gerber, and E. Weibel, “7X7 Reconstruction on $\text{Si}(111)$ Resolved in Real Space,” *Physical Review Letters*, vol. 50, no. 2, pp. 120–123, 1983.
- [16] G. Binnig, H. Rohrer, C. Gerber, and E. Weibel, “Tunneling through a Controllable Vacuum Gap,” *Applied Physics Letters*, vol. 40, no. 2, pp. 178–180, 1982.
- [17] I. Giaever, “Electron Tunneling Between 2 Superconductors,” *Physical Review Letters*, vol. 5, no. 10, pp. 464–466, 1960.
- [18] I. Giaever, “Energy Gap in Superconductors Measured by Electron Tunneling,” *Physical Review Letters*, vol. 5, no. 4, pp. 147–148, 1960.
- [19] J. Bardeen, “Tunneling from a Many-Particle Point of View,” *Physical Review Letters*, vol. 6, pp. 57–59, 1961.
- [20] J. Tersoff and D. Hamann, “Theory and Application for the Scanning Tunneling Microscope,” *Physical Review Letters*, vol. 50, no. 25, pp. 1998–2001, 1983.

- [21] J. Tersoff and D. Hamann, “Theory of the Scanning Tunneling Microscope,” *Physical Review B*, vol. 31, no. 2, pp. 805–813, 1985.
- [22] G. Binnig and H. Rohrer, “Scanning Tunneling Microscopy - From Birth to Adolescence,” *Reviews of Modern Physics*, vol. 59, pp. 615–625, JUL 1987.
- [23] G. Binnig and H. Rohrer, “Scanning Tunneling Microscopy,” *Helvetica Physica Acta*, vol. 55, no. 6, pp. 726–735, 1982.
- [24] G. Binnig, G and D. Smith, “Single-Tube 3-Dimensional Scanner for Scanning Tunneling Microscopy,” *Review of Scientific Instruments*, vol. 57, pp. 1688–1689, AUG 1986.
- [25] K. Besocke, “AN Easily Operable Scanning Tunneling Microscope,” *Surface Science*, vol. 181, pp. 145–153, MAR 1987.
- [26] S. Pan, E. Hudson, and J. Davis, “He-3 refrigerator based very low temperature scanning tunneling microscope,” *Review of Scientific Instruments*, vol. 70, pp. 1459–1463, FEB 1999.
- [27] J. Barth, H. Brune, G. Ertl, and R. Behm, “Scanning Tunneling Microscopy Observations on the Reconstructed Au(111) Surface - Atomic Structure, Long-Range Superstructure, Rotational Domains, and Surface-Defects,” *Physical Review B*, vol. 42, pp. 9307–9318, NOV 15 1990.
- [28] J. P. Veazey, G. Reguera, and S. H. Tessmer, “Electronic properties of conductive pili of the metal-reducing bacterium *Geobacter sulfurreducens* probed by scanning tunneling microscopy (vol 84, 060901, 2011),” *Physical Review E*, vol. 85, APR 26 2012.
- [29] T. Chen, S. Tessmer, J. Tucker, J. Lyding, and D. Vanharlingen, “Scanning Tunneling Microscopy and Spectroscopy of Thin-Film Superconductor PB,” *Journal of Vacuum Science & Technology B*, vol. 9, no. 2, Part 2, pp. 1000–1005, 1991.
- [30] H. Kim, C. Malliakas, A. Tomic, S. Tessmer, M. Kanatzidis, and S. Billinge, “Local Atomic Structure and Discommensurations in the Charge Density Wave of CeTe_3 ,” *Physical Review Letters*, vol. 96, p. 226401, JUN 9 2006.
- [31] J. Baland, “Manipulating Chlorine Atom Bonding on the Si(100)-(2x1) Surface with the STM,” *Science*, vol. 262, pp. 1703–1706, DEC 10 1993.

- [32] J. Boland and J. Villarrubia, “Identification of the Products from the Reaction of Chlorine with the Silicon(111)-(7X7) Surface,” *Science*, vol. 248, pp. 838–840, MAY 18 1990.
- [33] K. Besocke and S. Berger, “Piezoelectric Driven Kelvin Probe For Contact Potential Difference Studies,” *Review of Scientific Instruments*, vol. 47, no. 7, pp. 840–842, 1976.
- [34] M. Gasseller, M. DeNinno, R. Loo, J. F. Harrison, M. Caymax, S. Rogge, and S. H. Tessmer, “Single-Electron Capacitance Spectroscopy of Individual Dopants in Silicon,” *Nano Letters*, vol. 11, pp. 5208–5212, DEC 2011.
- [35] R. Ashoori, “Electrons in artificial atoms,” *Nature*, vol. 379, pp. 413–419, Feb 1 1996.
- [36] I. Maasilta, S. Chakraborty, I. Kuljanishvili, S. Tessmer, and M. Melloch, “Tunneling Images of a 2D Electron System in a Quantizing Magnetic Field,” *Physica E-Low-Dimensional Systems & Nanostructures*, vol. 18, pp. 167–168, MAY 2003.
- [37] S. Tessmer, P. Glicofridis, R. Ashoori, L. Levitov, and M. Melloch, “Subsurface charge accumulation imaging of a quantum Hall liquid (vol 392, pg 51, 1998),” *Nature*, vol. 395, p. 724, OCT 15 1998.
- [38] J. P. Veazey, *Scanning probe studies of the pilus nanowires in Geobacter sulfurreducens*. PhD thesis, Michigan State University, 2011.
- [39] J. Stroscio and W. Kaiser, eds., *Scanning tunneling Microscopy*, vol. 27 of *Methods of Experimental Physics*. Academic Press, 1993.
- [40] C. J. Chen, *Introduction to Scanning Tunneling Microscopy*, vol. 64 of *Monographs on the Physics and Chemistry of Materials*. Oxford Science Publications, 2nd. edition ed., 2008.
- [41] R. Feenstra, J. Stroscio, J. Tersoff, and A. Fein, “Atom-Selective Imaging of the GAAS(110) Surface,” *Physical Review Letters*, vol. 58, pp. 1192–1195, MAR 23 1987.
- [42] N. Lang, “Spectroscopy of Single Atoms in the Scanning Tunneling Microscope,” *Physical Review B*, vol. 34, pp. 5947–5950, OCT 15 1986.
- [43] M. Gasseller, *Scanning Probe Study of Semiconductor Dopant Charging (A Doctoral Thesis)*. PhD thesis, Michigan State University, ProQuest Dissertation and Theses, 2010.

- [44] W. Zhang, R. Yu, H.-J. Zhang, X. Dai, and Z. Fang, “First-principles studies of the three-dimensional strong topological insulators Bi_2Te_3 , Bi_2Se_3 and Sb_2Te_3 ,” *New Journal of Physics*, vol. 12, p. 065013, June 2010.
- [45] N. Ashcroft and N. Mermin, *Solid State Physics*. Philadelphia: Saunders College, 1976.
- [46] X.-L. Qi and S.-C. Zhang, “The quantum spin Hall effect and topological insulators,” *Physics Today*, vol. 63, pp. 33–38, JAN 2010.
- [47] K. v. Klitzing, G. Dorda, and M. Pepper, “New method for high-accuracy determination of the fine-structure constant based on quantized hall resistance,” *Physical Review Letters*, vol. 45, pp. 494–497, Aug 1980.
- [48] C. L. Kane and E. J. Mele, “Quantum Spin Hall Effect in Graphene,” *Physical Review Letters*, vol. 95, no. 22, p. 226801, 2005.
- [49] B. A. Bernevig and S.-C. Zhang, “Quantum Spin Hall Effect,” *Physical Review Letters*, vol. 96, p. 106802, Mar. 2006.
- [50] S. Murakami, N. Nagaosa, and S.-c. Zhang, “Spin-Hall Insulator,” *Physical Review Letters*, vol. 93, no. 15, p. 156804, 2004.
- [51] M. Z. Hasan and C. L. Kane, “Colloquium: Topological Insulators,” *Reviews of Modern Physics*, vol. 82, pp. 3045–3067, Nov 8 2010.
- [52] L. Fu and C. Kane, “Topological Insulators with Inversion Symmetry,” *Physical Review B*, vol. 76, p. 045302, July 2007.
- [53] L. Fu, *Theory of Topological Insulators*. PhD thesis, University of Pennsylvania, 2009.
- [54] R. Roy, “ \mathbb{Z}_2 Classification of Quantum Spin Hall Systems: An Approach Using Time-Reversal Invariance,” *Physical Review B*, vol. 79, p. 195321, May 2009.
- [55] B. A. Bernevig, T. L. Hughes, and S.-C. Zhang, “Quantum spin Hall effect and topological phase transition in HgTe quantum wells,” *Science*, vol. 314, pp. 1757–1761, DEC 15 2006.
- [56] M. Koenig, S. Wiedmann, C. Bruene, A. Roth, H. Buhmann, L. W. Molenkamp, X.-L. Qi, and S.-C. Zhang, “Quantum Spin Hall Insulator State in HgTe Quantum Wells,” *Science*, vol. 318, pp. 766–770, NOV 2 2007.

- [57] L. Fu, C. Kane, and E. Mele, “Topological Insulators in Three Dimensions,” *Physical Review Letters*, vol. 98, p. 106803, Mar. 2007.
- [58] P. Roushan, J. Seo, C. V. Parker, Y. S. Hor, D. Hsieh, D. Qian, A. Richardella, M. Z. Hasan, R. J. Cava, and A. Yazdani, “Topological surface states protected from backscattering by chiral spin texture,” *Nature*, vol. 460, pp. 1106–1109, AUG 27 2009.
- [59] H.-J. Zhang, C.-X. Liu, X.-L. Qi, X.-Y. Deng, X. Dai, S.-C. Zhang, and Z. Fang, “Electronic Structures and Surface states of the Topological Insulator BiSb,” *Physical Review B*, vol. 80, p. 085307, Aug. 2009.
- [60] D. Hsieh, D. Qian, L. Wray, Y. Xia, Y. S. Hor, R. J. Cava, and M. Z. Hasan, “LETTERS A Topological Dirac Insulator in a Quantum Spin Hall Phase,” *Nature*, vol. 452, no. April, pp. 970–974, 2008.
- [61] T. Hirahara, K. Miyamoto, I. Matsuda, T. Kadono, A. Kimura, T. Nagao, G. Bihlmayer, E. Chulkov, S. Qiao, K. Shimada, H. Namatame, M. Taniguchi, and S. Hasegawa, “Direct Observation of Spin Splitting in Bismuth Surface States,” *Physical Review B*, vol. 76, p. 153305, Oct. 2007.
- [62] J. Hoffman, K. McElroy, D. Lee, K. Lang, H. Eisaki, S. Uchida, and J. Davis, “Imaging Quasiparticle Interference in $\text{Bi}_2\text{Sr}_2\text{CaCu}_2\text{O}_{8+\delta}$,” *Science*, vol. 297, pp. 1148–1151, AUG 16 2002.
- [63] G. Zhang, H. Qin, J. Teng, J. Guo, Q. Guo, X. Dai, Z. Fang, and K. Wu, “Quintuple-layer Epitaxy of Thin Films of Topological Insulator Bi_2Se_3 ,” *Applied Physics Letters*, vol. 95, no. 5, p. 053114, 2009.
- [64] H. Noh, H. Koh, S. Oh, J. Park, H. Kim, J. D. Rameau, T. Valla, and T. E. Kidd, “Spin-orbit Interaction Effect in the Electronic Structure of Bi_2Te_3 Observed by Angle-resolved Photoemission Spectroscopy,” *Europhysics Letters*, vol. 81, no. March, p. 57006, 2008.
- [65] Y. Wang, D. Hsieh, D. Pilon, L. Fu, D. Gardner, Y. Lee, and N. Gedik, “Observation of a Warped Helical Spin Texture in Bi_2Se_3 from Circular Dichroism Angle-Resolved Photoemission Spectroscopy,” *Physical Review Letters*, vol. 107, p. 207602, Nov. 2011.
- [66] C. Jozwiak, Y. Chen, A. Fedorov, J. Analytis, C. Rotundu, A. Schmid, J. Denlinger, Y.-D. Chuang, D.-H. Lee, I. Fisher, R. Birgeneau, Z.-X. Shen, Z. Hussain, and A. Lanzara, “Widespread Spin Polarization Effects in Photoemission from Topological Insulators,” *Physical Review B*, vol. 84, p. 165113, Oct. 2011.

- [67] Z.-H. Pan, A. Fedorov, D. Gardner, Y. Lee, S. Chu, and T. Valla, “Measurement of an Exceptionally Weak Electron-Phonon Coupling on the Surface of the Topological Insulator Bi_2Se_3 Using Angle-Resolved Photoemission Spectroscopy,” *Physical Review Letters*, vol. 108, p. 187001, May 2012.
- [68] X. Zhu, L. Santos, C. Howard, R. Sankar, F. Chou, C. Chamon, and M. El-Batanouny, “Electron-Phonon Coupling on the Surface of the Topological Insulator Bi_2Se_3 Determined from Surface-Phonon Dispersion Measurements,” *Physical Review Letters*, vol. 108, p. 185501, May 2012.
- [69] P. Cheng, C. Song, T. Zhang, Y. Zhang, Y. Wang, J.-F. Jia, J. Wang, Y. Wang, B.-F. Zhu, X. Chen, X. Ma, K. He, L. Wang, X. Dai, Z. Fang, X. Xie, X.-L. Qi, C.-X. Liu, S.-C. Zhang, and Q.-K. Xue, “Landau Quantization of Topological Surface States in Bi_2Se_3 ,” *Physical Review Letters*, vol. 105, p. 076801, Aug. 2010.
- [70] P. Schwab and M. Dzierzawa, “Landau Levels in a Topological Insulator,” *Physical Review B*, vol. 85, p. 155403, Apr. 2012.
- [71] T. Hanaguri, K. Igarashi, M. Kawamura, H. Takagi, and T. Sasagawa, “Momentum-Resolved Landau-Level Spectroscopy of Dirac Surface State in Bi_2Se_3 ,” *Physical Review B*, vol. 82, p. 081305(R), Aug. 2010.
- [72] P. Cheng, T. Zhang, K. He, X. Chen, X. Ma, and Q. Xue, “Scanning tunneling microscopy studies of topological insulators,” *Physica E: Low-dimensional Systems and Nanostructures*, vol. 44, pp. 912–916, Feb. 2012.
- [73] Z. Ren, A. A. Taskin, S. Sasaki, K. Segawa, and Y. Ando, “Observations of Two-Dimensional Quantum Oscillations and Ambipolar Transport in the Topological Insulator Bi_2Se_3 Achieved by Cd doping,” *Physical Review B*, vol. 84, p. 075316, AUG 9 2011.
- [74] J. G. Checkelsky, Y. S. Hor, M. H. Liu, D. X. Qu, R. J. Cava, and N. P. Ong, “Quantum Interference in Macroscopic Crystals of Nonmetallic Bi_2Se_3 ,” *Physical Review Letters*, vol. 103, p. 246601, DEC 11 2009.
- [75] J. G. Checkelsky, Y. S. Hor, R. J. Cava, and N. P. Ong, “Bulk Band Gap and Surface State Conduction Observed in Voltage-Tuned Crystals of the Topological Insulator Bi_2Se_3 ,” *Physical Review Letters*, vol. 106, p. 196801, MAY 10 2011.
- [76] J. G. Analytis, R. D. McDonald, S. C. Riggs, J.-H. Chu, G. S. Boebinger, and I. R. Fisher, “Two-dimensional Surface State in the Quantum Limit of a Topological Insulator,” *Nature Physics*, vol. 6, pp. 960–964, DEC 2010.

- [77] D. Kim, S. Cho, N. P. Butch, P. Syers, K. Kirshenbaum, S. Adam, J. Paglione, and M. S. Fuhrer, “Surface Conduction of Topological Dirac Electrons in Bulk Insulating Bi_2Se_3 ,” *Nature Physics*, vol. 8, pp. 459–463, Apr. 2012.
- [78] P. Di Pietro, F. M. Vitucci, D. Nicoletti, L. Baldassarre, P. Calvani, R. Cava, Y. S. Hor, U. Schade, and S. Lupi, “Optical Conductivity of Bismuth-Based Topological Insulators,” *Physical Review B*, vol. 86, p. 045439, JUL 24 2012.
- [79] L. He, F. Xiu, X. Yu, M. Teague, W. Jiang, Y. Fan, X. Kou, M. Lang, Y. Wang, G. Huang, N.-C. Yeh, and K. L. Wang, “Surface-dominated Conduction in a 6 nm Thick Bi_2Se_3 Thin Film.,” *Nano letters*, vol. 12, pp. 1486–90, Mar. 2012.
- [80] H. Beidenkopf, P. Roushan, J. Seo, L. Gorman, I. Drozdov, Y. S. Hor, R. J. Cava, and A. Yazdani, “Spatial Fluctuations of Helical Dirac Fermions on the Surface of Topological Insulators,” *Nature Physics*, vol. 7, pp. 939–943, DEC 2011.
- [81] L. A. Wray, S.-Y. Xu, Y. Xia, D. Hsieh, A. V. Fedorov, Y. S. Hor, R. J. Cava, A. Bansil, H. Lin, and M. Z. Hasan, “A Topological Insulator Surface Under Strong Coulomb, Magnetic and Disorder Perturbations,” *Nature Physics*, vol. 7, pp. 32–37, JAN 2011.
- [82] Y. S. Hor, A. Richardella, P. Roushan, Y. Xia, J. G. Checkelsky, A. Yazdani, M. Z. Hasan, N. P. Ong, and R. J. Cava, “P-Type Bi_2Se_3 for Topological Insulator and Low-Temperature Thermoelectric Applications,” *Physical Review B*, vol. 79, p. 195208, MAY 2009.
- [83] D. Hsieh, Y. Xia, D. Qian, L. Wray, J. H. Dil, F. Meier, J. Osterwalder, L. Patthey, J. G. Checkelsky, N. P. Ong, A. V. Fedorov, H. Lin, A. Bansil, D. Grauer, Y. S. Hor, R. J. Cava, and M. Z. Hasan, “LETTERS A Tunable Topological Insulator in the Spin Helical Dirac Transport Regime,” *Nature*, vol. 460, no. 7259, pp. 1101–1105, 2009.
- [84] Y. S. Hor, a. J. Williams, J. G. Checkelsky, P. Roushan, J. Seo, Q. Xu, H. W. Zandbergen, A. Yazdani, N. P. Ong, and R. J. Cava, “Superconductivity in $\text{Cu}_x\text{Bi}_2\text{Se}_3$ and Its Implications for Pairing in the Undoped Topological Insulator,” *Physical Review Letters*, vol. 104, p. 057001, Feb. 2010.
- [85] T. Valla, Z.-H. Pan, D. Gardner, Y. Lee, and S. Chu, “Photoemission Spectroscopy of Magnetic and Nonmagnetic Impurities on the Surface of the Bi_2Se_3 Topological Insulator,” *Physical Review Letters*, vol. 108, p. 117601, Mar. 2012.
- [86] M. Ye, S. Eremeev, K. Kuroda, E. Krasovskii, E. Chulkov, Y. Takeda, Y. Saitoh, K. Okamoto, S. Zhu, K. Miyamoto, M. Arita, M. Nakatake, T. Okuda, Y. Ueda,

- K. Shimada, H. Namatame, M. Taniguchi, and a. Kimura, “Quasiparticle Interference on the Surface of Bi_2Se_3 Induced by Cobalt Adatom in the Absence of Ferromagnetic Ordering,” *Physical Review B*, vol. 85, p. 205317, May 2012.
- [87] J. J. Cha, J. R. Williams, D. Kong, S. Meister, H. Peng, A. J. Bestwick, P. Gallagher, D. Goldhaber-Gordon, and Y. Cui, “Magnetic Doping and Kondo Effect in Bi_2Se_3 Nanoribbons.,” *NanoLetters*, vol. 10, pp. 1076–81, Mar. 2010.
- [88] Y. L. Chen, J.-H. Chu, J. G. Analytis, Z. Liu, K. Igrashi, H.-H. Kuo, X. L. Qi, S. K. Mo, M. R. G., D. H. Lu, M. Hashimoto, T. Sasagawa, S. Zhang, I. R. Fisher, Z. Hussain, and Z. X. Shen, “Massive Dirac Fermion on the Surface of a Magnetically Doped Topological Insulator,” *Science*, vol. 329, pp. 659–62, Aug. 2010.
- [89] J. Honolka, A. A. Khajetoorians, V. Sessi, T. O. Wehling, S. Stepanow, J. L. Mi, B. B. Iversen, T. Schlenk, J. Wiebe, N. B. Brookes, A. I. Lichtenstein, P. Hofmann, K. Kern, and R. Wiesendanger, “In-Plane Magnetic Anisotropy of Fe Atoms on $\text{Bi}_2\text{Se}_3(111)$,” *Physical Review Letters*, vol. 108, p. 256811, JUN 22 2012.
- [90] M. Teague, H. Chu, F.-X. Xiu, L. He, K.-L. Wang, and N.-C. Yeh, “Observation of Fermi-energy Dependent Unitary Impurity Resonances in a Strong Topological Insulator Bi_2Se_3 with Scanning Tunneling Spectroscopy,” *Solid State Communications*, vol. 152, pp. 747–751, May 2012.
- [91] Z. Alpichsev, R. Biswas, A. Balatsky, J. G. Analytis, J.-H. Chu, I. Fisher, and A. Kapitulnik, “STM imaging of impurity resonances on Bi_2Se_3 .” arxiv1108.002v1.
- [92] B. Yan, D. Zhang, and C. Felser, “Topological surface states of bi_2se_3 with the coexistence of se vacancies.” arxiv1209.5985v3, October 2012.
- [93] L. Xue, P. Zhou, C. Zhang, C. He, G. Hao, L. Sun, and J. Zhong, “First-principles study of native point defects in bi_2se_3 .” arxiv:1270.0103v1.
- [94] Y.-L. Wang, Y. Xu, Y.-P. Jiang, J.-W. Liu, C.-Z. Chang, M. Chen, Z. Li, C.-L. Song, L.-L. Wang, K. He, X. Chen, W.-H. Duan, Q.-K. Xue, and X.-C. Ma, “Structural Defects and Electronic Properties of the Cu-doped Topological Insulator Bi_2Se_3 ,” *Physical Review B*, vol. 84, p. 075335, Aug. 2011.
- [95] S. Kim, M. Ye, K. Kuroda, Y. Yamada, E. Krasovskii, E. Chulkov, K. Miyamoto, M. Nakatake, T. Okuda, Y. Ueda, K. Shimada, H. Namatame, M. Taniguchi, and A. Kimura, “Surface Scattering via Bulk Continuum States in the 3D Topological Insulator Bi_2Se_3 ,” *Physical Review Letters*, vol. 107, p. 056803, July 2011.

- [96] S. R. Park, W. S. Jung, C. Kim, D. J. Song, C. Kim, S. Kimura, K. D. Lee, and N. Hur, “Quasiparticle scattering and the protected nature of the topological states in a parent topological insulator Bi_2Se_3 ,” *Physical Review B*, vol. 81, no. 4, p. 041405(R), 2010.
- [97] S. R. Park, W. S. Jung, G. R. Han, Y. K. Kim, C. Kim, D. J. Song, Y. Y. Koh, S. Kimura, K. D. Lee, N. Hur, J. Y. Kim, B. K. Cho, J. H. Kim, Y. S. Kwon, J. H. Han, and C. Kim, “Intrinsic quasi-particle dynamics of topological metallic states,” *New Journal of Physics*, vol. 13, p. 013008, Jan. 2011.
- [98] Z. Alpichshev, J. G. Analytis, J. H. Chu, I. R. Fisher, Y. L. Chen, Z. X. Shen, A. Fang, and A. Kapitulnik, “STM Imaging of Electronic Waves on the Surface of Bi_2Te_3 : Topologically Protected Surface States and Hexagonal Warping Effects,” *Physical Review Letters*, vol. 104, p. 016401, JAN 8 2010.
- [99] J. W. McIver, D. Hsieh, H. Steinberg, P. Jarillo-Herrero, and N. Gedik, “Control over topological insulator photocurrents with light polarization,” *Nature nanotechnology*, vol. 7, pp. 96–100, Feb. 2012.
- [100] Y. Xia, D. Qian, D. Hsieh, L. Wray, a. Pal, H. Lin, a. Bansil, D. Grauer, Y. S. Hor, R. J. Cava, and M. Z. Hasan, “Observation of a Large-Gap Topological-Insulator Class with a Single Dirac Cone on the Surface,” *Nature Physics*, vol. 5, pp. 398–402, May 2009.
- [101] C. Chen, S. He, H. Weng, W. Zhang, L. Zhao, H. Liu, X. Jia, and D. Mou, “Robustness of Topological Order and Formation of Quantum Well States in Topological Insulators Exposed to Ambient Environment,” *Proceedings of the National Academy of Sciences of the United States of America*, vol. 109, no. 10, pp. 3694–3698, 2012.
- [102] M. Bianchi, D. Guan, S. Bao, J. Mi, B. B. Iversen, P. D. C. King, and P. Hofmann, “Coexistence of the Topological State and a Two-Dimensional Electron Gas on the Surface of Bi_2Se_3 ,” *Nature communications*, vol. 1, p. 128, Jan. 2010.
- [103] M. Bianchi, R. C. Hatch, J. Mi, B. B. Iversen, and P. Hofmann, “Simultaneous Quantization of Bulk Conduction and Valence States through Adsorption of Nonmagnetic Impurities on Bi_2Se_3 ,” *Physical Review Letters*, vol. 107, p. 086802, AUG 16 2011.
- [104] H. Benia, C. Lin, K. Kern, and C. Ast, “Reactive Chemical Doping of the Bivol. 107, p. 177602, Oct. 2011.
- [105] L. Fu, “Hexagonal Warping Effects in the Surface States of the Topological Insulator Bi_2Te_3 ,” *Physical Review Letters*, vol. 103, p. 266801, Dec. 2009.

- [106] M. Brahlek, Y. S. Kim, N. Bansal, E. Edrey, and S. Oh, “Surface Versus Bulk State in Topological Insulator Bi_2Se_3 Under Environmental Disorder,” *Applied Physics Letters*, vol. 99, no. 1, p. 012109, 2011.
- [107] D. Hsieh, Y. Xia, L. Wray, F. Meier, J. Dil, J. Osterwalder, L. Pathey, A. Fedorov, H. Lin, A. Bansil, D. Grauer, Y. S. Hor, R. J. Cava, and M. Z. Hasan, “Observation of Time-Reversal-Protected Single-Dirac-Cone Topological-Insulator States,” *Physical Review Letters*, vol. 103, no. 14, p. 146401, 2009.
- [108] T. V. Menshchikova, S. V. Eremeev, and E. V. Chulkov, “On the origin of two-dimensional electron gas states at the surface of topological insulators,” *JETP Letters*, vol. 94, pp. 106–111, Sept. 2011.
- [109] D. Hsieh, Y. Xia, L. Wray, D. Qian, A. Pal, J. H. Dil, J. Osterwalder, F. Meier, G. Bihlmayer, C. L. Kane, Y. S. Hor, R. J. Cava, and M. Z. Hasan, “Observation of Unconventional Quantum Spin Textures in Topological Insulators,” *Science*, vol. 323, pp. 919–922, 2009.
- [110] M. Romanowich, M.-S. Lee, D.-Y. Chung, J.-H. Song, S. Mahanti, M. G. Kanatzidis, and S. H. Tessmer, “The interplay of topological surface and bulk electronic states in bi_2se_3 .” arXiv:1210.1874, October 2012.
- [111] O. Yazyev, E. Kioupakis, J. Moore, and S. Louie, “Quasiparticle Effects in the Bulk and Surface-State Bands of Bi_2Se_3 and Bi_2Te_3 Topological Insulators,” *Physical Review B*, vol. 85, p. 160511(R), Apr. 2012.
- [112] P. D. C. King, R. C. Hatch, M. Bianchi, R. Ovsyannikov, C. Lupulescu, G. Landolt, B. Slomski, J. H. Dil, D. Guan, J. L. Mi, E. D. L. Rienks, J. Fink, A. Lindblad, S. Svensson, S. Bao, G. Balakrishnan, B. B. Iversen, J. Osterwalder, W. Eberhardt, F. Baumberger, and P. Hofmann, “Large Tunable Rashba Spin Splitting of a Two-Dimensional Electron Gas in Bi_2Se_3 ,” *Physical Review Letters*, vol. 107, p. 096802, AUG 25 2011.
- [113] S. Urazhdin, S. Tessmer, and R. Ashoori, “A simple low-dissipation amplifier for cryogenic scanning tunneling microscopy,” *Review of Scientific Instruments*, vol. 73, pp. 310–312, FEB 2002.
- [114] M. Bohmisch, F. Burmeister, A. Rettenberger, J. Zimmermann, J. Boneberg, and P. Leiderer, “Atomic force microscope based Kelvin measurements: Application to an electrochemical reaction,” *Journal of Physical Chemistry B*, vol. 101, pp. 10162–10165, DEC 4 1997.

- [115] I. Kujanishvili, S. Chakraborty, I. Maasilta, S. Tessmer, and M. Melloch, “Modeling electric-field-sensitive scanning probe measurements for a tip of arbitrary shape,” *Ultramicroscopy*, vol. 102, pp. 7–12, DEC 2004.
- [116] L. Fu and C. L. Kane, “Probing Neutral Majorana Fermion Edge Modes with Charge Transport,” *Physical Review Letters*, vol. 102, p. 216403, MAY 29 2009.
- [117] H. Meissner, “Superconductivity of Contacts With Interposed Barriers,” *Physical Review*, vol. 117, no. 3, pp. 672–680, 1960.
- [118] R. M. Lutchyn, J. D. Sau, and S. Das Sarma, “Majorana Fermions and a Topological Phase Transition in Semiconductor-Superconductor Heterostructures,” *Physical Review Letters*, vol. 105, p. 077001, AUG 13 2010.
- [119] J. D. Sau, S. Tewari, R. M. Lutchyn, T. D. Stanescu, and S. Das Sarma, “Non-Abelian quantum order in spin-orbit-coupled semiconductors: Search for topological Majorana particles in solid-state systems,” *Physical Review B*, vol. 82, p. 21409, DEC 9 2010.